

Northumbria Research Link

Citation: Zahertar, Shahrzad (2021) Development of electromagnetic metamaterials and surface acoustic wave transducers on a single device geometry. Doctoral thesis, Northumbria University.

This version was downloaded from Northumbria Research Link:
<https://nrl.northumbria.ac.uk/id/eprint/51643/>

Northumbria University has developed Northumbria Research Link (NRL) to enable users to access the University's research output. Copyright © and moral rights for items on NRL are retained by the individual author(s) and/or other copyright owners. Single copies of full items can be reproduced, displayed or performed, and given to third parties in any format or medium for personal research or study, educational, or not-for-profit purposes without prior permission or charge, provided the authors, title and full bibliographic details are given, as well as a hyperlink and/or URL to the original metadata page. The content must not be changed in any way. Full items must not be sold commercially in any format or medium without formal permission of the copyright holder. The full policy is available online: <http://nrl.northumbria.ac.uk/policies.html>



**Northumbria
University**
NEWCASTLE

**DEVELOPMENT OF
ELECTROMAGNETIC
METAMATERIALS AND SURFACE
ACOUSTIC WAVE TRANSDUCERS
ON A SINGLE DEVICE GEOMETRY**

SHAHRZAD ZAHERTAR

PhD

2021

**DEVELOPMENT OF
ELECTROMAGNETIC
METAMATERIALS AND SURFACE
ACOUSTIC WAVE TRANSDUCERS
ON A SINGLE DEVICE GEOMETRY**

SHAHRZAD ZAHERTAR

A thesis submitted in partial fulfilment of
the requirements of the University of
Northumbria at Newcastle for the degree of
Doctor of Philosophy

Faculty of Engineering and Environment

January 2021

Abstract

Ageing population and health challenges associated with it shows us the importance of continuous and remote health monitoring using inexpensive, low-power, sustainable, and simple to use Lab-on-Chip (LoC) devices. LoC systems aim to bring in the whole laboratory process onto a small chip. Although crucial effort has been invested into this field, a marketable product is yet difficult to attain. An important reason is that LoC systems are developed via the integration of different devices and even technologies that are tailored for an individual task. A streamlined integration of these on a single platform is challenging, especially considering complicated fabrication processes. There are two fundamental mechanisms that have important roles in development of a LoC device; i.e. sensing and fluid manipulation.

The aim of this thesis is to investigate a new method of bringing biosensing and fluid manipulation capabilities on a single structure that can be integrated in various biosensing platforms. The sensing capability is realised using metamaterial-based electromagnetic split ring resonators (SRR), and the fluid manipulation capability is realised using surface acoustic waves (SAWs). The functionalities are performed on a single structure fabricated on different rigid and flexible substrates. SRR-based sensors have drawn much attention in different fields such as material characterisation, biosensing, strain sensing and remote sensing attributed to their simple design and fabrication, reliability and high quality factor. SRRs are metallic structures that are fabricated on a dielectric substrate and operate at certain resonant frequencies. Their operational frequency depends on their geometry and the effective permittivity of the materials surrounding them. However, these structures are incapable of manipulating fluids. On the other hand, SAW actuators have been extensively studied for their ability in different microfluidic functionalities, namely, streaming, pumping, separation, jetting and nebulisation. SAW actuators consist of Interdigital Transducers (IDTs) that are patterned on a piezoelectric substrate. By applying radio frequency (RF) power to the IDTs travelling surface waves are generated, which is the driver of the microfluidic functions.

In this thesis, a general methodology for the integration of sensing and fluid manipulation capabilities in a single device is described based on four different designs introduced as separate chapters, which can be beneficial in LoC applications. These fabricated devices have been employed as wireless sensors in microwave frequency range and utilised as a SAW actuator by applying power in radio frequency range. In addition, a flexible embroidered SRR is also introduced in this thesis that can be utilised in daily items based on fabrics towards continuous monitoring applications.

Contents

Abstract	iii
Acknowledgements	xiii
Declaration	xv
List of Publications	xvii
1 Introduction	1
2 Literature Review	5
2.1 Sensors	5
2.2 Electrochemical Sensors	7
2.2.1 Voltammetric Sensors	8
2.2.2 Amperometric	9
2.3 Inductive-Capacitive Resonators	10
2.3.1 Basics of RF and microwaves	11
2.3.2 Metamaterials	16
2.3.3 Split-Ring Resonator	16
2.4 Acoustic Wave Actuators	18
2.4.1 Working Principles: Piezoelectric Effect	19
2.4.2 Bulk Acoustic Waves	21
2.4.3 Surface Acoustic Waves	22
2.4.4 Design considerations in SAWs	30
References	36
3 A Fully Integrated Biosensing Platform Combining Acoustofluidics and Electromagnetic Metamaterials	55
3.1 Introduction	56
3.2 Experimental Section	58
3.3 Results and Discussion	59
3.3.1 Acoustofluidic Characteristics	59

3.3.2	Electromagnetic Characteristics	65
3.4	Conclusion	71
	References	73
4	DSRR-Inspired Geometry for Integration of Metamaterial-Based Sensing and Acoustofluidic-	
	Based Streaming	79
4.1	Fabrication and Materials	80
4.2	Results and Discussions	80
4.2.1	Electromagnetic Characterisation	80
4.2.2	Experimental Setup	82
4.2.3	Glucose Sensing	83
4.2.4	Dielectric Material Characterisation	85
4.2.5	Yeast Fermentation Process	87
4.2.6	Acoustofluidic-based Characterisation	90
4.3	Conclusion	91
	References	93
5	Flexible and Integrated Sensing Platform of Acoustic Waves and Metamaterials based	
	on Polyimide-Coated Woven Carbon Fibers	97
5.1	Introduction	98
5.2	Experimental Section	100
5.3	Results and Discussion	101
5.3.1	Demonstration of Liquid Temperature Control using the Integrated Platform	106
5.3.2	UV Sensing using SAW	107
5.3.3	Glucose Concentration Monitoring using the Electromagnetic Resonator .	109
5.4	Conclusions	111
	References	112
6	A Flexible PVDF-based Platform Combining Acoustofluidics and Electromagnetic	
	Metamaterials	121
6.1	Introduction	122
6.2	Design and Fabrication of the Devices	123

6.3	Characterisation of the Devices	124
6.4	Conclusions	128
	References	129
7	Embroidered Rectangular Split-Ring Resonators for the Characterization of Dielectric Materials	131
7.1	Introduction	132
7.2	Materials and Methods	134
7.3	Results and Discussion	136
7.4	Conclusion	143
	References	144
8	Conclusion and Future Outlook	151
8.1	Future Work	155
	Acronyms	157

List of Figures

2.1	Sensor generations over time (Image is adapted from [8]).	6
2.2	Radio and optical spectra in electromagnetic radiation (Image is adapted from [24]).	10
2.3	Schematic of a two-port vector network analyser.	14
2.4	Commonly used SRRs. (a) Circular split-ring resonator (b) Circular dual split-ring resonator (c) Rectangular split-ring resonator (d) Rectangular dual split-ring resonator.	17
2.5	Key modes of BAWs and SAWs (adapted from [90])	19
2.6	Scheme of the piezoelectrical effect on a quartz crystal. (a) represents a cut in a quartz crystal at equilibrium moments. (b) represents a mechanical pressure applied. (c) represents a mechanical stretch applied.	20
2.7	Schematic of a back trench Film Bulk Acoustic Resonator (FBAR).	22
2.8	Schematic view of SAWs propagating through a droplet. The energy is dissipated within the liquid at the Rayleigh angle.	23

2.9	Flow patterns of acoustic streaming in a droplet induced by ZnO/Si SAWs: (a) Top view, where a single IDT on the left causes the butterfly streaming patterns inside the droplet; (b) the front-side view of butterfly streaming patterns induced by the ZnO/Si SAW; (c) the corresponding simulated streaming pattern using finite volume software induced by a SAW launched from the left [90].	25
2.10	Acoustic mixing of a water droplet with a red dye droplet at different intervals induced by a ZnO/Si SAW device with the SAW launched from the left side [90].	25
2.11	Splitting and translation of $3\mu L$ droplet into two $1.5\mu L$ droplets over time [132].	26
2.12	Vertical liquid jetting of a $2\mu L$ droplet actuated by ZnO/Si SAWs from two opposite IDTs. The SAWs are launched from two sides of the droplet, thus the droplet is pushed up from both sides by the opposing waves at the Rayleigh angle, i.e., (a) to (c). The leaky waves propagate inside the droplet and reach the surfaces of the deformed liquid and then are reflected back into the liquid, thus further pushing the liquid upwards, i.e., (c) to (f). The vertical jetting of the droplet continues until the elongated liquid beam break up into small droplets, i.e., (g) and (h) [90]. . . .	27
2.13	Surface Acoustic Wave configured as a delay line (adapted from [140]).	29
2.14	One-port SAW reflective delay line (adapted from [141]).	29
2.15	Surface Acoustic Wave configured as resonator (adapted from [140]).	30
2.16	One-port SAW resonator device (adapted from [141]).	30
2.17	Single-phase unidirectional transducer design scheme.	33
2.18	(a) Slant IDT design scheme (b) Circular IDTs [90].	34
3.1	(a) Illustration of a SAW device on a LiNbO_3 substrate which is placed on a FR4 substrate including antennas for electromagnetic excitation. (b) Cross-sectional schematic of the device [17].	60
3.2	S_{11} spectrum of the SAW device at acoustic frequencies. We used a network analyser to measure the spectrum between the ports defined by the pads of the IDT electrodes [17].	61
3.3	Micrographs of two sections of the IDT electrodes illustrating the variations in the finger widths of the IDT electrodes [17].	61

3.4	Experimental demonstration of streaming using polystyrene particles inside a droplet with a volume of $2 \mu\text{L}$, (a-b) cross-section view and (c-d) top view. (e) The distribution of velocity magnitudes in a time instant shown in subplot-(d) [17].	63
3.5	Experimental demonstration of pumping function. Subfigures (a-d) show a sequence of snapshots while a droplet with a volume of $1 \mu\text{L}$ is pumped along the surface.(e) Pumping speed, s , increases with power level, P , following $P \propto s^{-3.6}$ [17].	64
3.6	Experimental demonstration of jetting function. Subfigures (a-c) show snapshots while a droplet with a volume of $1 \mu\text{L}$ is manipulated at a fixed location over the surface.(d) The height of the manipulated droplet measured from its original height increases with applied power [17].	65
3.7	Simulated (a) S_{21} spectrum of the SAW device, (b) profile of surface current density at the resonance [17].	67
3.8	Simulated, b) measured S_{21} spectra of the SAW device while a liquid droplet with a volume of $2 \mu\text{l}$ is actuated on its substrate. (c) The shift in the resonant frequency of the SAW device due to the movement of a liquid droplet with a volume of $2 \mu\text{l}$. The distance of the droplet is measured from the edge of the IDT [17].	69
3.9	(a) Measured S_{21} spectra of the device while the concentration of glucose in a $2 \mu\text{L}$ -droplet is increased. (b) Change in the resonant frequency of the device with concentration of glucose [17].	70
4.1	Simulation and experimental characterisation of the fabricated device. (a) Simulated reflection (S_{11}) spectrum of the device where magnetic field is along x-axis, electric field is along y-axis and propagation vector is perpendicular to the plane of the device when a water droplet is defined inside the inner circle with $\epsilon_r = 1$ (blue), and with $\epsilon_r = 80$ (red) (b) Measured S_{11} spectrum of the device in the absence ($\epsilon_r = 1$) and presence ($\epsilon_r = 80$) of $30\mu\text{L}$ of DI droplet. The simulated current density patterns are shown (c) at 3.678 GHz for $\epsilon_r = 1$, and (d) at 3.678 GHz for $\epsilon_r = 80$ [11].	83
4.2	Effect of different glucose concentrations on the operational frequency of the device.	84

4.3	Effects of different materials inside the container on the frequency of the device. (a) S_{11} spectra of the materials that were used in the experiment. (b) Measured shift in the resonant frequency with and without the container for different materials. Setup is shown in the inset.	86
4.4	Yeast fermentation process and yeast control experiment. (a) measured shift in resonant frequency of the system over time. (b) S_{11} spectra of various intervals of time in fermentation process, including an inset representing a narrower range of frequency in reflection spectra of the system. (c) measured shift in resonant frequency of the control experiment (d) reflection spectra of different intervals of time for the control experiment. (e-g) the container used in fermentation process from beginning of the experiment towards the end respectively.	89
4.5	S_{11} characterisation of DSRR device within the range of 5-20MHz.	90
4.6	(a-f) Streaming patterns of polystyrene particles inside a 10 μ L droplet over time when the power applied to the electrode is 0.5 W at the frequency of 18 MHz. . .	91
5.1	(a) Schematic illustration of the integrated platform combining surface acoustic waves and metamaterials with the equivalent circuit of the device at resonance. (b) Schematic illustration of the integrated platform. Schematic illustrations of the experimental setups for (c) glucose sensing, (d) UV sensing, and (e) temperature control [26].	102
5.2	(a) XRD patterns of the ZnO/PI/carbon fiber tri-layer structure. (b) AFM image of the ZnO thin film. (c) Reflection spectra S_{11} of SAWs with the designed wavelengths of 64, 100, and 160 μ m. (d) Transmission spectrum S_{21} of the electromagnetic resonator of the SAW device with a wavelength of 64 μ m [26]. . . .	104
5.3	FEA simulation of vibration modes of SAW devices based on the ZnO/PI/carbon fiber structure: (a) Rayleigh wave modes with $\lambda = 64 \mu$ m and $\lambda = 160 \mu$ m and (b) reflection spectra S_{11} of devices with $\lambda = 64, 10,$ and 160μ m. Simulated patterns of (c) S_{21} spectrum of the electromagnetic resonator (the corresponding coupled SAW has a wavelength of 64 μ m) and (d) profile of surface current density at the resonance (the corresponding coupled SAW has a wavelength of 64 μ m) [26]. . .	105

5.4	Measured average temperatures of a 5 μL distilled water droplet on top of the SAW device with increasing input power. The inset shows that the average temperature is controlled by the input power (23 W) over time [26].	106
5.5	(a) Real-time frequency shift of the SAW UV sensor with a wavelength of 64 μm under UV light. (b) Total frequency shift varying with the UV intensity. (c) Sheet conductance varying with the UV intensity. (d) Temperature-change-induced frequency shift Δf_T and the ratio between Δf_T and the total shift varying with the UV intensity. The inset shows the temperature increase with the UV intensity [26].	108
5.6	(a) S_{21} spectra of the device with droplets with varying concentrations of glucose and (b) frequency shift of the device with glucose concentration, measured on three different days. The concentration values for each day were the same at 10, 100, 200, 300, 400, and 500 mg/dL. The markers in the figures are shifted slightly in the horizontal direction for better readability [26].	110
6.1	(a) Schematics of the metallised layer on a PVDF substrate, (b) cross-sectional overview of the fabricated devices, (c) induced circulating current and the equivalent circuit of the device operating as an electromagnetic metamaterial [6].	123
6.2	S_{11} spectra of the PVDF/silver-electrode device measured between the bonding pads [6].	125
6.3	S_{21} spectra of the PVDF/gold-electrode device measured using a pair of monopole antennas connected to a vector network analyser [6].	126
6.4	Simulated electromagnetic resonances of the device with different excitation conditions [6].	127
7.1	Photograph of the fabricated SRR structure with a single split using an inverted embroidery method [26].	135
7.2	Photograph of the experimental setup where an embroidered sensor is attached to an LDPE bottle filled with solvents [26].	135
7.3	(a) Simulation and experimental results (b) Current density patterns at 1.81, and 2.07 GHz for the excitation configuration shown in the figure [26].	137
7.4	(a) Simulation and experimental results (b) Current density patterns at 1.75, 1.93, 2.05, and 2.07 GHz for the excitation setting shown in the figure [26].	138

7.5	(a) Normalized S_{21} spectra of the SRR structure, where the sensor is wrapped around the LDPE bottles filled with DI water, methanol, ethanol, acetone, IPA, and empty bottle. (b) Measured resonant frequencies for different bottles [26]. . .	141
7.6	Histogram and mean value of the set of experiments for solvents and empty bottle [26].	142

List of Tables

2.1	Maxwell's equations in differential format	12
4.1	Material properties and the measured shift in the frequencies for different materials[11].	86
7.1	Material properties and the mean value of the measured frequencies for solvents.	142
8.1	Summary of the chapters.	154

Acknowledgements

First and foremost, I would like to express my sincere gratitude to my principal supervisor, Dr. Hamdi Torun. I've always felt very lucky to have the opportunity to work with him. I would like to thank him for his continuous support, guidance, encouragements, patience, brilliant ideas and solutions to the problems I faced during my studies. Completion of this dissertation without his guidance wouldn't be possible.

I would like to express my appreciation to Prof. Richard Fu for his generous assistance, efforts and contribution to this work.

I would like to thank the members of my dissertation committee for helping me improve the quality of this dissertation.

I would like to extend my thanks to the technical staff, Rebecca Payne, Gavin Warburton, and Dr. Pietro Maiello for their cooperation and assistance during this project.

I would like to thank colleagues and friends at Northumbria University, and our collaborators from other universities for the time we spent together, the discussions that we had, and in general for making this journey more enjoyable.

I would like to thank Northumbria University for funding my PhD studies.

I would like to express my gratitude to my best friends, B. T., A. P., and L. S., for always being there for me although being miles apart.

Lastly, I would like to thank my parents and my sister for their unconditional love and support throughout my life. Especially my mother, whose presence made the life much easier for me during the thesis submission process.

Declaration

I declare that the work contained in this thesis has not been submitted for any other award and that it is all my own work. I also confirm that this work fully acknowledges opinions, ideas and contributions from the work of others.

Any ethical clearance for the research presented in this thesis has been approved. Approval has been sought and granted by the *Faculty Ethics Committee* on 13/11/2018.

Name: Shahrzad Zahertar

Date: 31 January 2021

List of Publications

Journal Articles

- **Shahrzad Zahertar**, Y. Wang, Ran Tao, J. Xie, Yong Qing Fu, Hamdi Torun, *A fully integrated biosensing platform combining acoustofluidics and electromagnetic metamaterials*. J. Phys. D: Appl. Phys. 52 485004, 17 September 2019.
- **Shahrzad Zahertar**, Emma Laurin, Linzi E. Dodd, Hamdi Torun, *Embroidered Rectangular Split-Ring Resonators for the Characterization of Dielectric Materials*. IEEE Sensors Journal, Volume: 20, Issue: 5, 2434 - 2439, 13 November 2019.
- Ran Tao, **Shahrzad Zahertar**, Hamdi Torun, Yi Ru Liu, Meng Wang, Yuchao Lu, Jing Ting Luo, Jethro Vernon, Richard Binns, Yang He, Kai Tao, Qiang Wu, Hong Long Chang, and Yong Qing Fu, *Flexible and Integrated Sensing Platform of Acoustic Waves and Metamaterials based on Polyimide-Coated Woven Carbon Fibers*. ACS Sens., 5, 8, 2563–2569, 20 July 2020.
- **Shahrzad Zahertar**, Hamdi Torun, Ran Tao, Pep Canyelles-Pericas, Jingting Luo, Qiang Wu and Yong Qing Fu, *An integrated platform for metamaterial-based sensing and surface acoustic wave-based acoustofluidics utilising circular interdigital transducers*. Sens. Diagn., 1, 270-279, 31st January 2022.

Conferences

- **Shahrzad Zahertar**, Ran Tao, Richard Fu, Hamdi Torun, *Microwave Sensing using Flexible Acoustofluidic Devices*. 2019 IEEE International Conference on Flexible and Printable Sensors and Systems (FLEPS), Glasgow, United Kingdom, 08 August 2019.
- **Shahrzad Zahertar**, Linzi E. Dodd, Hamdi Torun, *Embroidered Rectangular Split-Ring Resonators for Material Characterisation*. 2019 IEEE International Conference on Flexible and Printable Sensors and Systems (FLEPS), Glasgow, United Kingdom, 08 August 2019.
- **Shahrzad Zahertar**, Jiaen Wu, George Chatzipirpiridis, Olgac Ergeneman, Pep Canyelles-Pericas, Ran Tao, Yong Qing Fu, Hamdi Torun, *A Flexible PVDF-based Platform Combining Acoustofluidics and Electromagnetic Metamaterials*. 2020 IEEE International Conference on Flexible and Printable Sensors and Systems (FLEPS), Manchester, United Kingdom, 16 August 2020.

Chapter 1

Introduction

Lifestyle related diseases such as obesity, diabetes, and cancer are rising on a global scale due to poor diet, inactivity, smoking, and excessive alcohol consumption [1]. One of the main challenges remains delivering efficient healthcare that is affordable and sustainable. Enhancement of Point-of-Care Testing (PoCT) devices can significantly improve global health [2]. PoCT devices are referred to devices that can perform near patient testing without a need for laboratory testing [3]. PoCT development aims for devices that are quicker, more sensitive and provide more specific results. Emerging PoCT technologies include different platforms such as Lab-on-chip (LoC) platforms, Paper-based assays, Cell-phone (CP) based technologies. Extensive research is conducted in recent years to improve in these areas [4]. The demand for PoCT devices is increasing attributed to their widespread applications in various health conditions. Also, the number of people in need for continuous health monitoring is a factor driving the increase demand for PoCT devices. Some examples of PoCT devices include glucose sensors, blood coagulation meters and biosensors for infectious disease detection. The market for these devices has been expanding in parallel to the increase in the variety of devices. In 2019, the market for PoCT diagnostics was USD 28.5 billion and it is anticipated to reach USD 46.7 billion by 2024 [5].

A LoC device as its name suggests aims to combine the entire laboratory process onto a small chip, and therefore, usually is an integration of various platforms that are capable of liquid preparation, separation, and sensing functionalities [6]. These capabilities translate in advancement of microfluidics and biosensing technologies [4]. LoC devices are capable of sampling and process-

ing trivial amount of liquid under investigation, which can lead to faster analysis, reduced sample and solvent size, can be non-invasive, with low-power consumption, highly sensitive, and accurate. Number of elements play an important role in developing a successful LoC device including simplicity, robustness and reliability. However, there are challenges in developing a market-ready product, and there are multiple factors that need to be addressed. These include but are not limited to successful integration of various parts with different functionalities (i.e. sensing and sample collection) that comprise the whole lab-on-chip device, achieving a sustainable small size device.

The research explained in this thesis is focused to combine acoustofluidic devices with their capabilities in liquid sampling and electromagnetic metamaterials with their wireless sensing capabilities on a single geometry. In other words, the aim of this research is to develop an integrated and simplified platform of sensing and actuation employing a single structure as a potential lab-on-chip device. The objectives include designing, simulating, and characterising a single structure, which can act as a split-ring resonator (SRR) sensor in microwave frequencies, and also characterising the same structure as a surface acoustic wave (SAW) actuator in radio frequencies. In line with the aim of the research, an embroidered rectangular SRR is also introduced in this thesis for wireless sensing applications. The contents of the following chapters are as below:

In the second chapter, a literature review will be provided on sensors and acoustic wave actuators.

In the third chapter, a SAW device with curved interdigital transducers (IDTs) fabricated on a lithium niobate substrate is proposed as the first proof of concept. In the radio frequency region, different microfluid functionalities such as streaming, pumping and jetting have been explored by applying power to the electrodes of the IDTs. The fabricated device has been utilised as an SRR within 3-5 GHz, and has been investigated for its sensitivity to various concentrations of glucose inside a droplet as well as the location of the droplet relative to the device. This chapter is the first demonstration of the proposed idea and has been validated successfully.

In the fourth chapter, a circular geometry inspired by dual split-ring resonators (DSRR) on a lithium niobate surface has been tested for its capabilities in sensing and in streaming. DSRRs are commonly used sensors to lower the operating frequency of the device or can favour minia-

turisation for a target frequency by increasing the effective capacitance. Although DSRRs are among conventional designs that have been employed in metamaterials, they are not common in acoustofluidics. The fabricated device has been interrogated using a loop antenna within 3-4 GHz and has been utilised to perform various sensing experiments. At the end, the device has been characterised in radio frequencies and has been utilised for streaming of polystyrene particles inside a droplet.

In the fifth chapter, a woven carbon fiber coated with polyimide and zinc oxide was used as a flexible piezoelectric substrate and a straight conventional IDT design was patterned on top of it. The device has been investigated for temperature control in a liquid droplet utilising surface acoustic waves and also the sensitivity of the device to various UV intensities was measured in its acoustic frequency. The device was further utilised as a sensor measuring different glucose concentrations in microwave frequencies.

In the sixth chapter, straight IDTs composing a rectangular design have been patterned on polyvinylidene fluoride (PVDF) substrate. PVDF is a flexible piezoelectric substrate and applicability of the proposed concept on a flexible polymer substrate has been investigated. The S_{21} , and S_{11} frequency response of the device has been obtained in microwave and radio frequencies respectively. Different electromagnetic excitation conditions have been applied to simulate device and to characterise the potential behaviour of the device within 3-4.5 GHz.

In the seventh chapter, the concept towards developing flexible sensors have been investigated by employing embroidered rectangular SRRs. The behaviour of the device in microwave regime has been explored under various electromagnetic excitation configurations through simulations and experiments, and the device's ability in various dielectric material characterisation has been tested.

The conclusion and future directions are presented in the last chapter.

Chapter 2

Literature Review

In the following, a literature review on several types of sensors and actuators is provided.

2.1 Sensors

Significant advancements in engineering and material science have led to improvements in sensor fabrication. The sensor field is astonishingly so broad that almost every major in science plays an import role in its development. For example, ongoing improvements in material science have let scientists choose the most suitable material for the intended application while reducing the cost and enhancing reliability of the sensors. It is difficult to come up with a universal definition for sensors or to categorise them. There have been various descriptions depending on the field that the sensor was developed [1], [7], [8].

From a broad perspective a sensor can be described as “a device that receives a stimulus and responds with an electrical signal” [9]. Transducer or detector are other words that have often been synonymously and interchangeably used for sensor. Instrument Society of America has defined transducer as “A device which provides a usable output in response to a specified measurand” [10]. A measurand can be a physical, chemical or biological property or condition to be measured and a usable output can be electrical, chemical, optical, or a mechanical signal.

Sensors exist since centuries, and it is a difficult task to find the first created sensor. For example, Mercury-in-glass thermometer was created in 1714 by Daniel Gabriel Fahrenheit and it is based

on the thermal expansion of the mercury to indicate the temperature. However, first thermostat developed by Warren S. Johnson in 1883 is considered to be the first modern sensor [1], [11], as it combines thermal sensor with an electrical output which allows to control a system. Ever since, many more sensors based on various working principles have been developed. Over time, by advancement of other fields such as communication and cloud computing in parallel, sensors have become more capable and sophisticated than the first invented versions. Figure 2.1 illustrates the development of sensors over time.

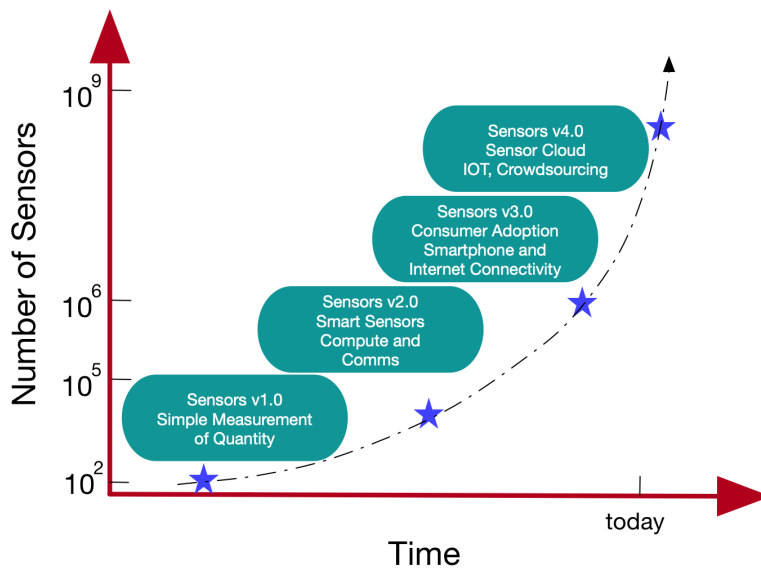


Figure 2.1: Sensor generations over time (Image is adapted from [8]).

The transition between the second and third generations of sensor, as shown in Figure 2.1, happened recently. One example is sensing in the medical industry. Up until recently, medical sensors have been predominantly employed in hospitals within expensive medical equipment. However, by progress of technology and sensors, they have become cheaper to manufacture, their size has been reduced while their accuracy has been increased. Due to these, medical sensors have become available outside hospital environment to individuals who are seeking to actively monitor their health and wellness. One example is oximeters; oximeters first were made as a standalone device and were mostly utilised in clinical settings, and miniaturisation helped to integrate them within smartwatches and wristbands that can be worn every day.

The main drivers for sensor development are factors regarding environment, health and fitness, economy, public health, national security, and Internet of Things [1]. Sensors have numerous

applications in various fields, including but not limited to product testing, quality control and assessment, food processing, air quality measurements, and medical devices. Depending on which field the sensors are used, some factors have to be considered. These parameters can be distributed into three categories [8]:

Environmental: Sensors can be built in a protected environment such as smartphones, where the major dangers are heat from nearby components or a shock from falling on the ground. On the other hand, sensors can require specific protection in order to be able to produce an accurate output. Such environmental parameters can be the resistance to temperature and humidity, the power consumption, the corrosion or the resistance to electromagnetic interferences.

Economic: Even if advancement in technology made sensors more accessible, the cost of a sensor can remain high depending on its manufacturing technique, materials used and the quality of the materials. Another major economical parameter is the sensor's lifetime; an expensive sensor can offer a cost-effective solution if that sensor can be used over a very long time, whereas some sensors such as a pregnancy test can only be used once.

Characteristics: Some notable characteristics are the accuracy, the repeatability, the sensitivity, the range and the linearity. Sensor applications influence the choice of sensors characteristics. A thermostat made for consumable market does not usually require the levels of accuracy and sensitivity as compared to its counterpart for medical device market.

2.2 Electrochemical Sensors

A working (or sensing) and a reference electrode are the key components of an electrochemical sensor. These electrodes will be placed in a medium consisting of liquid or solid electrolytes and the interaction of the electrodes with the electrolyte can be translated to a sensing mechanism. Depending on the used electrolyte, these sensors can be operational between -30°C to 1600°C [12].

The conventional liquid electrolyte-based electrochemical sensors can be typically used to monitor and measure the conductivity, pH, dissolved ions and gas in an electrolyte in lower temperatures. On the other hand, in higher temperatures, solid electrolytes are used to measure the melted metals or exhaustive gases [1].

Although high sensitivity and low power consumption are among the advantages of these types of sensors, environmental conditions such as pressure and temperature can severely affect the selectivity, sensitivity, and operational lifetime of these sensors. Also, oversaturation and cross-sensitivity can be other limitations of electrochemical sensors [1], [12].

Voltammetric and Amperometric sensors are among the most commonly used electrochemical sensors.

2.2.1 Voltammetric Sensors

Voltammetric sensors measure the current resulting due to a time-dependent potential applied to an electrochemical cell. The result is a function of the applied potential, and the plot it produces is called a voltammogram whose role is to provide information about the analysed species in the oxidation or reduction action [13]. This technique has been introduced by Jaroslav Heyrovsky in 1920 for creating the polarography technique, which awarded him the Nobel Prize in Chemistry in 1959. Early voltammetry methods were using two electrodes, while modern ones use three. The working electrode receives a time-dependent potential excitation signal while the reference electrode keeps a fixed potential. The measured current between the working electrode and counter electrode gives the voltammogram [14]. Different materials exist for the working electrode, such as carbon, silver, gold, platinum and mercury. Platinum is commonly used for the auxiliary electrode and the reference electrode usually is an Ag/AgCl or a saturated calomel electrode (SCE). When oxidizing or reducing an analyte at the working electrode, the generated current from the reduction-oxidation (redox) reactions is called a faradaic current. Voltammetric sensors are mainly used for quantitative applications. In environmental samples, trace metals detection in water samples is one major application of voltammetry to ensure the non-toxicity of water. Clinical examinations apply voltammetry to detect trace metal in urine, tissue and blood samples. Lead concentration in blood is small and voltammetry method is one of the most appropriate methods to detect lead poisoning [15].

Voltammetric sensors have been used and improved since the introduction of voltammetry technique by Heyrovsky in 1920. In 1996, Palecek improved the adsorptive transfer stripping voltammetry (AdTSV) technique by developing nucleic acid-modified electrodes for the aim of reducing DNA sample size required in the experiments [16]. Nyein et al. developed a wearable voltammet-

ric sensor to monitor ionized calcium and pH in biofluids [17].

2.2.2 Amperometric

Amperometry is another sub-category of electrochemical sensors. Amperometric sensors measure changes in current. The working electrode potential is set to a fixed value proportionally to the reference electrode and the changes in current are measured over a period of time. The current is then related to the concentration of the analyte. This type of sensor has been commonly used in biosensors and immunoassays [18]. During the electrolyse, reduction-oxidation (redox) reactions happen at the electrode surface due to the applied potential [19]. The measured current is proportional to the redox concentration of specific active species from which the sensing electrode has been designed. These sensors are used in oxygen-sensing applications, gas detection such as toxic gases (e.g. chlorine Cl), or fire detection (through detecting CO) [1].

Amperometric sensors have seen an evolution over time, which have led to improvements in their characteristics. One of the first amperometric sensors is a Clark oxygen sensor developed by L.C. Clark in 1956, made to measure dissolved oxygen in blood [20]. In this sensor, a thin electrolyte solution that separates the working electrode from an oxygen-permeable membrane is used. The oxygen goes under reduction at the cathode. The sensor delivers a current proportional to the concentration of oxygen that has been dissolved. More recently in 2001, Pividori et al. developed an amperometric biosensor to detect staphylococcus aureus, utilising an epoxy-graphite composite electrode and peroxidase with a thin nylon membrane. This method significantly reduced the time of the analysis and detection from 4-5 days to 36 hours [21]. In 2020, Muthusankar et al. developed an amperometric sensor based on phosphotungstic acid-assisted PDPA/ZnO nanohybrid composite to detect glucose. The combination of diphenylquinone diamine (DPDQ²⁺) and phosphotungstic acid anion improved the glucose oxidation, which led to a rapid sensor response of less than 2 seconds [22].

Both amperometric and voltametric sensors require direct electrical connection for measurements. This requirement is not favourable for applications where remote measurements are needed. A method of implementing remote measurements is to design sensors that can interact with electromagnetic waves. Inductive-capacitive (LC) resonators are used in wireless sensors that enable remote monitoring. Following is a literature review on LC resonators.

2.3 Inductive-Capacitive Resonators

Wireless sensors that operate within the radio frequency band of electromagnetic radiation, have attracted so much attention in recent years. Radio frequency identification (RFID) is a popular example of wireless sensors and is mainly utilised for tracking and identification purposes; In RFID sensors, a signal sent from a reader is received by a tag to be identified [23]. Radio frequency band in electromagnetic spectrum covers frequencies from 3 kHz up to 300 GHz and is divided into sub-categories based on the frequency (or wavelength) as following: low frequency, medium frequency, high frequency, ultra-high frequency, super high frequency, and extremely high frequency. The radio frequency spectrum in electromagnetic radiation is presented in Figure 2.2 [24].

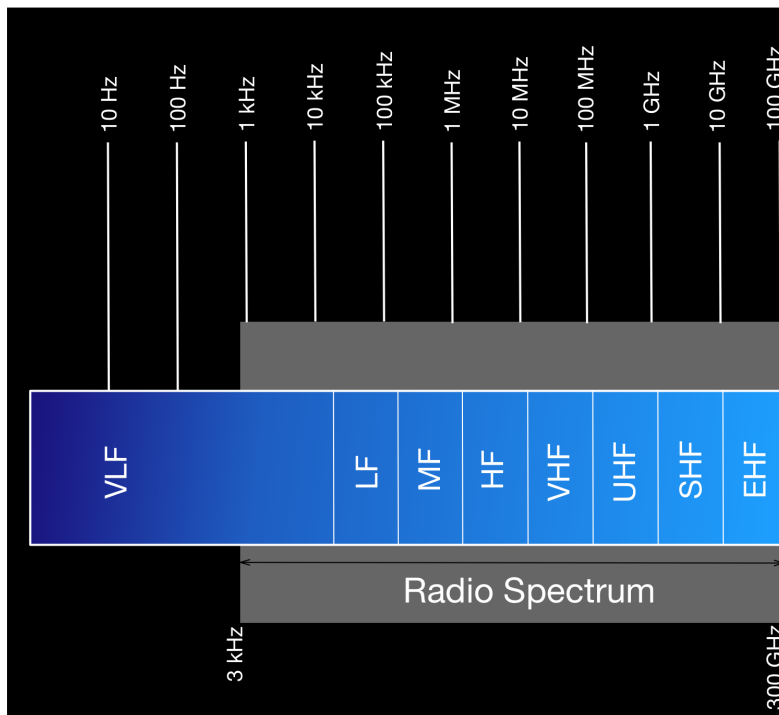


Figure 2.2: Radio and optical spectra in electromagnetic radiation (Image is adapted from [24]).

The frequencies in the range of 300 MHz to 300 GHz are also known as microwaves and usually are considered as a subcategory in radio frequency band. However, some conventional definitions separate radio and microwave frequency bands from each other. Based on the conventional definition, radio frequency (RF) band covers frequencies of 3 kHz-300 MHz and microwave band covers frequencies of 300 MHz-300 GHz [25]. The latter definition will be used throughout this thesis.

The section below covers basics of RF and microwaves.

2.3.1 Basics of RF and microwaves

RF and microwave signals propagate as electromagnetic waves. The initial investigations leading to our understanding of electromagnetic spectrum, originated from early studies in optics, electricity, and magnetism. Before the 19th century, electricity and magnetism were considered as two separate forces. However, in 1820, Ørsted found that electric currents exerted a force on magnets and in 1831, Faraday realised that changing a magnetic field induces electrical currents [26]. Maxwell concluded these discoveries in his paper “A Dynamical Theory of the Electromagnetic Field” [27] in 1864, which has led to our modern understanding of electromagnetism [26]. Electromagnetic wave is a transverse wave consisting of perpendicular vibrations of electric and magnetic fields that propagate with the speed of light through vacuum. The basis of the study and the application of the wave propagation in a medium starts with Maxwell’s equations, which show the relation between electric and magnetic fields through coupled spatial and temporal differential equations.

Maxwell’s Equations

Maxwell’s equations in differential form are presented in Table 2.1, in which \vec{D} and \vec{B} are the electric and magnetic flux densities respectively. \vec{E} and \vec{H} are the electric and magnetic fields. ρ_{enc} is the enclosed electric charge, and \vec{J} is the current.

Table 2.1: Maxwell's equations in differential format

Gauss's law	$\nabla \cdot \vec{D} = \rho_{\text{enc}}$	Relates net electric flux density to net enclosed electric charge.
Gauss's law for magnetism	$\nabla \cdot \vec{B} = 0$	Relates net magnetic flux to net enclosed magnetic charge; there are no magnetic monopoles.
Faraday's law	$\nabla \times \vec{E} = -\frac{\partial \vec{B}}{\partial t}$	Relates induced electric field to changing magnetic flux.
Ampere-Maxwell's law	$\nabla \times \vec{H} = \vec{J} + \frac{\partial \vec{D}}{\partial t}$	Relates induced magnetic field to changing electric flux and to current.

\vec{D} , \vec{B} , \vec{J} can be written as:

$$\vec{D} = \epsilon \vec{E} \quad (2.1)$$

$$\vec{B} = \mu \vec{H} \quad (2.2)$$

$$\vec{J} = \sigma \vec{E} \quad (2.3)$$

Where ϵ , μ , σ are the electric permittivity, magnetic permeability, and conductivity respectively. Derived from Maxwell's equations, the speed of light in vacuum (c), in a medium (v), and hence the refractive index (n) can be defined as:

$$c = \frac{1}{\sqrt{\epsilon_0 \mu_0}} \quad (2.4)$$

$$v = \frac{1}{\sqrt{\epsilon \mu}} \quad (2.5)$$

$$n = \frac{c}{v} = \frac{\sqrt{\epsilon\mu}}{\sqrt{\epsilon_0\mu_0}} = \sqrt{\epsilon_r\mu_r} \quad (2.6)$$

Where ϵ_0 and μ_0 are the electric permittivity and magnetic permeability of the vacuum, ϵ and μ are the electric permittivity and magnetic permeability of the medium, ϵ_r , and μ_r are the relative permittivity and relative permeability respectively.

Maxwell unified the theories of electricity, magnetism, and optics, and he formed the basis of electromagnetic-based communication. Hertz, Tesla, and Marconi continued Maxwell's work and contributed to the electromagnetic theory and the early practical applications of electromagnetic-based communications; in 1887, Hertz demonstrated that electromagnetic wave could travel distances between a basic spark-gap transmitter and receiver and also linked the speed of those waves to the speed of light. In 1891, and in 1893 Tesla demonstrated wireless power transmission and wireless telegraphy. He also filed for a US patent for a radio in 1897. In 1901, and 1902 Marconi demonstrated the trans-Atlantic communication using a kite flown antenna [26].

There are several instruments used to measure the RF and microwave signals. Since the majority of performance parameters, design constraints, and regulations for RF and microwaves are presented in frequency domain, measurements usually take the form of power versus frequency. Instruments include spectrum analysers to capture power in frequency domain, signal generators to produce carriers and modulated signals, as well as network analysers to measure S-parameters, impedances, and other frequency responses [26].

A brief introduction is given on S-parameters in section below.

S-Parameters

Several matrix representations are available for characterising circuits in different frequency regions. These include admittance parameters (Y-parameters), impedance parameters (Z-parameters), ABCD or chain matrix, scattering parameters (S-parameters) [28]. S-parameters are widely used for microwave, and radio frequency ranges.

A two-port vector network analyser, illustrated in Figure 2.3, was utilised to capture the scattering parameters of the devices proposed in this thesis.

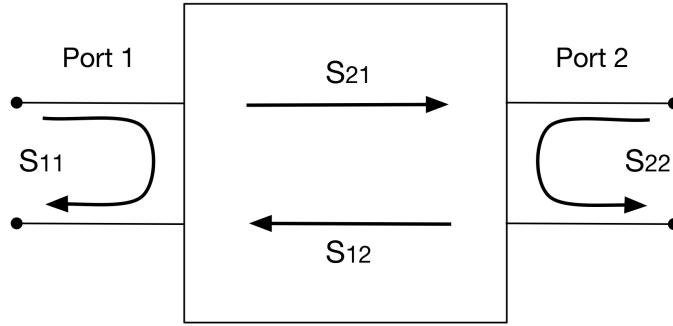


Figure 2.3: Schematic of a two-port vector network analyser.

The S matrix for a two port network analyser is:

$$S = \begin{bmatrix} S_{11} & S_{12} \\ S_{21} & S_{22} \end{bmatrix} \quad (2.7)$$

In which, elements of the matrix are complex numbers with amplitude and phase. S_{11} , and S_{22} are reflection coefficients, and measure the ratio of the reflected wave to the incident wave at port 1 and 2 respectively. S_{21} and S_{12} , are transmission coefficients representing the transmitted power from port one to two and vice versa [29].

Typically, Decibels (dB) is used when discussing power in RF and microwave systems. Decibels is a unitless measure representing the ratio of power/voltage to a reference power/voltage;

$$dB = 10 \log \frac{power}{reference\ power} \quad (2.8)$$

$$dB = 20 \log \frac{voltage}{reference\ voltage} \quad (2.9)$$

For instance, $S_{21} = 0$ dB means that all the incident power to port 1 is 100% transmitted to port 2.

One of the main categories of wireless sensors are Inductive-capacitive sensors (also known LC resonators, LC tanks). These sensors can be modelled as lumped elements with an effective inductance and capacitance, and the fundamental resonant frequency, f , can be calculated by the following equation [30]:

$$f = \frac{1}{2\pi\sqrt{LC}} \quad (2.10)$$

Where L is the effective inductance in henrys and C is the effective capacitance in farads and are determined by the geometry of the resonator and its surrounding dielectric medium. By altering one of these parameters, the frequency of the resonator can be modulated. Changes made to the inductor or capacitor with physical or chemical elements can also affect the bandwidth, or the quality factor. The delivered energy coupled with the passive components that composed the LC circuits make LC resonators a useful candidate for RF and microwave sensors which do not need batteries. In addition to these characteristics, the resonant sensors do not require any external chip or device to work, which eases their manufacturing process and allows to miniaturise them.

LC resonators have applications in various areas including medical [31]–[35], food industry [36]–[41], and environment [42]–[45]. The frequency response of the resonators can be altered when there is change in relative permittivity or permeability. This mechanism can help characterise and differentiate healthy from cancerous tissues. In food industry, resonators can be utilised to ensure the quality of the food. In environmental applications these resonators can be employed in harsh environment, where direct access to the sensing area is neither ideal nor possible.

Mannoor et al. designed an antenna with bacteria binder which allows the resonance frequency to react to the bacterial concentration. This project was mounted on tooth enamel to monitor bacteria staying on the tooth [32]. Huang et al. presented a method for food processing management. In their method, the changes of the pH level in food was captured via a flexible pH sensor lodged in a deformable batteryless RF transponder [41]. In another study, Potyrailo et al., proposed a method in order to measure the freshness of the packaged milk by monitoring bacterial load within milk package [40]. Jun et al. made a wireless and flexible gas sensor to detect volatile organic compounds such as ammonia and acetic acid. The sensor gives the possibility to measure 0.1 part per million of ammonia vapour with the difference in reflection coefficient at the resonance frequency [46].

One very common type of LC resonators is split-ring resonators (SRR), which are building blocks of metamaterials. A brief literature review is therefore presented on metamaterials and SRRs:

2.3.2 Metamaterials

Meta means “beyond” in Greek and metamaterials, as their name suggests, are artificially engineered structures that exhibit properties that are not readily available in natural materials. These properties are having negative values of permittivity and permeability simultaneously over a frequency band, resulting in a negative refractive index. The concept of negative refractive index was first conceptualised by Victor Veselago in 1967 [47]. He categorised materials as right-handed materials (RHM) and left-handed materials (LHM). Negative refractive index materials were a representation of LHM because of the formed left-handed triad by electric, and magnetic fields and the propagation vector, supporting backward wave propagation. Since this behaviour is not available in natural materials, his studies were not practiced experimentally over 30 years. In 2000, Smith et al proposed an array of two-dimensional metallic split-ring resonators and wires, and proved the existence of metamaterials experimentally based on Pendry’s work [48], [49].

Electromagnetic metamaterials are usually sub-wavelength metallic elements that present a unique capability in manipulating electromagnetic waves and can operate at certain frequencies. The early examples of metamaterials were operating at microwave frequencies and so far efforts have been made to broaden the operating frequency range to optical frequencies [50] to explore various application including biosensing [35], [51]–[55], perfect absorption [56]–[58], super lenses [59]–[61], and cloaking [62]–[64].

2.3.3 Split-Ring Resonator

Split-Ring resonators (SRRs) are basic building blocks of metamaterials. SRRs are composed of metallic rings containing one or more splits and are fabricated on a dielectric substrate. The most conventional split-ring resonators have circular or rectangular geometries [65] and are shown in Figure 2.4.

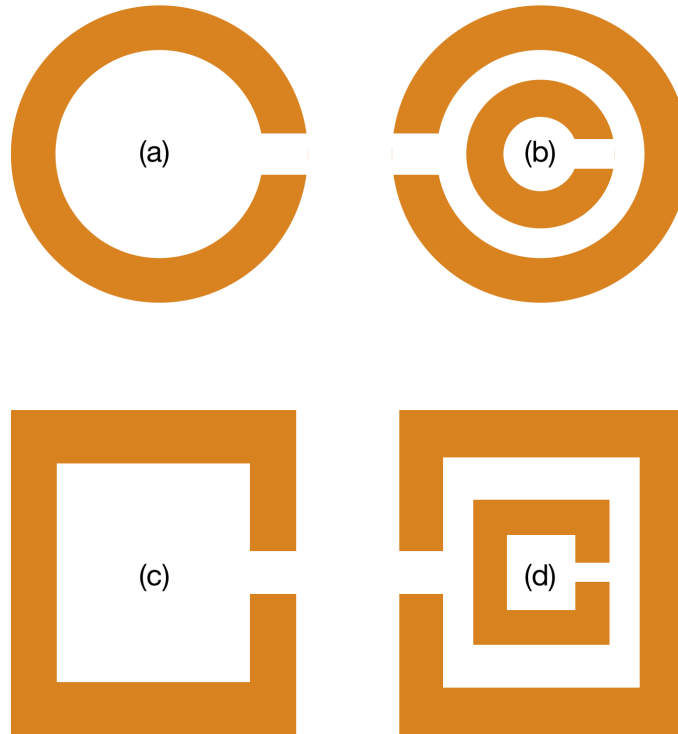


Figure 2.4: Commonly used SRRs. (a) Circular split-ring resonator (b) Circular dual split-ring resonator (c) Rectangular split-ring resonator (d) Rectangular dual split-ring resonator.

When SRRs are exposed to electromagnetic waves, they couple with the EM waves and depending on the excitation condition and the directions of the electric and magnetic fields, SRRs are capable of exhibiting different types of resonance; electric or magnetic. A magnetic resonant frequency is when a circulating current is induced inside the ring, which can happen under certain circumstances based on the electric and magnetic field directions relative to the device.

SRRs can be excited wirelessly, and when operating in their fundamental magnetic frequency, they can be modelled as a simple LC resonator. Therefore, by changing the size and dimensions of the structure, the effective inductance or capacitance changes and this effect is reflected in the value of magnetic frequency. This feature together with achievable high quality factor resonances, and simple fabrication process make them a suitable candidate for sensors.

SRRs can be utilised to sense physical, chemical, and biological properties for various applications including biomedical [66]–[70], environmental [71]–[73], and food industry [74], [75]. Torun et al proposed a circular SRR coupled with monopole antennas to monitor the interactions between heparin and fibroblast growth factor 2 (FGF-2) [53]. Lee et al developed a planar split ring resonator to detect biomolecules such as cortisol hormones and prostate cancer marker [70]. Tseng et

al fabricated a split-ring resonator sensor on a dielectric substrate, which was bio-responsive and its thickness was dependant on biomolecules and ions; consequently, it resulted in a change in the frequency response of the sensor [33]. Naqui et al. developed an alignment and 2D displacement sensor utilising coplanar wave guides loaded with SRRs [76]. Abdolrazzagli et al. designed a dual mode SRR sensor operating at microwave frequencies with the objective of eliminating the erroneous impact of relative humidity on chemical sensing of uncontrolled environments [58]. A 3-D printed SRR embedded in a cavity was proposed as a chemical sensor by Salim et al. [77]. They also developed a complementary split-ring resonator (CSRR) integrated with microfluid channels to measure low concentrations of ethanol in trivial amounts [78].

Although SRRs are desirable for non-invasive, reliable, real-time and wireless sensing, they lack the capability of manipulating fluids, a requirement for liquid sampling. So, SRRs cannot effectively form a LoC device on their own.

A conventional type of actuators that have been explored for their capability in fluid manipulation is based on acoustic waves. Following is a literature review on this type of actuators.

2.4 Acoustic Wave Actuators

Over the past few decades, microfluidics has inspired researchers in different fields. It has shown promising solutions for fluid sampling related problems by reducing the sample size needed for analysis. Microfluidic manipulation is performed at the micro-scale level in micro-channels or by use of sessile droplets. The objective of using this technology in different fields is replacing each course of action in macro-scale level by a micro-scale equivalent and uniting the components without undermining their merits. Despite dealing with small volumes, being cost-effective, and their ability in processing and control, microfluidics have limitations in their traditional form when it comes to actuation, as they rely on an external bench-top pneumatic pump linked by a tangle of tubes [79]. Operation on such a system with hand-held version is challenging for both experts and non-experts in laboratories. Bioassays are one of the most noteworthy applications used for lab-on-chip devices, however, these biological assays need mixing. Some solutions have been introduced such as passive mixers [80]. Although they can provide solutions for some cases, they need intricate architectures. According to Sackmann et al., it is not enough for microfluidics to

emulate the steps at macro-scale level into micro-scale levels and achieve an equivalent performance; microfluidics must do better than that in order to compete with larger technologies [81]. In the following, it will be discussed how actuation via the use of acoustic waves can deal with such problems and help fulfil the promise of microfluidics.

Acoustic waves operate based on vibration. Vibration can manipulate the particles both within fluids and gases; this feature has been studied by Chladni et al., Kundt et al., and Faraday et al. and have affected other scientific works later done [82]–[84]. Fluid actuation with the help of acoustic waves are demanding in terms of analysis, however, it is practical since it only requires a small hardware for operation providing broad actuation forces and force gradients.

Acoustic waves have been utilised for decades and have applications in various fields, ranging from communications to automotive and environmental sensing [85]–[89]. Acoustic wave-based sensors and actuators rely on piezoelectric property of their substrate; applying an alternating current (AC) or radio frequency (RF) excitation to electrodes patterned on a piezoelectric material generates an acoustic wave that propagates in the direction perpendicular to the surface of the material into the bulk medium (bulk acoustic wave, BAW) or along the surface of the material (surface acoustic wave, SAW). Figure 2.5 shows the different modes of BAWs and SAWs (adapted from [90]).

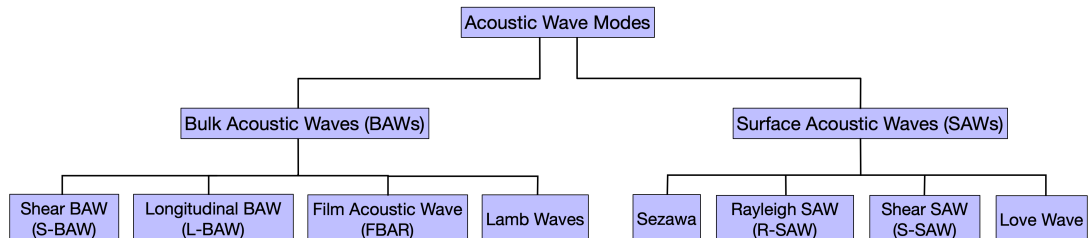


Figure 2.5: Key modes of BAWs and SAWs (adapted from [90])

A literature review is provided on working principles of acoustic waves, Bulk Acoustic Waves, and Surface Acoustic Waves respectively with the focus being centred on SAWs.

2.4.1 Working Principles: Piezoelectric Effect

The piezoelectric effect is the generation of an electric charge by a crystal that is under strain or pressure. This phenomenon was discovered by Pierre and Jacques Curie in 1880 when applying a mechanical stress to multiple types of crystal. The converse piezoelectric effect, i.e. applying

a mechanical stretch instead of pressure, was mathematically derived by Lippman in 1881, and it was verified by the Curie brothers during the same year [91]. A few decades had to pass before a practical use was found. In 1917, Professor P. Langevin applied the piezoelectric effect onto cut plates of quartz (SiO_2) in order to analyse the electrostatic properties of seawater, which is the base of the sonar development [92].

When applying a mechanical stress onto a piezoelectric material, the dipole moments get self-reorientated, causing electric polarization variations of molecules. These variations produce an electrical potential on the surface material. The opposite is also true; applying an electrical potential on the piezoelectric material results in a deformation of the material structure [93]. In 1927, A. Meissner proposed a simplified explanatory model of the phenomenon with a quartz crystal, as shown in Figure 2.6 [94].

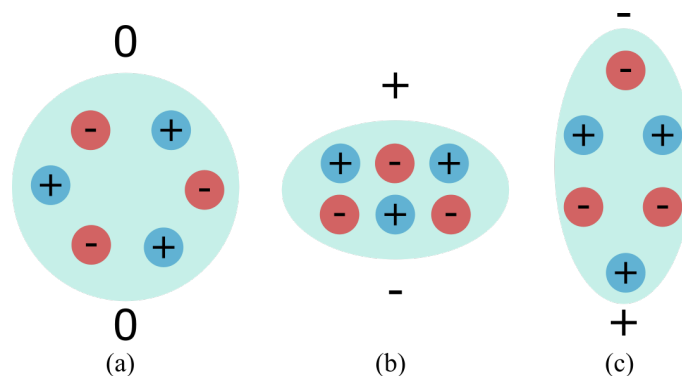


Figure 2.6: Scheme of the piezoelectrical effect on a quartz crystal. (a) represents a cut in a quartz crystal at equilibrium moments. (b) represents a mechanical pressure applied. (c) represents a mechanical stretch applied.

Piezoelectric effect can only happen on materials with specific characteristics. The material has to be polarized and should present a spontaneous polarization when a mechanical stress is applied, as shown in Figure 2.6. These include crystals like quartz, or man-made ceramics that are artificially polarized. Some polymers like polyvinylidene fluoride (PVDF) also possess a piezoelectric property. On a more general aspect, all ferroelectric materials and pyroelectric materials are piezoelectric materials, and so have high piezoelectric capability [95], [96]. At the beginning of piezoelectric research, natural crystals such as quartz were used. Langevin's research for sonar application was reused later by modifying the quartz with Rochelle salt crystals which have better electromechanical coupling properties [97], [98]. As research in this field became more important, the need of having an efficient piezoelectric material at lower cost and with better physical

properties emerged. Synthetic piezoelectric materials with higher piezoelectric performance have been researched, with improved reliability and reproducibility [99]–[101]. Artificially polarized ceramics are among the mostly used materials in the piezoelectric field nowadays [94], [102]–[104].

Piezoelectric sensors have advantages compared to other sensor types. Their manufacturing process makes them easy and low-cost to fabricate, with durable quality and advanced mechanical properties. Piezoelectric sensors are called passive sensors, or self-generating sensors, meaning that they do not require an external power source in order to work [7]. This is an important advantage to include them in biosensors and more specifically wearable biosensors. An example can be a sweat metabolites monitor [105]. This proof-of-concept of self-powered sensor still needs to be tested on the accuracy and lifespan aspects. Saravanakumar et al. researched a self-powered piezoelectric sensor that can measure pH [106], [107]. Karki et al. compared wearable biosensors materials for heart rate and respiration cycle measurements with piezoelectric PVDF and electromechanical film [108], [109]. Other studies have experimented harvesting energy from physical motion with piezoelectric sensors on wearable devices [105], [110], [111].

2.4.2 Bulk Acoustic Waves

Bulk acoustic waves (BAW) propagate through the bulk of the piezoelectric material. The most common BAW devices are Quartz Crystal Microbalances (QCM), for which sensing principle has been explained in 1959 by Sauerbrey [112]. QCM are made of quartz crystal sandwiched between two metallic electrodes, typically gold. The wave mode in QCM is a Thickness Shear Mode (TSM), which can be used in liquid and dry environments. In order to sense the measurand, QCM applies the gravimetric method of mass change [113]. The resonant frequency changes when the mass of a molecule, absorbed or deposited, is applied on the QCM surface. Using Sauerbrey equation, it is possible to obtain an estimation of the change in frequency [113]:

$$\Delta f = -\frac{2(f_0)^2}{A\sqrt{u_q p_q}} \Delta m \quad (2.11)$$

Where Δf is the change in resonant frequency (Hz), f_0 is the unloaded crystal's resonant frequency (Hz), A is the active area of the QCM, u_q is the shear modulus of the quartz, p_q is the

quartz density (g/cm^3) and Δm is the deposited molecule mass (g) [113].

Another wave mode for BAW is called Shear BAW (SBAW). This mode consists of shear horizontal BAWs for which the propagation is just beneath the substrate surface.

One other type of BAWs that is used for sensing applications is Film Bulk Acoustic Resonator (FBAR), an example of which is shown in Figure 2.7. Sharing similar structure with the QCM, the advantage of FBAR is its dimensions that are much smaller. The operating frequency of FBARs can range from sub GHz up to tens of GHz. FBARs also have the advantages of being highly sensitive and their manufacturing process is low-cost [114]. However, having a small size impacts the FBAR with such a sensitivity that detects many different parameters and therefore adds more noise in the obtained signal.



Figure 2.7: Schematic of a back trench Film Bulk Acoustic Resonator (FBAR).

2.4.3 Surface Acoustic Waves

Surface acoustic waves (SAWs), also known as Rayleigh waves, were initially reported by Lord Rayleigh back in 1885 [115]. These mechanical waves need a medium to propagate. The propagation will be done parallel to an elastic surface where high energy concentration can be found [116]. SAWs not only propagate along the symmetrical crystal axes but they can also propagate along different rotated cuts. This will enable many applications including SAW filters. These filters are widely used in wireless communication systems to provide sharp and clean signals [79].

By implementing interdigital transducers (IDTs) on a piezoelectric substrate, it is possible to generate SAWs [79]. One important factor in the design of a SAW device is the number of fingers, which affects its quality factor. A common SAW device employs at least one set of interdigital transducers assembled on the surface of a piezoelectric substrate [117]. Generally interdigital transducers enable high frequency SAWs. The minimum working frequency of a SAW device is limited by the substrate thickness. The frequency of generated waves is typically in the order of tens to hundreds of MHz, which makes it suitable to work with microfluidics. SAW devices

are made up of anisotropic materials and their crystal structure orientation specifies the type of the wave form they will generate. Power efficiency is an important issue while designing SAW devices which can be improved by adding reflectors in the design. Reflectors are the replication of fingers deployed one wavelength away from them [79].

The most commonly used substrates in surface acoustic wave devices include quartz, lithium niobate (LiNbO_3), lithium tantalate (LiTaO_3), ZnO, cadmium sulfide (CdS) and gallium arsenide (GaAs) [118].

SAWs can be utilised for both actuation and sensing, which will be discussed further in more detail in the following subsections.

Droplet Actuation

By applying RF power to the electrodes of a SAW device at its acoustic frequency, surface acoustic waves are generated and will travel without much attenuation on the piezoelectric substrate. However, when generated SAWs encounter a liquid droplet, the waves are dissipated into the droplet and seem to quickly attenuate in the droplet and the substrate [79]. This mechanism is illustrated in Figure 2.8.

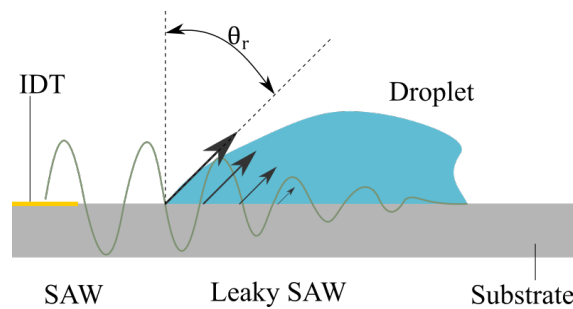


Figure 2.8: Schematic view of SAWs propagating through a droplet. The energy is dissipated within the liquid at the Rayleigh angle.

The intensity of SAWs that are “leaked” in the droplet diminishes and are therefore called Leaky SAWs (LSAWs). These LSAWs travel through the liquid with a streaming angle named the Rayleigh angle θ_r .

Rayleigh angle is calculated using the Rayleigh SAW velocity onto the substrate, ν_S , and using the SAW velocity within the liquid, ν_L , by the following equation:

$$\theta_r = \arcsin\left(\frac{\nu_L}{\nu_S}\right) \quad (2.12)$$

This decay factor happens along a certain length onto the piezoelectric substrate. This length is called the attenuation length, and is calculated by the following equation:

$$\alpha^{-1} = \frac{\rho_S \nu_S^2}{\rho_L \nu_L f} \quad (2.13)$$

Where α^{-1} is the attenuation length, ρ_S and ρ_L are the densities of substrate material and liquid respectively. The attenuation of the SAW along the Rayleigh angle is even more drastic and follows another equation as below:

$$\beta^{-1} = \frac{\rho_L \nu_L^3}{4\pi^2 f_{saw}^2 \left(\frac{4}{3}\mu + \mu'\right)} \quad (2.14)$$

Where μ and μ' are the shear and bulk viscosities of the fluid respectively [79].

The acoustic wave that is leaked into the droplet will set up pressure fields along the Rayleigh angle. At lower applied powers above a certain level, an internal streaming inside the droplet will emerge. By further increasing the RF power applied to the electrodes, the leaked SAW energy intensifies, and the droplet will start to lean towards the direction of the Rayleigh angle. If the leaked surface power reaches a certain threshold where it overcomes the pinning force between the droplet and the substrate, then the droplet can be pumped. Increasing the applied power even further can lead to jetting and the nebulisation of the droplet.

Examples from literature on these microfluidic functions are presented in more detail in the following sections:

Streaming

Streaming is a phenomenon happening when acoustic waves of high oscillation and high amplitude are absorbed in a fluid. It can be used for pumping and mixing applications in a continuous flow and digital microfluidics [119], [120].

Wixforth developed a microfluid processor and explored internal streaming inside very small

amounts of sessile droplets (\sim tens of nanoliter) employing SAWs [121]. Acoustic streaming has multiple advantages such as speeding up biochemical reactions as well as improving the speed of hybridization reaction when examining DNA and protein [122]–[124].

When particles flow inside a droplet, the common shapes are vortexes that are formed in a butterfly pattern as shown in Figure 2.9. The shapes depend on multiple factors such as the number and types of IDTs used, the hydrophobicity of the substrate, and the size of the droplet [90].

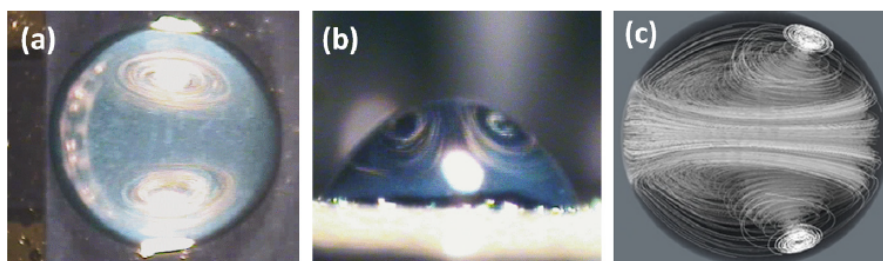


Figure 2.9: Flow patterns of acoustic streaming in a droplet induced by ZnO/Si SAWs: (a) Top view, where a single IDT on the left causes the butterfly streaming patterns inside the droplet; (b) the front-side view of butterfly streaming patterns induced by the ZnO/Si SAW; (c) the corresponding simulated streaming pattern using finite volume software induced by a SAW launched from the left [90].

The acoustic streaming also contributes to moving smaller droplets on a surface. This can be seen in Figure 2.10, where two droplets of water are mixed together using a single set of IDTs to move and mix the droplets. The transportation of a droplet depends on the same factors affecting the mixing shapes, and it also depends on the RF power applied.

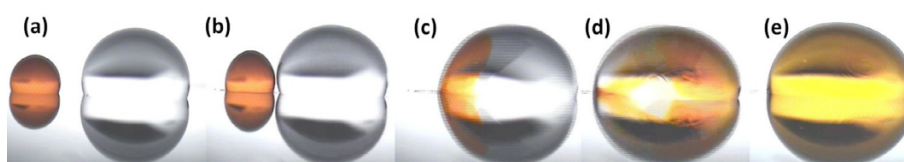


Figure 2.10: Acoustic mixing of a water droplet with a red dye droplet at different intervals induced by a ZnO/Si SAW device with the SAW launched from the left side [90].

Kulkarni et al. used SAWs to explore the in-gel sample processing by mixing reactants in a $40 \mu\text{L}$ droplet until all the reactions happened [125]. This process revealed to be substantially faster than conventional methods as all reactions were completed in dozens of minutes. Frommelt et al. developed a traveling SAW (TSAW)-based droplet mixing device using two tapered IDTs [126]. They observed that the SAW amplitude and frequency have a direct impact on the mixing speed, and that change in the input signals would modify the flow patterns.

Pumping

A challenge in pumping of the micro-scale sessile droplets in a LoC device is to avoid evaporation of the droplet during this process [127]. Although, pumping is mostly performed utilizing continuously filled channels, digitised pumping of sessile droplets can be achieved using SAW actuators. When the leaked surface acoustic wave inside the droplet reaches certain level, the droplet is deformed and leaned in the direction of the Rayleigh angle. At this point, further increasing the applied power to the electrode will cause the LSAW to overcome the pinning force between substrate and the droplet, and consequently, pumping will be achieved.

Wixforth et al developed a microfluid processor with predefined trajectories for pumping droplets in nanolitre range [128]. Renaudin et al. demonstrated that the pumping of a droplet depends on the RF power applied and that the threshold power in hydrophobic surfaces to achieve pumping is lower [129]. Actuation of sessile droplets utilising low powers was explored by Baudoin et al. [130]. They realised that vibrating the droplet can substantially reduce the amount of power required for pumping. This process can play an important role, where it is necessary to keep the temperature of the droplet constant during the pumping process. Ai et al. explored the effect of focused IDTs on pumping [131]. They observed that focused IDTs translate the droplet on the focal distance, five times faster than straight IDTs. Figure 2.11 illustrates the splitting of a $3\ \mu\text{L}$ droplet into two equal-size sub droplets and their translation. In this experiment, two SAW devices fabricated on a lithium niobate substrate were placed on the opposite side of each other with an offset [132].

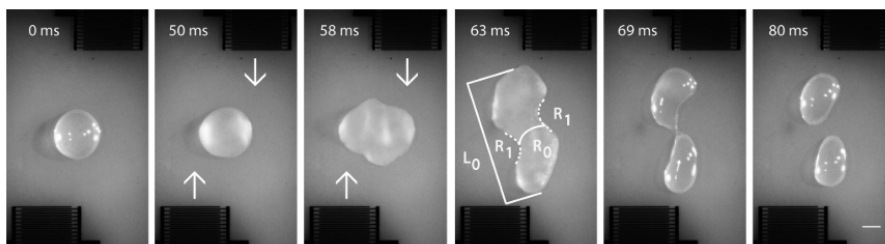


Figure 2.11: Splitting and translation of $3\ \mu\text{L}$ droplet into two $1.5\ \mu\text{L}$ droplets over time [132].

Jetting

Generally, the inertial force should overcome the surface tension force so that jetting can happen and can depend on various factors including the viscosity and size of the droplet. Applying a

high acoustic power on a SAW device electrode combined with hydrophobicity of the surface, can overcome the surface tension and jetting of a small droplet into the air will be possible [133]. The concept of droplet jetting using SAW was proposed by Shiokawa et al. in 1990 [134]. They observed that, when high-intensity acoustic waves were generated on a SAW device, small liquid droplets were ejected at Rayleigh angle from the original droplet. Figure 2.12 represents an example of jetting, in which two IDTs placed at opposite sides of the droplet are used to generate the SAWs. SAWs are pushing the droplet in its centre, and the Rayleigh angle applies a vertical force. Hence, the droplet is deformed and elongated upward, until it is entirely ejected from the SAW device. This jetting solution presents an advantage compared to traditional nozzle-based droplet ejector as they would be more cost-effective [90]. Another method of droplet jetting is to use circular IDTs. Although this solution has a higher energy efficiency, continuous droplet jetting is not easily feasible by this method, as it requires the droplet to be precisely placed at the centre of the IDTs. However, in the aforementioned case with two opposite IDTs, a microchannel can be integrated on the device to provide continuous flow of the droplet [90].

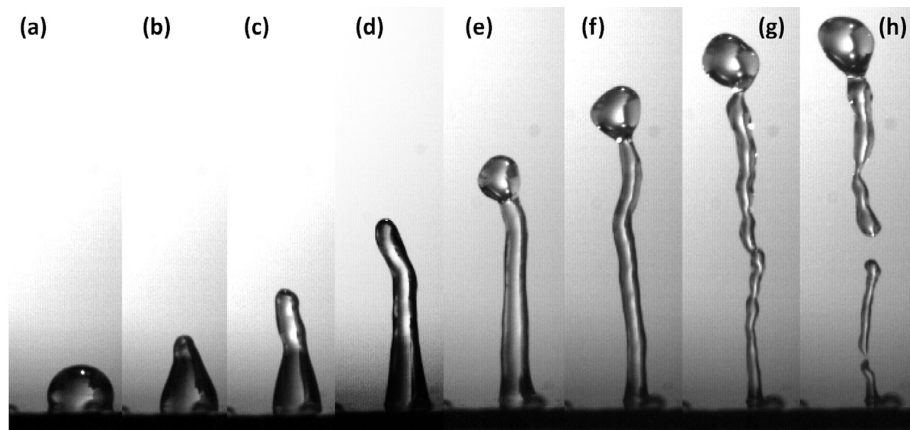


Figure 2.12: Vertical liquid jetting of a $2 \mu\text{L}$ droplet actuated by ZnO/Si SAWs from two opposite IDTs. The SAWs are launched from two sides of the droplet, thus the droplet is pushed up from both sides by the opposing waves at the Rayleigh angle, i.e., (a) to (c). The leaky waves propagate inside the droplet and reach the surfaces of the deformed liquid and then are reflected back into the liquid, thus further pushing the liquid upwards, i.e., (c) to (f). The vertical jetting of the droplet continues until the elongated liquid beam break up into small droplets, i.e., (g) and (h) [90].

Multiple research groups have studied jetting technique to improve its efficiency. Bennes et al. investigated the choice of the substrate [135]. They observed that when a hydrophilic substrate is used, the jetting would produce a spray. However, a proper jet is produced when the surface of the substrate is hydrophobic. Later, Pang et al. applied different thickness of ZnO and ultrananocrys-

talline diamond (UNCD) on the substrate to observe their possible effect on jetting [136]. The UNCD improved the energy transfer between the substrate and the droplet. Darmawan and Byun observed that super hydrophobic substrates have a higher droplet detachment time compared to hydrophobic substrates because of the SAW propagation area [137].

Sensing with Acoustic Waves

SAW devices can be employed as sensors, as SAW has high sensitivity to different types of perturbations such as mechanical, chemical or optical stimuli [138], [139]. The main technique to sense with acoustic wave devices is to measure the variations of the acoustic phase velocity. This velocity is linked to the resonant frequency by the following equation [90]:

$$f_r = \frac{\nu}{\lambda} \quad (2.15)$$

Where f_r is the resonant frequency, ν is the acoustic phase velocity and λ is the wavelength. Many factors can induce a change in the acoustic phase velocity, such as mass loading, conductivity, temperature, and pressure. Their impact is modelled in the following equation:

$$\begin{aligned} \frac{\Delta f}{f_0} &= \frac{\Delta \nu}{\nu_{acoustic}} \\ &= \frac{1}{\nu} \left(\frac{\partial \nu}{\partial m} \Delta m + \frac{\partial \nu}{\partial \sigma} \Delta \sigma + \frac{\partial \nu}{\partial T} \Delta T + \frac{\partial \nu}{\partial c} \Delta c + \frac{\partial \nu}{\partial \varepsilon} \Delta \varepsilon + \frac{\partial \nu}{\partial P} \Delta P \dots \right) \end{aligned} \quad (2.16)$$

Where ν is the acoustic phase velocity, m is the mass load, σ is the conductivity, T is the temperature, c is the mechanical constant, ε is the dielectric constant, and P is the pressure. This equation assumes that all external factors are small.

Two different structures exist to use a SAW device as a sensor, one being delay line structures and the other being SAW resonators [140]. Delay line structures are used to analyse the velocity of the surface waves altered by a measurand. The velocity follows a round trip delay of the readout signals [141]. Multiple reflectors are placed at different distances from the IDT in order to track this delay.

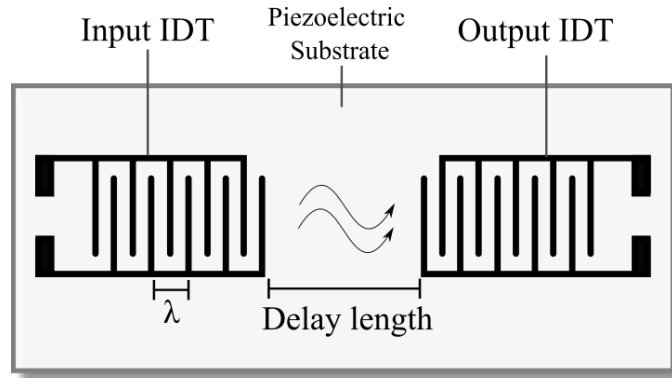


Figure 2.13: Surface Acoustic Wave configured as a delay line (adapted from [140]).

In a delay-line structure, the SAW-sensor will generate acoustic waves from an IDT emitter to another IDT receiver. This configuration can be seen in Figure 2.13, where a 2-ports SAW configuration is shown. It is possible to use a 1-port SAW configuration too. In this configuration, one SAW port, is acting as a wave emitter and receiver, and is surrounded by reflectors [142]. Such configuration can be seen in Figure 2.16.

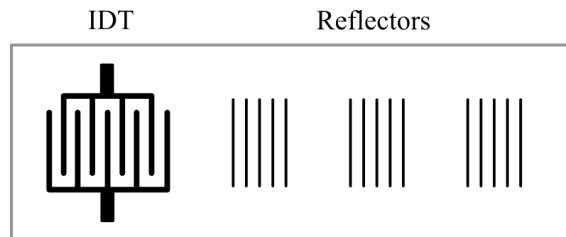


Figure 2.14: One-port SAW reflective delay line (adapted from [141]).

SAW resonators act as LC resonators, in which the measurand has influence on the resonance frequency. Multiple SAW resonators can be used on a single system to improve the sensing sensitivity and robustness. Buff W. et al. were the first to investigate the use of two SAW resonators with a differential evaluation [143]. This configuration cancels out the possible disturbances coming from impedance changes, as well as improving the signal quality.

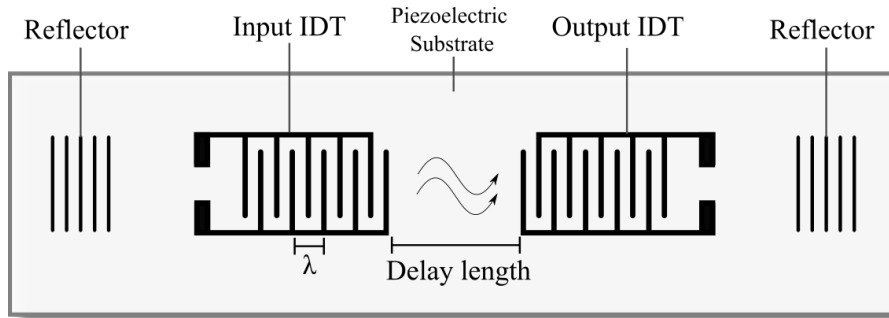


Figure 2.15: Surface Acoustic Wave configured as resonator (adapted from [140]).

A one-port SAW resonator is illustrated in Figure 2.16

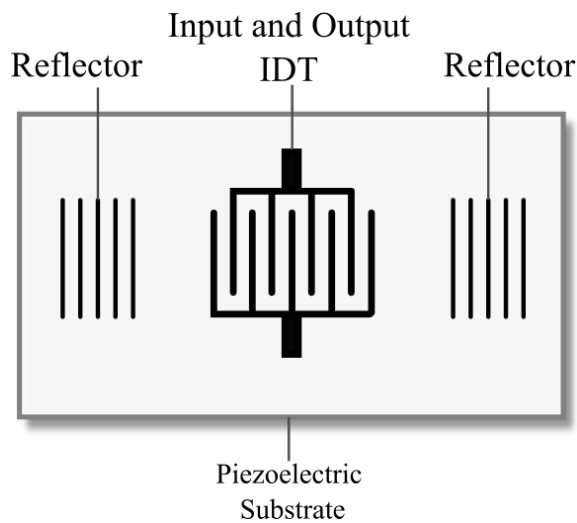


Figure 2.16: One-port SAW resonator device (adapted from [141]).

The parameters and mode of the SAW-based sensors are to be chosen depending on the application. These parameters, such as wavelength of the IDTs will have a direct influence on the sensor resonant frequency as well as its sensitivity [90].

2.4.4 Design considerations in SAWs

The selection of the piezoelectric film plays an important role in the design and successful integration of SAW devices for sensing and actuation purposes. There are several factors to consider for the choice of the piezoelectric film. These mainly include microstructure and piezoelectric properties, fabrication considerations, and the intended application. More details are explained below [90]:

Microstructure properties:

The film must have strong texture, dense structure with low porosity. Also, the film's microstructure and thickness must be uniform. Other parameters include good stoichiometry (e.g. Zn/O or Al/N ratio), and high crystallinity with low defect density.

Piezoelectric properties:

The film must have the following characteristics: high electromechanical coupling coefficient (k^2), good thermal stability (low thermal coefficient of frequency, or velocity), high quality factor, with low acoustic loss and low damping.

Fabrication considerations:

Low film stress, easy deposition and good adhesion of the films on various substrates, cost, reproducibility, compatibility with other technologies e.g. CMOS/MEMS, easy patterning/processing/etching of the films are among the considerations, which are needed to be taken into account in the fabrication step.

Microfluidics applications:

For microfluidic actuation purposes, the following characteristics for the film are needed to be taken into consideration: being chemically inert, robustness or flexibility based on the intended use, easy surface modification, ability to handle high powers without causing fractures in the structure, hydrophilicity/hydrophobicity of the surface (e.g. the surface needs to be hydrophobic for pumping of microfluids), compatibility with other technologies for integration, optically accessible to monitor the process.

Sensing applications:

High sensitivity, selectivity, resolution, and low noise levels are important for sensing applications. In general, the following characteristics are taken into consideration for design of the sensors: high quality factor (Q), low environment dependency, high thermal stability, substrate flexibility/rigidity depending on the application, fast response and low hysteresis. If the sensor is designed for bio-applications, additional parameters such as biocompatibility, easy surface

modification/functionalisation, and chemical inertness are also considered. Some of the quantitative measures, explained earlier in the design considerations, are defined in more detail below [90]:

Responsivity

The Responsivity of a sensor, R , to any external perturbation x is defined as:

$$R = \lim_{\Delta x \rightarrow 0} \frac{f(x + \Delta x) - f(x)}{\Delta x} = \frac{df}{dx} \quad (2.17)$$

where it reflects the shift in frequency caused by Δx or the variation factors such as temperature, pressure, mass, density, viscosity or conductivity.

Quality Factor, Q:

The quality factor, Q , can be utilised as an indication of the performance of acoustic wave resonators. The quality factor is influenced by ohmic losses in contacts and electrodes, acoustic wave leakage into the substrate, dielectric losses of the piezoelectric films, cracks and defects, surface/interface roughness.

The quality factor can be experimentally obtained by the well-known 3-dB method as below:

$$Q = \frac{f_0}{\Delta f_{-3dB}} \quad (2.18)$$

where Δf_{-3dB} is the bandwidth at -3dB of the resonant peak of the admittance at f_0 .

The electromechanical coupling coefficient, k^2 :

Electromechanical coefficient, k^2 , is a function of piezoelectric coefficient of the acoustic wave resonator and is defined as below:

$$k^2 = \frac{\epsilon_{31}^2}{c_{11}\epsilon_{33}} \quad (2.19)$$

where ϵ_{31}^2 is electric field, c_{11} is the elastic constant of the material, and ϵ_{33} is the permittivity at

a constant strain. Electromechanical coefficient of a SAW device can be experimentally obtained by:

$$k^2 = \frac{\pi}{4N} \left(\frac{G}{B} \right)_{f=f_0} \quad (2.20)$$

where N is the number of SAW device finger pairs; G is the conductance (real part) and B is the susceptance (imaginary part) of the electrical admittance Y ($Y = G + jB$), at the central frequency, respectively. Using a network analyser, G and B values can be extracted from the Smith Chart of the transmission or reflection coefficients at the central resonant frequency.

The Effect of IDT Design in SAWs

The SAW devices shown in Figures 2.13 and 2.16 generate acoustic waves in two directions using standard bidirectional IDTs. While this is useful in a one-part SAW configuration, there is an energy loss when using a two-port SAW configuration. Hanma and Hunsinger researched a single-phase unidirectional transducer (SPUDT), which uses unidirectional IDTs that have built-in reflectors among the fingers to force the acoustic waves to go into one direction [144]–[146]. An example of a SPUDT can be seen in Figure 2.17. Their disadvantage is that the total SAW energy is reduced compared to standard IDTs. They are an essential component for microfluidics applications as they maintain the SAW sensor at the most optimal operation conditions.

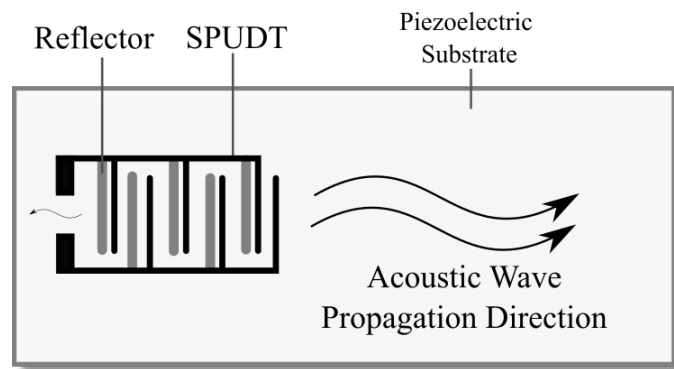


Figure 2.17: Single-phase unidirectional transducer design scheme.

In slant IDTs the operating frequency can continuously vary as a result of the modification in electrode periodicity. Slanted IDTs have the advantage of changing the moving direction of a droplet by changing the operating frequency continuously. Their disadvantage is their broad bandwidth.

An schematic of these IDTs is shown in Figure 2.18(a). To improve the mixing and pumping characteristic of a SAW device, circular IDTs can be implemented. Their design produces higher sensitivity and resolution in sensing by focusing acoustic energy in its centre. Figure 2.18(b) shows an illustration of circular IDTs [90].

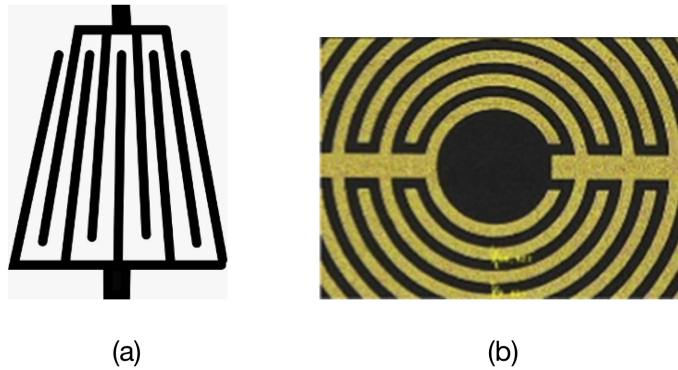


Figure 2.18: (a) Slant IDT design scheme (b) Circular IDTs [90].

Film thickness and dispersion effects

Thin film acoustic wave devices have considerable dispersion effects; The thickness of the film influences the quality factor, acoustic wave velocity, resonant frequency, and electromechanical coefficient significantly [147]. The ratio between the wavelength and the thickness of the thin film saw devices is a dominant factor in determining the wave modes and their velocities. This can be characterised by normalised thickness, which is hk , where h is the film thickness, and k is the wave vector ($k=2\pi/\lambda$) [90].

For thin film SAW devices, if the piezoelectric film thickness is larger or comparable to the wavelength of the SAW, the waves will mainly propagate inside the piezoelectric layer. Therefore, the acoustic wave velocity will be that of the Rayleigh waves for the thin film layer. For example, the speed of the wave would be 2800 m/s for ZnO, and 5600 m/s for AlN). On the other hand, if the film thickness is much smaller than one wavelength, the SAW energy will be mainly dissipated in the substrate, and thus, the wave velocity would be that of Rayleigh velocity of the substrate material. Therefore, the velocity of the SAW devices can be tuned between acoustic velocities of thin film or substrate material by adjusting the ratio between the film thickness and the wavelength of the SAWs. There is a cut-off film thickness in the order of tens of nanometres or $\sim 10\%$ of wavelength of the SAW, below which no significant SAW can be generated. This is due to the

very low electromechanical coupling coefficient and limited piezoelectric effect for very thin films [90].

Furthermore, by increasing the film thickness 1^{st} and higher modes of Sezawa modes can be detected [90], [148], [149]. Sezawa modes can also be generated through multi-layered device designs, where the acoustic wave velocity in the substrate is higher than that of the top layer [90], [150], [151]. However, multi-layered structures would be more complex as the material and thickness of each layer will have an impact on the wave propagation [152]–[155].

Sezawa waves exhibit higher phase velocities and resonant frequencies compared to Rayleigh waves for a given thickness, which would render the SAW device more suitable for higher frequency applications [90], [156]. For example, for biosensing applications, higher order Sezawa mode with higher frequency shows better sensitivity compared to Rayleigh mode.

References

- [1] M. J. McGrath, C. N. Scanaill, and D. Nafus, *Sensor Technologies: Healthcare, Wellness and Environmental Applications*, en. Apress, 2013, ISBN: 978-1-4302-6013-4. DOI: 10.1007/978-1-4302-6014-1. [Online]. Available: <https://www.springer.com/de/book/9781430260134> (visited on 01/16/2021).
- [2] P. Yager, T. Edwards, E. Fu, *et al.*, “Microfluidic diagnostic technologies for global public health,” en, *Nature*, vol. 442, no. 7101, pp. 412–418, Jul. 2006, Number: 7101 Publisher: Nature Publishing Group, ISSN: 1476-4687. DOI: 10.1038/nature05064. [Online]. Available: <https://www.nature.com/articles/nature05064> (visited on 07/06/2020).
- [3] S. K. Sia and L. J. Kricka, “Microfluidics and point-of-care testing,” en, *Lab on a Chip*, vol. 8, no. 12, pp. 1982–1983, Dec. 2008, Number: 12 Publisher: The Royal Society of Chemistry, ISSN: 1473-0189. DOI: 10.1039/B817915H. [Online]. Available: <https://pubs.rsc.org/en/content/articlelanding/2008/lc/b817915h> (visited on 01/16/2021).
- [4] S. K. Vashist, P. B. Lippa, L. Y. Yeo, A. Ozcan, and J. H. T. Luong, “Emerging Technologies for Next-Generation Point-of-Care Testing,” en, *Trends in Biotechnology*, vol. 33, no. 11, pp. 692–705, Nov. 2015, Number: 11, ISSN: 0167-7799. DOI: 10.1016/j.tibtech.2015.09.001. [Online]. Available: <http://www.sciencedirect.com/science/article/pii/S0167779915001870> (visited on 07/06/2020).
- [5] *Point of Care/POC Diagnostics Market worth \$46.7 billion by 2024*, Jan. 2021. [Online]. Available: <https://www.marketsandmarkets.com/PressReleases/point-of-care-diagnostic.asp> (visited on 01/16/2021).
- [6] L. R. Volpatti and A. K. Yetisen, “Commercialization of microfluidic devices,” en, *Trends in Biotechnology*, vol. 32, no. 7, pp. 347–350, Jul. 2014, Number: 7, ISSN: 0167-7799.

DOI: <https://doi.org/10.1016/j.tibtech.2014.04.010>. [Online]. Available: <http://www.sciencedirect.com/science/article/pii/S0167779914000870> (visited on 07/06/2020).

- [7] N. R. Council, *Expanding the vision of sensor materials*. National Academies Press, 1995, ISBN: 0-309-58743-3.
- [8] R. C. Dorf, *Sensors, Nanoscience, Biomedical Engineering, and Instruments: Sensors Nanoscience Biomedical Engineering*, English, 1st edition. Boca Raton: CRC Press, Jan. 2006, ISBN: 978-0-8493-7346-6.
- [9] J. Fraden, "Sensor Characteristics," en, in *Handbook of Modern Sensors: Physics, Designs, and Applications*, 4th ed., New York: Springer-Verlag, 2010, pp. 13–52, ISBN: 978-1-4939-0040-4. DOI: 10.1007/978-1-4419-6466-3. [Online]. Available: <https://www.springer.com/gp/book/9781493900404> (visited on 01/16/2021).
- [10] Instrument Society of America and American National Standards Institute, *Electrical transducer nomenclature and terminology*. en. Research Triangle Park, N.C.: Instrument Society of America, 1982, OCLC: 11272242, ISBN: 978-0-87664-113-2.
- [11] T. Peffer, M. Pritoni, A. Meier, C. Aragon, and D. Perry, "How people use thermostats in homes: A review," *Building and Environment*, vol. 46, no. 12, pp. 2529–2541, 2011, Number: 12 ISBN: 0360-1323 Publisher: Elsevier.
- [12] U. Guth, W. Vonau, and J. Zosel, "Recent developments in electrochemical sensor application and technology—a review," en, *Measurement Science and Technology*, vol. 20, no. 4, p. 042002, Jan. 2009, Number: 4 Publisher: IOP Publishing, ISSN: 0957-0233. DOI: 10.1088/0957-0233/20/4/042002. [Online]. Available: <https://doi.org/10.1088/0957-0233/20/4/042002> (visited on 01/15/2021).
- [13] J. T. Maloy, *Factors affecting the shape of current-potential curves*. ACS Publications, 1983, ISBN: 0021-9584.
- [14] D. Harvey, *11.4: Voltammetric and Amperometric Methods*, en, Jun. 2020. [Online]. Available: [https://chem.libretexts.org/Courses/BethuneCookman.University/B-CU%3ACH-345_Quantitative_Analysis/Book%3A_Analytical_Chemistry_2.1_\(Harvey\)/11%3A_Electrochemical_Methods/11.04%3A_Voltammetric_and_Amperometric_Methods](https://chem.libretexts.org/Courses/BethuneCookman.University/B-CU%3ACH-345_Quantitative_Analysis/Book%3A_Analytical_Chemistry_2.1_(Harvey)/11%3A_Electrochemical_Methods/11.04%3A_Voltammetric_and_Amperometric_Methods) (visited on 01/15/2021).
- [15] D. Harvey, "Analytical Chemistry 2.0," 2018.

- [16] E. Paleček, “From polarography of DNA to microanalysis with nucleic acid-modified electrodes,” *Electroanalysis*, vol. 8, no. 1, pp. 7–14, 1996, Number: 1 ISBN: 1040-0397 Publisher: Wiley Online Library.
- [17] H. Y. Y. Nyein, W. Gao, Z. Shahpar, *et al.*, “A wearable electrochemical platform for non-invasive simultaneous monitoring of Ca²⁺ and pH,” *ACS nano*, vol. 10, no. 7, pp. 7216–7224, 2016, Number: 7 ISBN: 1936-0851 Publisher: ACS Publications.
- [18] D. W. Kimmel, G. LeBlanc, M. E. Meschievitz, and D. E. Cliffel, “Electrochemical sensors and biosensors,” *Analytical chemistry*, vol. 84, no. 2, pp. 685–707, 2012, Number: 2 ISBN: 0003-2700 Publisher: ACS Publications.
- [19] J. Wang, J. Wang, and K. Rogers, *Electrochemical sensors for environmental monitoring: a review of recent technology*. US Environmental Protection Agency, Office of Research and Development . . . , 1995.
- [20] J. W. Severinghaus and P. B. Astrup, “History of blood gas analysis. IV. Leland Clark’s oxygen electrode,” *Journal of clinical monitoring*, vol. 2, no. 2, pp. 125–139, 1986, Number: 2 ISBN: 0748-1977 Publisher: Springer.
- [21] M. I. Pividori, A. Merkoçi, and S. Alegret, “Dot-blot amperometric genosensor for detecting a novel determinant of b-lactamase resistance in *Staphylococcus aureus*,” *Analyst*, vol. 126, no. 9, pp. 1551–1557, 2001, Number: 9 Publisher: Royal Society of Chemistry.
- [22] E. Muthusankar, S. M. Wabaidur, Z. A. Alothman, M. R. Johan, V. K. Ponnusamy, and D. Ragupathy, “Fabrication of amperometric sensor for glucose detection based on phosphotungstic acid–assisted PDPA/ZnO nanohybrid composite,” *en, Ionics*, vol. 26, no. 12, pp. 6341–6349, Dec. 2020, Number: 12, ISSN: 1862-0760. DOI: 10.1007/s11581-020-03740-0. [Online]. Available: <https://doi.org/10.1007/s11581-020-03740-0> (visited on 01/15/2021).
- [23] S. Majumder, T. Mondal, and M. J. Deen, “Wearable sensors for remote health monitoring,” *Sensors*, vol. 17, no. 1, p. 130, 2017, Number: 1 Publisher: Multidisciplinary Digital Publishing Institute.
- [24] A. Campbell, *What are the spectrum band designators and bandwidths?* en, Publisher: Brian Dunbar, May 2015. [Online]. Available: http://www.nasa.gov/directorates/heo/scan/communications/outreach/funfacts/txt_band_designators.html (visited on 01/16/2021).

- [25] R. T. Hitchcock, *Radio-frequency and microwave radiation*. AIHA, 2004, ISBN: 1-931504-55-5.
- [26] M. D. Stoehr and I. PMTS, *Rf basics*, 2020.
- [27] J. C. Maxwell, "Viii. a dynamical theory of the electromagnetic field," *Philosophical transactions of the Royal Society of London*, no. 155, pp. 459–512, 1865.
- [28] R. Sorrentino and G. Bianchi, *Microwave and RF engineering*. John Wiley & Sons, 2010.
- [29] F. Caspers and P. Kowina, "Rf measurement concepts," 2014.
- [30] L. Y. Chen, B. C.-K. Tee, A. L. Chortos, *et al.*, "Continuous wireless pressure monitoring and mapping with ultra-small passive sensors for health monitoring and critical care," en, *Nature Communications*, vol. 5, no. 1, p. 5028, Oct. 2014, Number: 1 Publisher: Nature Publishing Group, ISSN: 2041-1723. DOI: 10.1038/ncomms6028. [Online]. Available: <https://www.nature.com/articles/ncomms6028> (visited on 01/15/2021).
- [31] Y.-G. Park, S. Lee, and J.-U. Park, "Recent Progress in Wireless Sensors for Wearable Electronics," en, *Sensors*, vol. 19, no. 20, p. 4353, Jan. 2019, Number: 20 Publisher: Multidisciplinary Digital Publishing Institute. DOI: 10.3390/s19204353. [Online]. Available: <https://www.mdpi.com/1424-8220/19/20/4353> (visited on 01/15/2021).
- [32] M. S. Mannoor, H. Tao, J. D. Clayton, *et al.*, "Graphene-based wireless bacteria detection on tooth enamel," en, *Nature Communications*, vol. 3, no. 1, p. 763, Mar. 2012, Number: 1 Publisher: Nature Publishing Group, ISSN: 2041-1723. DOI: 10.1038/ncomms1767. [Online]. Available: <https://www.nature.com/articles/ncomms1767> (visited on 01/15/2021).
- [33] P. Tseng, B. Napier, L. Garbarini, D. L. Kaplan, and F. G. Omenetto, "Functional, RF-Trilayer Sensors for Tooth-Mounted, Wireless Monitoring of the Oral Cavity and Food Consumption," eng, *Advanced Materials (Deerfield Beach, Fla.)*, vol. 30, no. 18, e1703257, May 2018, Number: 18, ISSN: 1521-4095. DOI: 10.1002/adma.201703257.
- [34] N. Kozma, H. Speletz, U. Reiter, G. Lanzer, and T. Wagner, "Impact of 13.56-MHz radiofrequency identification systems on the quality of stored red blood cells," *Transfusion*, vol. 51, no. 11, pp. 2384–2390, 2011, Number: 11 ISBN: 0041-1132 Publisher: Wiley Online Library.
- [35] Z. Geng, X. Zhang, Z. Fan, X. Lv, and H. Chen, "A Route to Terahertz Metamaterial Biosensor Integrated with Microfluidics for Liver Cancer Biomarker Testing in Early Stage," en, *Scientific Reports*, vol. 7, no. 1, p. 16378, Nov. 2017, Number: 1 Publisher:

- Nature Publishing Group, ISSN: 2045-2322. DOI: 10.1038/s41598-017-16762-y. [Online]. Available: <https://www.nature.com/articles/s41598-017-16762-y> (visited on 07/06/2020).
- [36] K. H. Eom, M. C. Kim, S. Lee, and C. W. Lee, "The vegetable freshness monitoring system using RFID with oxygen and carbon dioxide sensor," *International Journal of Distributed Sensor Networks*, vol. 8, no. 6, p. 472 986, 2012, Number: 6 ISBN: 1550-1477 Publisher: SAGE Publications Sage UK: London, England.
- [37] E. Smits, J. Schram, M. Nagelkerke, *et al.*, "4.5. 2 Development of printed RFID sensor tags for smart food packaging," *Tagungsband*, pp. 403–406, 2012.
- [38] L. Sen, K. H. Hyun, J. W. Kim, J. W. Shin, and K. H. Eom, "The design of smart RFID system with gas sensor for meat freshness monitoring," *Advanced Science and Technology Letters*, vol. 41, pp. 17–20, 2013.
- [39] K.-H. Eom, K.-H. Hyun, S. Lin, and J.-W. Kim, "The meat freshness monitoring system using the smart RFID tag," *International Journal of Distributed Sensor Networks*, vol. 10, no. 7, p. 591 812, 2014, Number: 7 ISBN: 1550-1477 Publisher: SAGE Publications Sage UK: London, England.
- [40] R. A. Potyrailo, N. Nagraj, Z. Tang, F. J. Mondello, C. Surman, and W. Morris, "Battery-free radio frequency identification (RFID) sensors for food quality and safety," *Journal of agricultural and food chemistry*, vol. 60, no. 35, pp. 8535–8543, 2012, Number: 35 ISBN: 0021-8561 Publisher: ACS Publications.
- [41] W.-D. Huang, S. Deb, Y.-S. Seo, S. Rao, M. Chiao, and J. C. Chiao, "A passive radio-frequency pH-sensing tag for wireless food-quality monitoring," *IEEE Sensors Journal*, vol. 12, no. 3, pp. 487–495, 2011, Number: 3 ISBN: 1530-437X Publisher: IEEE.
- [42] H. Cheng, G. Shao, S. Ebadi, *et al.*, "Evanescent-mode-resonator-based and antenna-integrated wireless passive pressure sensors for harsh-environment applications," *Sensors and Actuators A: Physical*, vol. 220, pp. 22–33, 2014, ISBN: 0924-4247 Publisher: Elsevier.
- [43] C. Li, Q. Tan, P. Jia, *et al.*, "Review of research status and development trends of wireless passive LC resonant sensors for harsh environments," *Sensors*, vol. 15, no. 6, pp. 13 097–13 109, 2015, Number: 6 Publisher: Multidisciplinary Digital Publishing Institute.

- [44] Q. Tan, T. Luo, T. Wei, J. Liu, L. Lin, and J. Xiong, "A wireless passive pressure and temperature sensor via a dual LC resonant circuit in harsh environments," *Journal of Microelectromechanical Systems*, vol. 26, no. 2, pp. 351–356, 2017, Number: 2 ISBN: 1057-7157 Publisher: IEEE.
- [45] Y. Wang, Y. Jia, Q. Chen, and Y. Wang, "A passive wireless temperature sensor for harsh environment applications," *Sensors*, vol. 8, no. 12, pp. 7982–7995, 2008, Number: 12 Publisher: Molecular Diversity Preservation International.
- [46] J. Jun, J. Oh, D. H. Shin, *et al.*, "Wireless, Room Temperature Volatile Organic Compound Sensor Based on Polypyrrole Nanoparticle Immobilized Ultrahigh Frequency Radio Frequency Identification Tag," *ACS Applied Materials & Interfaces*, vol. 8, no. 48, pp. 33 139–33 147, Dec. 2016, Number: 48 Publisher: American Chemical Society, ISSN: 1944-8244. DOI: 10.1021/acsami.6b08344. [Online]. Available: <https://doi.org/10.1021/acsami.6b08344> (visited on 01/15/2021).
- [47] V. G. Veselago, "Electrodynamics of substances with simultaneously negative and," *Usp. Fiz. Nauk*, vol. 92, p. 517, 1967.
- [48] D. R. Smith, W. J. Padilla, D. C. Vier, S. C. Nemat-Nasser, and S. Schultz, "Composite medium with simultaneously negative permeability and permittivity," *Physical review letters*, vol. 84, no. 18, p. 4184, 2000, Number: 18 Publisher: APS.
- [49] J. B. Pendry, A. J. Holden, D. J. Robbins, and W. J. Stewart, "Magnetism from conductors and enhanced nonlinear phenomena," *IEEE transactions on microwave theory and techniques*, vol. 47, no. 11, pp. 2075–2084, 1999, Number: 11 ISBN: 0018-9480 Publisher: IEEE.
- [50] C. M. Soukoulis, S. Linden, and M. Wegener, "Negative refractive index at optical wavelengths," *Science*, vol. 315, no. 5808, pp. 47–49, 2007, Number: 5808 ISBN: 0036-8075 Publisher: American Association for the Advancement of Science.
- [51] J. T. Hong, D. J. Park, J. H. Yim, *et al.*, "Dielectric constant engineering of single-walled carbon nanotube films for metamaterials and plasmonic devices," *The Journal of Physical Chemistry Letters*, vol. 4, no. 22, pp. 3950–3957, 2013, Number: 22 ISBN: 1948-7185 Publisher: ACS Publications.

- [52] Y.-T. Chang, Y.-C. Lai, C.-T. Li, C.-K. Chen, and T.-J. Yen, "A multi-functional plasmonic biosensor," *Optics express*, vol. 18, no. 9, pp. 9561–9569, 2010, Number: 9 ISBN: 1094-4087 Publisher: Optical Society of America.
- [53] H. Torun, F. Cagri Top, G. Dundar, and A. D. Yalcinkaya, "An antenna-coupled splitting resonator for biosensing," *Journal of Applied Physics*, vol. 116, no. 12, p. 124 701, Sep. 2014, Publisher: American Institute of Physics, ISSN: 0021-8979. DOI: 10.1063/1.4896261. [Online]. Available: <https://aip.scitation.org/doi/10.1063/1.4896261> (visited on 01/15/2021).
- [54] C. Debus and P. H. Bolivar, "Frequency selective surfaces for high sensitivity terahertz sensing," *Applied Physics Letters*, vol. 91, no. 18, p. 184 102, 2007, Number: 18 ISBN: 0003-6951 Publisher: American Institute of Physics.
- [55] R. Zhang, Q. Chen, K. Liu, *et al.*, "Terahertz Microfluidic Metamaterial Biosensor for Sensitive Detection of Small-Volume Liquid Samples," *IEEE Transactions on Terahertz Science and Technology*, vol. 9, no. 2, pp. 209–214, Mar. 2019, Number: 2 Conference Name: IEEE Transactions on Terahertz Science and Technology, ISSN: 2156-3446. DOI: 10.1109/TTHZ.2019.2898390.
- [56] V. J. Gokhale, O. A. Shenderova, G. E. McGuire, and M. Rais-Zadeh, "Infrared absorption properties of carbon nanotube/nanodiamond based thin film coatings," *Journal of Microelectromechanical Systems*, vol. 23, no. 1, pp. 191–197, 2013, Number: 1 ISBN: 1057-7157 Publisher: IEEE.
- [57] W. Li and J. Valentine, "Metamaterial perfect absorber based hot electron photodetection," *Nano letters*, vol. 14, no. 6, pp. 3510–3514, 2014, Number: 6 ISBN: 1530-6984 Publisher: ACS Publications.
- [58] M. Abdolrazzaghi, S. Khan, and M. Daneshmand, "A dual-mode split-ring resonator to eliminate relative humidity impact," *IEEE Microwave and Wireless Components Letters*, vol. 28, no. 10, pp. 939–941, 2018, Number: 10 ISBN: 1531-1309 Publisher: IEEE.
- [59] N. Fang and X. Zhang, "Imaging properties of a metamaterial superlens," in *Proceedings of the 2nd IEEE Conference on Nanotechnology*, IEEE, 2002, pp. 225–228, ISBN: 0-7803-7538-6.
- [60] S. Haxha, F. AbdelMalek, F. Ouerghi, M. D. B. Charlton, A. Aggoun, and X. Fang, "Metamaterial superlenses operating at visible wavelength for imaging applications," *Scientific*

- reports*, vol. 8, no. 1, pp. 1–15, 2018, Number: 1 ISBN: 2045-2322 Publisher: Nature Publishing Group.
- [61] Z. J. Wong, Y. Wang, K. O'Brien, *et al.*, “Optical and acoustic metamaterials: Superlens, negative refractive index and invisibility cloak,” *Journal of Optics*, vol. 19, no. 8, p. 084 007, 2017, Number: 8 ISBN: 2040-8986 Publisher: IOP Publishing.
- [62] A. Alu and N. Engheta, “Plasmonic and metamaterial cloaking: Physical mechanisms and potentials,” *Journal of Optics A: Pure and Applied Optics*, vol. 10, no. 9, p. 093 002, 2008, Number: 9 ISBN: 1464-4258 Publisher: IOP Publishing.
- [63] W. Cai, U. K. Chettiar, A. V. Kildishev, and V. M. Shalaev, “Optical cloaking with metamaterials,” *Nature photonics*, vol. 1, no. 4, pp. 224–227, 2007, Number: 4 ISBN: 1749-4893 Publisher: Nature Publishing Group.
- [64] M. Manjappa, P. Pitchappa, N. Wang, C. Lee, and R. Singh, “Active control of resonant cloaking in a terahertz MEMS metamaterial,” *Advanced Optical Materials*, vol. 6, no. 16, p. 1 800 141, 2018, Number: 16 ISBN: 2195-1071 Publisher: Wiley Online Library.
- [65] S. Zahertar, A. D. Yalcinkaya, and H. Torun, “Rectangular split-ring resonators with single-split and two-splits under different excitations at microwave frequencies,” *AIP Advances*, vol. 5, no. 11, p. 117 220, Nov. 2015, Publisher: American Institute of Physics. DOI: 10.1063/1.4935910. [Online]. Available: <https://aip.scitation.org/doi/10.1063/1.4935910> (visited on 01/15/2021).
- [66] K. Jaruwongrungrsee, U. Waiwijit, W. Withayachumnankul, *et al.*, “Microfluidic-based split-ring-resonator sensor for real-time and label-free biosensing,” *Procedia engineering*, vol. 120, pp. 163–166, 2015, ISBN: 1877-7058 Publisher: Elsevier.
- [67] G. Ekinici, A. D. Yalcinkaya, G. Dundar, and H. Torun, “Split-ring resonator-based strain sensor on flexible substrates for glaucoma detection,” in *Journal of Physics: Conference Series*, Issue: 1, vol. 757, IOP Publishing, 2016, p. 012 019, ISBN: 1742-6588.
- [68] H.-J. Lee and J.-G. Yook, “Biosensing using split-ring resonators at microwave regime,” *Applied Physics Letters*, vol. 92, no. 25, p. 254 103, 2008, Number: 25 ISBN: 0003-6951 Publisher: American Institute of Physics.
- [69] H. O. Moser, B. D. F. Casse, O. Wilhelmi, and B. T. Saw, “Terahertz Response of a Microfabricated Rod-Split-Ring-Resonator Electromagnetic Metamaterial,” *Physical Review Letters*, vol. 94, no. 6, p. 063 901, Feb. 2005, Number: 6 Publisher: American Physical So-

- ciety. DOI: 10.1103/PhysRevLett.94.063901. [Online]. Available: <https://link.aps.org/doi/10.1103/PhysRevLett.94.063901> (visited on 07/09/2020).
- [70] H.-J. Lee, J.-H. Lee, H.-S. Moon, *et al.*, “A planar split-ring resonator-based microwave biosensor for label-free detection of biomolecules,” en, *Sensors and Actuators B: Chemical*, vol. 169, pp. 26–31, Jul. 2012, ISSN: 0925-4005. DOI: 10.1016/j.snb.2012.01.044. [Online]. Available: <http://www.sciencedirect.com/science/article/pii/S0925400512000676> (visited on 01/15/2021).
- [71] M. H. Zarifi, M. Rahimi, M. Daneshmand, and T. Thundat, “Microwave ring resonator-based non-contact interface sensor for oil sands applications,” en, *Sensors and Actuators B: Chemical*, vol. 224, pp. 632–639, Mar. 2016, ISSN: 0925-4005. DOI: 10.1016/j.snb.2015.10.061. [Online]. Available: <http://www.sciencedirect.com/science/article/pii/S092540051530527X> (visited on 01/15/2021).
- [72] H. Kairm, D. Delfin, M. A. I. Shuvo, *et al.*, “Concept and model of a metamaterial-based passive wireless temperature sensor for harsh environment applications,” *IEEE Sensors Journal*, vol. 15, no. 3, pp. 1445–1452, 2014, Number: 3 ISBN: 1530-437X Publisher: IEEE.
- [73] S. P. Chakyar, S. K. Simon, C. Bindu, J. Andrews, and V. P. Joseph, “Complex permittivity measurement using metamaterial split ring resonators,” *Journal of Applied Physics*, vol. 121, no. 5, p. 054 101, 2017, Number: 5 ISBN: 0021-8979 Publisher: AIP Publishing LLC.
- [74] R. A. Alahnomi, Z. Zakaria, E. Ruslan, A. A. Mohd Bahar, and S. R. Ab Rashid, “High sensitive microwave sensor based on symmetrical split ring resonator for material characterization,” *Microwave and Optical Technology Letters*, vol. 58, no. 9, pp. 2106–2110, 2016, Number: 9 ISBN: 0895-2477 Publisher: Wiley Online Library.
- [75] H. Tao, M. A. Brenckle, M. Yang, *et al.*, “Silk-based conformal, adhesive, edible food sensors,” *Advanced Materials*, vol. 24, no. 8, pp. 1067–1072, 2012, Number: 8 ISBN: 0935-9648 Publisher: Wiley Online Library.
- [76] J. Naqui, M. Durán-Sindreu, and F. Martín, “Alignment and position sensors based on split ring resonators,” *Sensors*, vol. 12, no. 9, pp. 11 790–11 797, 2012, Number: 9 Publisher: Molecular Diversity Preservation International.

- [77] A. Salim, S. Ghosh, and S. Lim, “Low-Cost and Lightweight 3D-Printed Split-Ring Resonator for Chemical Sensing Applications,” en, *Sensors*, vol. 18, no. 9, p. 3049, Sep. 2018, Number: 9 Publisher: Multidisciplinary Digital Publishing Institute. DOI: 10.3390/s18093049. [Online]. Available: <https://www.mdpi.com/1424-8220/18/9/3049> (visited on 01/15/2021).
- [78] A. Salim and S. Lim, “Complementary Split-Ring Resonator-Loaded Microfluidic Ethanol Chemical Sensor,” en, *Sensors*, vol. 16, no. 11, p. 1802, Nov. 2016, Number: 11 Publisher: Multidisciplinary Digital Publishing Institute. DOI: 10.3390/s16111802. [Online]. Available: <https://www.mdpi.com/1424-8220/16/11/1802> (visited on 01/15/2021).
- [79] W. Connacher, N. Zhang, A. Huang, *et al.*, “Micro/nano acoustofluidics: Materials, phenomena, design, devices, and applications,” en, *Lab on a Chip*, vol. 18, no. 14, pp. 1952–1996, Jul. 2018, Number: 14 Publisher: The Royal Society of Chemistry, ISSN: 1473-0189. DOI: 10.1039/C8LC00112J. [Online]. Available: <https://pubs.rsc.org/en/content/articlelanding/2018/lc/c8lc00112j> (visited on 01/18/2021).
- [80] C.-Y. Lee, W.-T. Wang, C.-C. Liu, and L.-M. Fu, “Passive mixers in microfluidic systems: A review,” *Chemical Engineering Journal*, vol. 288, pp. 146–160, 2016, ISBN: 1385-8947 Publisher: Elsevier.
- [81] E. K. Sackmann, A. L. Fulton, and D. J. Beebe, “The present and future role of microfluidics in biomedical research,” *Nature*, vol. 507, no. 7491, pp. 181–189, 2014, Number: 7491 ISBN: 1476-4687 Publisher: Nature Publishing Group.
- [82] E. F. F. Chladni, “Discoveries on the theory of sound,” *Breitkopf und Hartel: Leipzig*, 1787.
- [83] M. Faraday, “On the forms and states assumed by fluids in contact with vibrating elastic surfaces,” *Philos. Trans. R. Soc. London*, vol. 121, pp. 39–346, 1831.
- [84] A. Kundt, “Ueber eine neue Art akustischer Staubfiguren und über die Anwendung derselben zur Bestimmung der Schallgeschwindigkeit in festen Körpern und Gasen,” *Annalen der Physik*, vol. 203, no. 4, pp. 497–523, 1866, Number: 4 ISBN: 0003-3804 Publisher: Wiley Online Library.
- [85] L. Y. Yeo and J. R. Friend, “Surface acoustic wave microfluidics,” *Annual review of fluid mechanics*, vol. 46, pp. 379–406, 2014.
- [86] P. Zhang, H. Bachman, A. Ozcelik, and T. J. Huang, “Acoustic microfluidics,” *Annual Review of Analytical Chemistry*, vol. 13, pp. 17–43, 2020.

- [87] M. J. Vellekoop, “Acoustic wave sensors and their technology,” *Ultrasonics*, vol. 36, no. 1-5, pp. 7–14, 1998.
- [88] N. Shehata, A. H. Hassanin, E. Elnabawy, R. Nair, S. A. Bhat, and I. Kandas, “Acoustic energy harvesting and sensing via electrospun pvdf nanofiber membrane,” *Sensors*, vol. 20, no. 11, p. 3111, 2020.
- [89] M. Baudoin and J.-L. Thomas, “Acoustic tweezers for particle and fluid micromanipulation,” *Annual Review of Fluid Mechanics*, vol. 52, pp. 205–234, 2020.
- [90] Y. Q. Fu, J. K. Luo, N. T. Nguyen, *et al.*, “Advances in piezoelectric thin films for acoustic biosensors, acoustofluidics and lab-on-chip applications,” en, *Progress in Materials Science*, vol. 89, pp. 31–91, Aug. 2017, ISSN: 0079-6425. DOI: 10.1016/j.pmatsci.2017.04.006. [Online]. Available: <http://www.sciencedirect.com/science/article/pii/S0079642517300403> (visited on 01/15/2021).
- [91] S. R. Moheimani and A. J. Fleming, *Piezoelectric transducers for vibration control and damping*. Springer Science & Business Media, 2006, ISBN: 1-84628-332-9.
- [92] S. Katzir, “Who knew piezoelectricity? Rutherford and Langevin on submarine detection and the invention of sonar,” *Notes and Records of the Royal Society*, vol. 66, no. 2, pp. 141–157, Jun. 2012, Number: 2 Publisher: Royal Society. DOI: 10.1098/rsnr.2011.0049. [Online]. Available: <https://royalsocietypublishing.org/doi/10.1098/rsnr.2011.0049> (visited on 01/15/2021).
- [93] A. Manbachi and R. S. C. Cobbold, “Development and Application of Piezoelectric Materials for Ultrasound Generation and Detection,” en, *Ultrasound*, vol. 19, no. 4, pp. 187–196, Nov. 2011, Number: 4 Publisher: SAGE Publications, ISSN: 1742-271X. DOI: 10.1258/ult.2011.011027. [Online]. Available: <https://doi.org/10.1258/ult.2011.011027> (visited on 01/15/2021).
- [94] J. Fraden, *Handbook of Modern Sensor*. Springer, 2013.
- [95] K. M. Ok, E. O. Chi, and P. S. Halasyamani, “Bulk characterization methods for non-centrosymmetric materials: Second-harmonic generation, piezoelectricity, pyroelectricity, and ferroelectricity,” en, *Chemical Society Reviews*, vol. 35, no. 8, pp. 710–717, Jul. 2006, Number: 8 Publisher: The Royal Society of Chemistry, ISSN: 1460-4744. DOI: 10.1039/B511119F. [Online]. Available: <https://pubs.rsc.org/en/content/articlelanding/2006/cs/b511119f> (visited on 01/15/2021).

- [96] L. B. Kong, H. Huang, and S. Li, “Fundamentals of Ferroelectric Materials,” en, in *Ferroelectric Materials for Energy Applications*, Section: 1 eprint: <https://onlinelibrary.wiley.com/doi/pdf/10.1002/9783527807505.ch1>, John Wiley & Sons, Ltd, 2018, pp. 1–31, ISBN: 978-3-527-80750-5. DOI: 10.1002/9783527807505.ch1. [Online]. Available: <https://www.onlinelibrary.wiley.com/doi/abs/10.1002/9783527807505.ch1> (visited on 01/15/2021).
- [97] W. P. Mason, “Piezoelectricity, its history and applications,” *The Journal of the Acoustical Society of America*, vol. 70, no. 6, pp. 1561–1566, Dec. 1981, Number: 6 Publisher: Acoustical Society of America, ISSN: 0001-4966. DOI: 10.1121/1.387221. [Online]. Available: <https://asa.scitation.org/doi/10.1121/1.387221> (visited on 01/15/2021).
- [98] A. Lüker, “A short history of ferroelectricity,” *by talari.com*. [Online, p. 9, 2011.
- [99] A. L. Kholkin, N. A. Pertsev, and A. V. Goltsev, “Piezoelectricity and crystal symmetry,” in *Piezoelectric and Acoustic Materials for Transducer Applications*, Springer, 2008, pp. 17–38.
- [100] W. Heywang, K. Lubitz, and W. Wersing, Eds., *Piezoelectricity: Evolution and Future of a Technology* (Springer Series in Materials Science), en. Berlin Heidelberg: Springer-Verlag, 2008, ISBN: 978-3-540-68680-4. DOI: 10.1007/978-3-540-68683-5. [Online]. Available: <https://www.springer.com/gp/book/9783540686804> (visited on 01/15/2021).
- [101] A. Vazquez Carazo, “Piezoelectric Transformers: An Historical Review,” en, *Actuators*, vol. 5, no. 2, p. 12, Jun. 2016, Number: 2 Publisher: Multidisciplinary Digital Publishing Institute. DOI: 10.3390/act5020012. [Online]. Available: <https://www.mdpi.com/2076-0825/5/2/12> (visited on 01/15/2021).
- [102] B. Jaffe, *Piezoelectric ceramics*. Elsevier, 2012, vol. 3, ISBN: 0-323-15568-5.
- [103] W. P. Mason and H. Baerwald, “Piezoelectric Crystals and Their Applications to Ultrasonics,” en, *Physics Today*, vol. 4, no. 5, p. 23, Jan. 2009, Number: 5 Publisher: American Institute of PhysicsAIP, ISSN: 0031-9228. DOI: 10.1063/1.3067231. [Online]. Available: <https://physicstoday.scitation.org/doi/abs/10.1063/1.3067231> (visited on 01/15/2021).
- [104] H. D. Megaw, “Ferroelectricity in crystals,” 1957, Publisher: Methuen.
- [105] J. Kim, A. S. Campbell, B. E.-F. de Ávila, and J. Wang, “Wearable biosensors for health-care monitoring,” en, *Nature Biotechnology*, vol. 37, no. 4, pp. 389–406, Apr. 2019, Number: 4 Publisher: Nature Publishing Group, ISSN: 1546-1696. DOI: 10.1038/s41587-019-

- 0045-y. [Online]. Available: <https://www.nature.com/articles/s41587-019-0045-y> (visited on 01/15/2021).
- [106] B. Saravanakumar, S. Soyoon, and S.-J. Kim, "Self-Powered pH Sensor Based on a Flexible Organic–Inorganic Hybrid Composite Nanogenerator," *ACS Applied Materials & Interfaces*, vol. 6, no. 16, pp. 13 716–13 723, Aug. 2014, Number: 16 Publisher: American Chemical Society, ISSN: 1944-8244. DOI: 10.1021/am5031648. [Online]. Available: <https://doi.org/10.1021/am5031648> (visited on 01/15/2021).
- [107] S.-T. Han, H. Peng, Q. Sun, *et al.*, "An Overview of the Development of Flexible Sensors," *en, Advanced Materials*, vol. 29, no. 33, p. 1 700 375, 2017, Number: 33 _eprint: <https://onlinelibrary.wiley.com/doi/pdf/10.1002/adma.201700375>, ISSN: 1521-4095. DOI: <https://doi.org/10.1002/adma.201700375>. [Online]. Available: <https://onlinelibrary.wiley.com/doi/abs/10.1002/adma.201700375> (visited on 01/15/2021).
- [108] S. Kärki and J. Lekkala, "Film-type transducer materials PVDF and EMFi in the measurement of heart and respiration rates," *eng, Annual International Conference of the IEEE Engineering in Medicine and Biology Society. IEEE Engineering in Medicine and Biology Society. Annual International Conference*, vol. 2008, pp. 530–533, 2008, ISSN: 2375-7477. DOI: 10.1109/IEMBS.2008.4649207.
- [109] T. Yilmaz, R. Foster, and Y. Hao, "Detecting vital signs with wearable wireless sensors," *eng, Sensors (Basel, Switzerland)*, vol. 10, no. 12, pp. 10 837–10 862, 2010, Number: 12, ISSN: 1424-8220. DOI: 10.3390/s101210837.
- [110] J.-H. Yang, H.-S. Cho, S.-H. Park, S.-H. Song, K.-S. Yun, and J. H. Lee, "Effect of garment design on piezoelectricity harvesting from joint movement," *en, Smart Materials and Structures*, vol. 25, no. 3, p. 035 012, Feb. 2016, Number: 3 Publisher: IOP Publishing, ISSN: 0964-1726. DOI: 10.1088/0964-1726/25/3/035012. [Online]. Available: <https://doi.org/10.1088/0964-1726/25/3/035012> (visited on 01/15/2021).
- [111] X. Pu, L. Li, M. Liu, *et al.*, "Wearable Self-Charging Power Textile Based on Flexible Yarn Supercapacitors and Fabric Nanogenerators," *Advanced Materials*, vol. 28, no. 1, pp. 98–105, 2016, Number: 1 _eprint: <https://onlinelibrary.wiley.com/doi/pdf/10.1002/adma.201504403>, ISSN: 1521-4095. DOI: <https://doi.org/10.1002/adma.201504403>. [Online]. Available: <https://onlinelibrary.wiley.com/doi/abs/10.1002/adma.201504403> (visited on 01/15/2021).

- [112] G. Sauerbrey, "Use of quartz vibrator for weighting thin films on a microbalance," *Zeitschrift für Physik*, vol. 155, pp. 206–212, 1959.
- [113] A. Alassi, M. Benammar, and D. Brett, "Quartz crystal microbalance electronic interfacing systems: A review," *Sensors*, vol. 17, no. 12, p. 2799, 2017, Number: 12 Publisher: Multidisciplinary Digital Publishing Institute.
- [114] Y. Zhang, J. Luo, A. J. Flewitt, Z. Cai, and X. Zhao, "Film bulk acoustic resonators (FBARs) as biosensors: A review," en, *Biosensors and Bioelectronics*, vol. 116, pp. 1–15, Sep. 2018, ISSN: 0956-5663. DOI: 10.1016/j.bios.2018.05.028. [Online]. Available: <http://www.sciencedirect.com/science/article/pii/S0956566318303750> (visited on 01/15/2021).
- [115] L. Rayleigh, "On waves propagated along the plane surface of an elastic solid," *Proceedings of the London mathematical Society*, vol. 1, no. 1, pp. 4–11, 1885, Number: 1 ISBN: 0024-6115 Publisher: Wiley Online Library.
- [116] C. Campbell, *Surface acoustic wave devices and their signal processing applications*. Elsevier, 2012, ISBN: 0-323-14866-2.
- [117] X. Ding, P. Li, S.-C. S. Lin, *et al.*, "Surface acoustic wave microfluidics," en, *Lab on a Chip*, vol. 13, no. 18, pp. 3626–3649, Aug. 2013, Publisher: The Royal Society of Chemistry, ISSN: 1473-0189. DOI: 10.1039/C3LC50361E. [Online]. Available: <https://pubs.rsc.org/en/content/articlelanding/2013/lc/c3lc50361e> (visited on 01/15/2021).
- [118] R. N. Thurston, A. D. Pierce, and E. P. Papadakis, *Reference for Modern Instrumentation, Techniques, and Technology: Ultrasonic Instruments and Devices I: Ultrasonic Instruments and Devices I*. Academic Press, 1998, ISBN: 0-08-053890-8.
- [119] A. Wixforth, C. Strobl, C. Gauer, A. Toegl, J. Scriba, and Z. v. Guttenberg, "Acoustic manipulation of small droplets," *Analytical and bioanalytical chemistry*, vol. 379, no. 7-8, pp. 982–991, 2004, Number: 7-8 ISBN: 1618-2642 Publisher: Springer.
- [120] R. Shilton, M. K. Tan, L. Y. Yeo, and J. R. Friend, "Particle concentration and mixing in microdrops driven by focused surface acoustic waves," *Journal of Applied Physics*, vol. 104, no. 1, p. 014910, Jul. 2008, Publisher: American Institute of Physics, ISSN: 0021-8979. DOI: 10.1063/1.2951467. [Online]. Available: <https://aip.scitation.org/doi/10.1063/1.2951467> (visited on 01/15/2021).

- [121] A. Wixforth, “Acoustically driven programmable microfluidics for biological and chemical applications,” *JALA: Journal of the Association for Laboratory Automation*, vol. 11, no. 6, pp. 399–405, 2006, Number: 6 ISBN: 1535-5535 Publisher: SAGE Publications Sage CA: Los Angeles, CA.
- [122] K. Chono, N. Shimizu, Y. Matsui, J. Kondoh, and S. Shiokawa, “Development of novel atomization system based on SAW streaming,” *Japanese journal of applied physics*, vol. 43, no. 5S, p. 2987, 2004, Number: 5S ISBN: 1347-4065 Publisher: IOP Publishing.
- [123] A. Toegl, R. Kirchner, C. Gauer, and A. Wixforth, “Enhancing results of microarray hybridizations through microagitation,” *Journal of biomolecular techniques: JBT*, vol. 14, no. 3, p. 197, 2003, Number: 3 Publisher: The Association of Biomolecular Resource Facilities.
- [124] M. I. Newton, M. K. Banerjee, T. K. H. Starke, S. M. Rowan, and G. McHale, “Surface acoustic wave–liquid drop interactions,” *Sensors and Actuators A: Physical*, vol. 76, no. 1-3, pp. 89–92, 1999, Number: 1-3 ISBN: 0924-4247 Publisher: Elsevier.
- [125] K. P. Kulkarni, S. H. Ramarathinam, J. Friend, L. Yeo, A. W. Purcell, and P. Perlmutter, “Rapid microscale in-gel processing and digestion of proteins using surface acoustic waves,” *Lab on a Chip*, vol. 10, no. 12, pp. 1518–1520, 2010, Number: 12 Publisher: Royal Society of Chemistry.
- [126] T. Frommelt, M. Kostur, M. Wenzel-Schäfer, P. Talkner, P. Hänggi, and A. Wixforth, “Microfluidic mixing via acoustically driven chaotic advection,” *Physical review letters*, vol. 100, no. 3, p. 034 502, 2008, Number: 3 Publisher: APS.
- [127] Z. Guttenberg, H. Müller, H. Habermüller, *et al.*, “Planar chip device for PCR and hybridization with surface acoustic wave pump,” *Lab on a Chip*, vol. 5, no. 3, pp. 308–317, 2005, Number: 3 Publisher: Royal Society of Chemistry.
- [128] A. Wixforth, “Acoustically driven planar microfluidics,” *Superlattices and Microstructures*, vol. 33, no. 5-6, pp. 389–396, 2003, Number: 5-6 ISBN: 0749-6036 Publisher: Elsevier.
- [129] A. Renaudin, P. Tabourier, J.-C. Camart, and C. Druon, *Surface acoustic wave two-dimensional transport and location of microdroplets using echo signal*. American Institute of Physics, 2006, ISBN: 0021-8979.

- [130] M. Baudoin, P. Brunet, O. Bou Matar, and E. Herth, “Low power sessile droplets actuation via modulated surface acoustic waves,” *Applied Physics Letters*, vol. 100, no. 15, p. 154 102, 2012, Number: 15 ISBN: 0003-6951 Publisher: American Institute of Physics.
- [131] Y. Ai and B. L. Marrone, “Droplet translocation by focused surface acoustic waves,” *Microfluidics and nanofluidics*, vol. 13, no. 5, pp. 715–722, 2012, Number: 5 ISBN: 1613-4982 Publisher: Springer.
- [132] S. Collignon, J. Friend, and L. Yeo, “Planar microfluidic drop splitting and merging,” *Lab on a Chip*, vol. 15, no. 8, pp. 1942–1951, 2015, Number: 8 Publisher: Royal Society of Chemistry.
- [133] Y. Sriphutkiat, S. Kasetsirikul, D. Ketpun, and Y. Zhou, “Cell alignment and accumulation using acoustic nozzle for bioprinting,” *Scientific reports*, vol. 9, no. 1, pp. 1–12, 2019, Number: 1 ISBN: 2045-2322 Publisher: Nature Publishing Group UK.
- [134] S. Shiokawa, Y. Matsui, and T. Ueda, “Study on SAW streaming and its application to fluid devices,” *Japanese journal of applied physics*, vol. 29, no. S1, p. 137, 1990, Number: S1 ISBN: 1347-4065 Publisher: IOP Publishing.
- [135] J. Benne, S. Alzuaga, S. Ballandras, F. Cherioux, F. Bastien, and J.-F. Manceau, “Droplet ejector using surface acoustic waves,” in *IEEE Ultrasonics Symposium, 2005.*, vol. 2, IEEE, 2005, pp. 823–826, ISBN: 0-7803-9382-1.
- [136] H.-F. Pang, Y. Q. Fu, L. Garcia-Gancedo, *et al.*, “Enhancement of microfluidic efficiency with nanocrystalline diamond interlayer in the ZnO-based surface acoustic wave device,” *Microfluidics and nanofluidics*, vol. 15, no. 3, pp. 377–386, 2013, Number: 3 ISBN: 1613-4982 Publisher: Springer.
- [137] M. Darmawan and D. Byun, “Focused surface acoustic wave induced jet formation on superhydrophobic surfaces,” *Microfluidics and Nanofluidics*, vol. 18, no. 5-6, pp. 1107–1114, 2015, Number: 5-6 ISBN: 1613-4982 Publisher: Springer.
- [138] W. P. Jakubik, “Surface acoustic wave-based gas sensors,” en, *Thin Solid Films*, Special Section: Proceedings of 7th International Workshop on Semiconductor Gas Sensors, vol. 520, no. 3, pp. 986–993, Nov. 2011, Number: 3, ISSN: 0040-6090. DOI: 10.1016/j.tsf.2011.04.174. [Online]. Available: <http://www.sciencedirect.com/science/article/pii/S0040609011010157> (visited on 01/15/2021).

- [139] L. A. Kuznetsova and W. T. Coakley, “Applications of ultrasound streaming and radiation force in biosensors,” eng, *Biosensors & Bioelectronics*, vol. 22, no. 8, pp. 1567–1577, Mar. 2007, Number: 8, ISSN: 0956-5663. DOI: 10.1016/j.bios.2006.08.023.
- [140] G. Panneerselvam, V. Thirumal, and H. M. Pandya, “Review of surface acoustic wave sensors for the detection and identification of toxic environmental gases/vapours,” *Archives of Acoustics*, vol. 43, 2018.
- [141] F. Lurz, T. Ostertag, B. Scheiner, R. Weigel, and A. Koelpin, “Reader Architectures for Wireless Surface Acoustic Wave Sensors,” en, *Sensors*, vol. 18, no. 6, p. 1734, Jun. 2018, Number: 6 Publisher: Multidisciplinary Digital Publishing Institute. DOI: 10.3390/s18061734. [Online]. Available: <https://www.mdpi.com/1424-8220/18/6/1734> (visited on 01/15/2021).
- [142] M. Hribšek, D. Tošić, and M. Radosavljević, “Surface Acoustic Wave Sensors in Mechanical Engineering,” *FME Transactions*, vol. 38, pp. 11–18, Jan. 2010.
- [143] W. Buff, M. Rusko, T. Vandahl, M. Goroll, and F. Moller, “A differential measurement SAW device for passive remote sensing,” in *1996 IEEE Ultrasonics Symposium. Proceedings*, ISSN: 1051-0117, vol. 1, Nov. 1996, 343–346 vol.1. DOI: 10.1109/ULTSYM.1996.583988.
- [144] K.-Y. Hashimoto, *Surface Acoustic Wave Devices in Telecommunications: Modelling and Simulation*, en. Berlin Heidelberg: Springer-Verlag, 2000, ISBN: 978-3-540-67232-6. DOI: 10.1007/978-3-662-04223-6. [Online]. Available: <https://www.springer.com/gp/book/9783540672326> (visited on 01/18/2021).
- [145] K. Hanma and B. J. Hunsinger, “A triple transit suppression technique,” in *1976 Ultrasonics Symposium*, IEEE, 1976, pp. 328–331.
- [146] X. Sun, W. Liu, X. Shao, S. Zhou, W. Wang, and D. Lin, “Surface Acoustic Wave Gyroscopic Effect in an Interdigital Transducer,” *Sensors (Basel, Switzerland)*, vol. 19, no. 1, Dec. 2018, Number: 1, ISSN: 1424-8220. DOI: 10.3390/s19010106. [Online]. Available: <https://www.ncbi.nlm.nih.gov/pmc/articles/PMC6339056/> (visited on 01/18/2021).
- [147] B. A. Auld, *Acoustic fields and waves in solids*. Ripol Classic Publishing House, 1973.
- [148] X. Du, Y. Q. Fu, S. Tan, *et al.*, “Zno film thickness effect on surface acoustic wave modes and acoustic streaming,” *Applied Physics Letters*, vol. 93, no. 9, p. 094 105, 2008.

- [149] R. Tao, W. Wang, J. Luo, *et al.*, “Thin film flexible/bendable acoustic wave devices: Evolution, hybridization and decoupling of multiple acoustic wave modes,” *Surface and Coatings Technology*, vol. 357, pp. 587–594, 2019.
- [150] G. Armstrong and S. Crampin, “Preferential excitation of 2nd-mode piezoelectric surface waves in zinc-oxide-layered substrates,” *Electronics Letters*, vol. 9, no. 14, pp. 322–323, 1973.
- [151] C. Caliendo and F. Laidoudi, “Experimental and theoretical study of multifrequency surface acoustic wave devices in a single si/sio₂/zno piezoelectric structure,” *Sensors*, vol. 20, no. 5, p. 1380, 2020.
- [152] H. Nakahata, A. Hachigo, K. Higaki, S. Fujii, S.-i. Shikata, and N. Fujimori, “Theoretical study on saw characteristics of layered structures including a diamond layer,” *IEEE Transactions on Ultrasonics, Ferroelectrics, and Frequency Control*, vol. 42, no. 3, pp. 362–375, 1995.
- [153] M. El Hakiki, O. Elmazria, and P. Alnot, “Theoretical investigation of surface acoustic wave in the new, three-layered structure: Zno/aln/diamond,” *IEEE transactions on ultrasonics, ferroelectrics, and frequency control*, vol. 54, no. 3, pp. 676–681, 2007.
- [154] L. Le Brizoual, O. Elmazria, S. Zhgoon, A. Soussou, F. Sarry, and M. A. Djouadi, “Aln/zno/diamond waveguiding layer acoustic wave structure: Theoretical and experimental results,” *IEEE transactions on ultrasonics, ferroelectrics, and frequency control*, vol. 57, no. 8, pp. 1818–1824, 2010.
- [155] C. Zhou, Y. Yang, H. Jin, *et al.*, “Surface acoustic wave resonators based on (002) aln/pt/diamond/silicon layered structure,” *Thin Solid Films*, vol. 548, pp. 425–428, 2013.
- [156] A. Talbi, F. Sarry, L. Le Brizoual, O. Elmazria, and P. Alnot, “Sezawa mode saw pressure sensors based on zno/si structure,” *IEEE transactions on ultrasonics, ferroelectrics, and frequency control*, vol. 51, no. 11, pp. 1421–1426, 2004.

Chapter 3

A Fully Integrated Biosensing Platform Combining Acoustofluidics and Electromagnetic Metamaterials

In this chapter, an implementation for an integrated device based on electromagnetic metamaterial sensors and acoustofluidic transducers is described. The sensing and actuation capabilities of this device are investigated for a single geometry fabricated on a piezoelectric substrate.

This chapter is based on a published article in *Journal of Physics D: Applied Physics*¹.

¹Shahzad Zahertar^A, Yong Wang^B, Ran Tao^A, Jin Xie^B, Yong Qing Fu^A, Hamdi Torun^A, “A fully integrated biosensing platform combining acoustofluidics and electromagnetic metamaterials,” *Journal of Physics D: Applied Physics*, vol. 52, no. 48, p. 485 004, Sep. 2019. © IOP Publishing. Reproduced with permission. All rights reserved

A Faculty of Engineering and Environment, Northumbria University, Newcastle upon Tyne, NE1 8ST, UK

B The State Key Laboratory of Fluid Power and Mechatronic Systems, Zhejiang University, Hangzhou 310027, China

Abstract

A key challenge in biosensing technology is to develop integrated approaches with the multiple capabilities of bio-sampling, fluid manipulation, high-precision detection and wireless operation. In this work, we present a new concept of integrated biosensing technology using the functionalities of electromagnetic metamaterials and acoustofluidic technology onto a single platform. The new concept of using a single structure to perform microfluidic functions at acoustic frequencies and to detect the characteristics of liquid at microwave frequencies will enable the development of improved lab-on-a-chip devices. As a case study, we demonstrated efficient acoustofluidic functions of mixing and pumping using the designed surface acoustic wave (SAW) device on a LiNbO_3 substrate in an experimental setup that also allows the measurement of the electromagnetic characteristics of the interdigitated transducer (IDT) pattern of the same device. We demonstrated microfluidic functions at 10-25 MHz. The device also exhibits electromagnetic resonance at 4.4 GHz with a quality factor value of 294. We showed the device can be used for glucose detection with a good sensitivity of 28 MHz/(mg/ml).

3.1 Introduction

Wireless health monitoring has become a reality attributed to the development of novel biosensors for a diverse range of applications such as glucometers, blood pressure sensors, and pulse oximeters. Breadth of these applications have been expanding with the development of new sensing and manipulation methods in microsystems. Microsystems technology offers various methods for manipulation of biological fluids for biosampling and preparation purposes, including electromechanical pumping, electrophoresis, and ultrasonic/acoustic actuation. Surface Acoustic Wave (SAW) actuators have been successfully demonstrated for various microfluidic functions including liquid mixing, transport, jetting and nebulisation [1]. SAWs are based on generation of nanometre-scale vibrations on a solid surface. Advantages include freedom from mechanically moving parts and easy-integration into microfluidic systems [2], [3]. In addition to conventional SAW devices on rigid substrates, mechanically flexible and bendable thin film-based acoustic wave devices that are suitable for wearable applications have also been demonstrated [4], [5].

SAW structures can also be used for sensing based on the piezoelectric effect. The resonant fre-

quency of an acoustic transducer is shifted when an analyte is adsorbed on its surface due to mass loading, or in other cases, changes in elasticity, viscosity or conductivity, thus the frequency of the transducer can be used to detect molecular interactions. However, their major challenges for sensing remain unresolved. The sensitivity of SAW sensors increases significantly with their centre frequencies are increased, favouring smaller devices with resonant frequencies up to GHz levels [6]. Yet, this results in a higher energy attenuation along the interfacing surface with the contacting fluid [7]. In addition, smaller devices require stringent control in manufacturing. As an alternative technology, film bulk acoustic resonators (FBAR) have been used for sensing. The operation principle of the FBAR transducers is based on resonating bulk waves between two electrodes separated with a piezoelectric film layer. FBAR transducers generally favour being smaller, thus are operated at higher frequencies, offering a much higher sensitivity. FBAR devices can be used for liquid sampling but their liquid manipulation and microfluidic function are rather limited compared to that of SAW transducers [5]. Thus, it is very challenging to optimise a single acoustic wave transducer for both sensing and actuation. In addition, the selectivity of the acoustic sensors is relatively poor, and the resonant frequency is significantly affected by variations in ambient conditions, including non-specific mass loading and temperature [5], [6]. Different approaches have been utilised to address these challenges. For example, exciting shear horizontal waves on the surface of the SAW devices or exciting them using later electric fields can significantly reduce the loss in acoustic energy into the liquid environment. Efficient devices using these approaches have been demonstrated for sensing applications [8]–[10]. Furthermore, combining sensing and actuation capabilities will pave the path for an integrated biosensing platform with efficient sample handling and high precision detection capabilities.

A promising sensing technology with high quality factors at frequencies higher than those of acoustic wave devices is electromagnetic metamaterials. Metamaterials exhibit electromagnetic properties, which are not present in the conventional materials. These include negative values of electric permittivity and magnetic permeability that can be achieved simultaneously [11]. Among different geometrical configurations, split-ring resonators (SRRs) are one of the most common structures for electromagnetic metamaterials. A conventional SRR is simply a ring with a split, which is preferably made of a highly-conductive metal on a dielectric substrate. In addition to their favourable electromagnetic characteristics, SRR devices can be realised in a simple and cost-

effective manner with various flexible configurations. An SRR structure electrically forms an LC resonator at its magnetic resonance when a circulating resonant current is induced along its surface with the resonant frequency, inductance and capacitance determined by the geometry of the structure. SRR structures in centimetre to millimetre-scale, similar to SAW devices, are usually used for applications in microwave bands. Unlike the conventional types of passive resonators, an SRR structure typically exhibits very sharp resonant behaviour with quality factors larger than 1,000 at microwave frequencies [12]. Owing to their high-quality factors, the change in the resonant frequency of an SRR structure can be effectively used as a sensing mechanism, and it can be induced by a change in dielectric properties of the surrounding medium. Different SRR biosensors have been demonstrated, for which binding of biomolecules on top of an SRR structure alters the device capacitance [13]–[15]. In addition to their high sensitivity, these structures offer advantages over acoustic wave devices in terms of specificity, e.g., they are not significantly affected by non-specific mass loading and temperature.

In this chapter, we, for the first time, introduce a new concept of integrating a SAW device and an electromagnetic metamaterial using a single-electrode structure. The structure is inspired by SRRs with their capability of inducing resonating current for electromagnetic sensing. The SRR-inspired electromagnetic metamaterial structure allows wireless measurements with high quality factors. In addition, the single-electrode structure defines an acoustofluidic device on a piezoelectric substrate. The focus of our concept is to achieve a dual functionality using acoustic transduction and metamaterial-based sensing capable of providing non-invasive, portable, fast, affordable, and accurate biosensors. We report the fluid manipulation capabilities of an acoustic transducer together with its electromagnetic detection capability based on its metamaterial functionality, and successfully demonstrate our device for glucose sensing.

3.2 Experimental Section

Standard photolithography and lift-off processes were applied to develop semi-annular aluminium interdigitated electrodes with wavelength of $100\ \mu\text{m}$ on a lithium niobate substrate. For acoustic wave characterisation, electrode pads were connected to one port of a portable vector network analyser (KEYSIGHT N9913A) and S_{11} characteristics of the device was obtained. For testing actuation capability of the device for different microfluidic functions, the surface of the substrate

was treated with 1% CYTOP (Asahi Glass Co.) solution by drop-coating to make it hydrophobic. The droplet was placed on the treated surface of the device using a micropipette. A function generator (Marconi Instruments 2024) was utilised for generating SAWs on the surface. To do this, the function generator was set to operate at the intended resonant frequency based on the achieved S_{11} characterisation. The output of the function generator was fed to an amplifier (Amplifier Research 75A250) and the output of the amplifier was connected to the electrode pads of the IDTs. An RF power meter (Racal Instruments 9104) was utilised to measure the output power of the amplifier in Watts. For electromagnetic characterisation, monopole antennas were fabricated on an FR4 (Flame Retardant 4) substrate utilising a standard printing circuit board manufacturing technique. FR4 is the most commonly used dielectric for fabricating circuit boards due to reasons such as low cost, high integrability with electronics, thermal and mechanical properties [16]. All of which makes this material highly popular among other alternatives. Monopole Antennas were connected to ports of a vector network analyser (Agilent Technologies N5230A) to interrogate the device. Transmission spectrum was captured by the vector network analyser.

3.3 Results and Discussion

3.3.1 Acoustofluidic Characteristics

We have used a SAW device fabricated on a lithium niobate (LiNbO_3) substrate. The transducer has curved interdigitated (IDT) electrodes configured in a semi-annular pattern with an outer radius of 4 mm. The period of IDT electrodes is $100 \mu\text{m}$. The IDT electrodes were defined using sputtered aluminium and a standard photolithographic lift-off process. We coupled this device with a pair of monopole patch antennas realised on a standard printed circuit board substrate (FR4, glass-reinforced epoxy laminate material) as conceptually shown in Figure 3.1. The antennas are 26 mm in length and 3 mm in width. We connect the antennas to the ports of a vector network analyser (VNA) to excite the device electromagnetically and to measure the scattering parameters of the device between the antennas. In addition, the IDT pads allow us to excite the SAW device electrically by applying an RF signal for liquid manipulation experiments. During these experiments, we treat the surface of the structure with CYTOP, which is an amorphous fluoropolymer providing water and oil repellency, thus increased hydrophobicity. Figure 3.1(b) shows the cross-sectional schematic of the device depicting the layers. FR4 and LiNbO_3 provide dielectric substrates with

permittivity values of 4.3 for FR4 and $\epsilon_{11} = 85, \epsilon_{33} = 29.5$ for LiNbO₃.

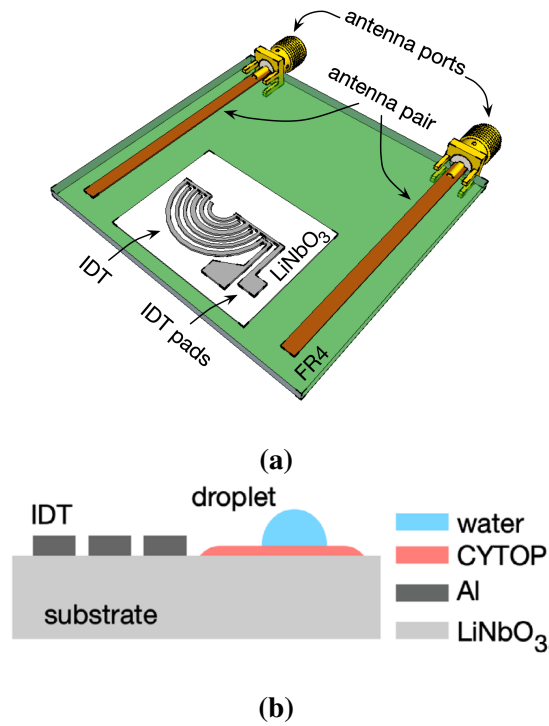


Figure 3.1: (a) Illustration of a SAW device on a LiNbO₃ substrate which is placed on a FR4 substrate including antennas for electromagnetic excitation. (b) Cross-sectional schematic of the device [17].

We measured the S_{11} (reflection coefficient from the port) spectrum of the SAW device at acoustic frequencies between the ports defined by the IDT pads. We observed four distinct frequencies between 10-25 MHz range as shown in Figure 3.2.

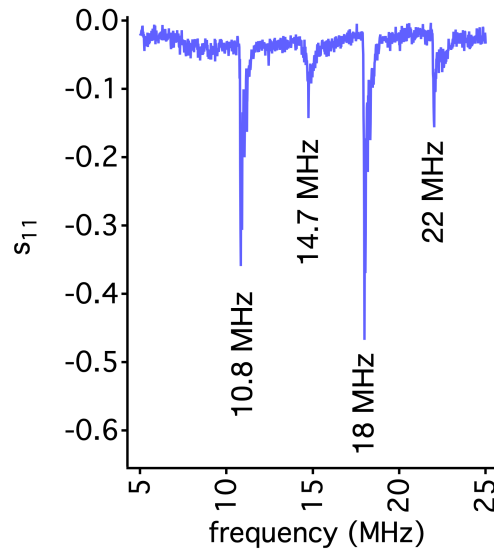


Figure 3.2: S_{11} spectrum of the SAW device at acoustic frequencies. We used a network analyser to measure the spectrum between the ports defined by the pads of the IDT electrodes [17].

The period of the IDT electrodes in the particular device is not constant and has some variation among the finger pairs as shown in Figure 3.3. We systematically measured the wavelength and observed a variation between $210 \mu\text{m}$ and $330 \mu\text{m}$. The variation in the wavelength results in distinct fundamental resonant frequencies.

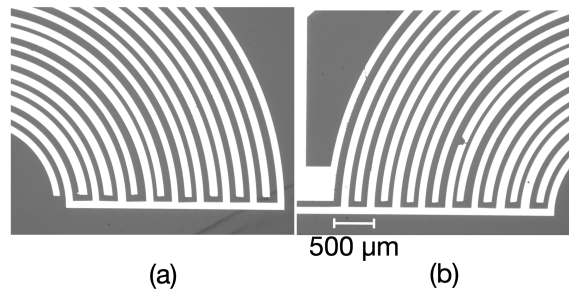


Figure 3.3: Micrographs of two sections of the IDT electrodes illustrating the variations in the finger widths of the IDT electrodes [17].

Among these, we observed the SAW device is efficient at 10.8 and 22 MHz. The wavelength of the IDTs determine the wavelength of the acoustic wave (λ) travelling over the surface, so its ratio to the acoustic wave velocity (ν) determines the acoustic resonant frequency ($f = \nu/\lambda$). On the other hand, the wavelength of the IDTs may alter the electromagnetic resonant frequency of the structure through the surface capacitance and inductance as explained in the next section.

The curved IDT electrode facilitates a focusing mechanism for the acoustic waves propagating

over the substrate. The acoustic wave energy is designed to be focused to the focal point due to the concentration of propagating waves. This was shown to be an effective way of mixing in microfluidics [18]. Consequently, we tested the mixing capability of our SAW device. Figure 3.4 shows the summary of mixing experiments. First, we treated the surface with a thin layer of CYTOP of ~ 500 nm thick. Then, we placed a sessile droplet of deionized water with a volume of $2 \mu\text{L}$ at the focal point of the SAW device. The water droplet comprised of polystyrene microbeads with a diameter of $10 \mu\text{m}$. First, we applied an RF signal at 10.8 MHz and observed the motion of polystyrene microbeads using a video camera. Figures 3.4(a) and 3.4(b) show the streamlines depicting the trajectories of the particles inside the droplet from a cross-sectional view. Upon the application of the RF excitation, the particles first started moving at a power of 0.5 W (Figure 3.4(a)), then gradually formed a steady streaming pattern (Figure 3.4(b)). We also observed the motion of the particles from the top view at a power of 0.44 W as shown in Figures 3.4(c) and 3.4(d). Digital particle image velocimetry results indicate circular mixing patterns in clockwise direction at steady state. We used a digital particle image velocimetry method to calculate the stream velocity inside the droplet [19], and Figure 3.4(e) shows the calculated distribution of velocity magnitudes of the particles at a steady state of streaming shown in Figure 3.4(d).

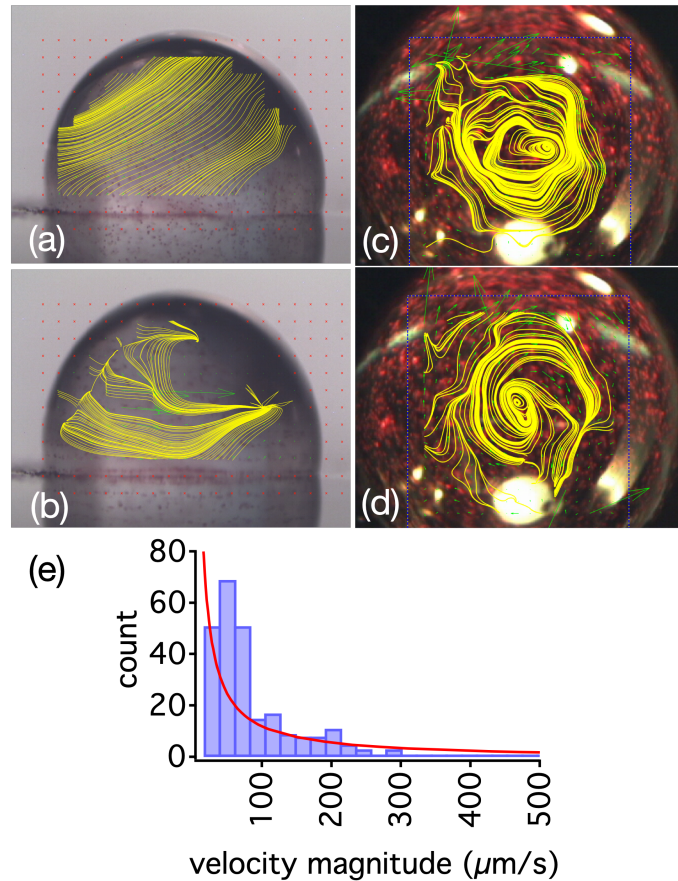


Figure 3.4: Experimental demonstration of streaming using polystyrene particles inside a droplet with a volume of $2 \mu\text{L}$, (a-b) cross-section view and (c-d) top view. (e) The distribution of velocity magnitudes in a time instant shown in subplot-(d) [17].

We then performed liquid pumping experiments using the same SAW device. We placed a droplet of deionized water with a volume of $1 \mu\text{L}$ on the CYTOP-treated surface along the central axis of the IDT electrodes. Then, we applied RF signals at various power levels and observed the motion of pumped droplets using a video camera. Figure 3.5(a-d) shows a sequence of snapshots while the droplet was pumped along the surface. Snapshots show consistent droplet shapes in linear translation over the surface. We repeated this experiment at 22 MHz and measured the speed of another droplet with the same volume of $1 \mu\text{L}$ by varying the power of the RF signal. The pumping of the droplet started at a threshold power of 4.3 W, below which the dominant function was mixing. Figure 3.5(e) depicts the speed of the droplet as a function of power. Each data point includes 5 different measurements and each error bar denotes the standard deviation of the measured speed. The speed (mm/s) increases with power (W) within the experimental range following a power law with an exponent of -3.6 .

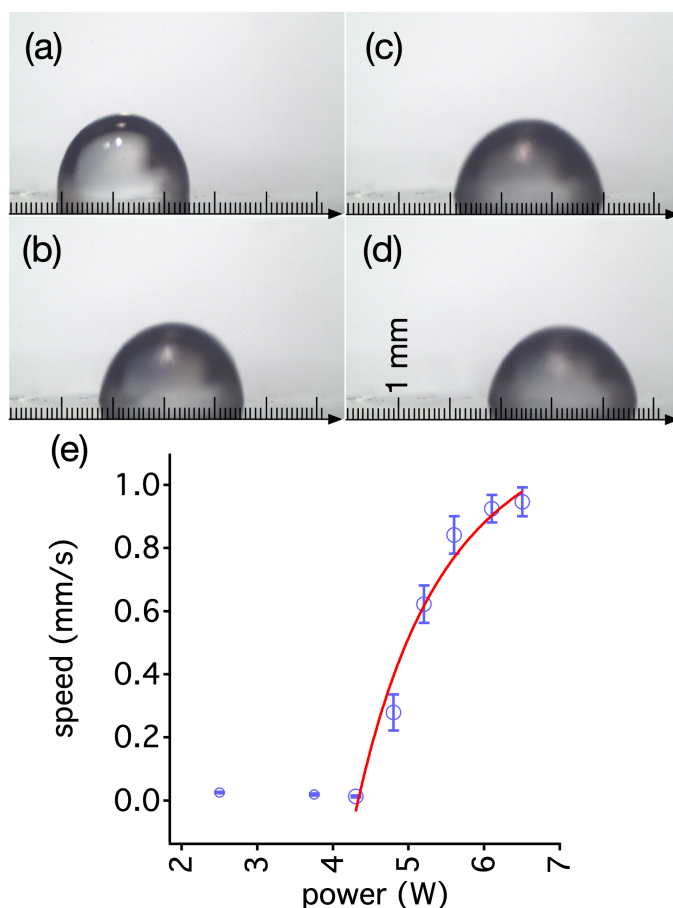


Figure 3.5: Experimental demonstration of pumping function. Subfigures (a-d) show a sequence of snapshots while a droplet with a volume of $1 \mu\text{L}$ is pumped along the surface. (e) Pumping speed, s , increases with power level, P , following $P \propto s^{-3.6}$ [17].

After mixing and pumping experiments, we used the device for liquid jetting experiments. The location of the droplet on the substrate is particularly important for this device since the traveling SAW is focused due to the circular nature of IDT electrodes. We observed that the droplets placed on the focal point can be manipulated vertically. The intensity of SAW is concentrated over a relatively small area at the focal point, so liquid manipulation functions can be implemented effectively. Figures 3.6(a) to 3.6(c) show snapshots of a droplet with a volume of $1 \mu\text{L}$ placed at the focal point of the IDT when a power of 2.9 W at 22 MHz was applied to the IDTs. The droplet did not move from its resting location but was actuated along the vertical axis away from the substrate. We repeated this experiment at different power levels and measured the height of manipulated droplet with increasing power. The maximum height reaches a settled value of 2 mm above its original height at its resting position. The relationship between the ejected high (h) and the applied power (P) can be described using the following equation for the specific experi-

ment:

$$h = 2.62 - 2.74e^{-\frac{P-0.02}{1.066}} \quad (3.1)$$

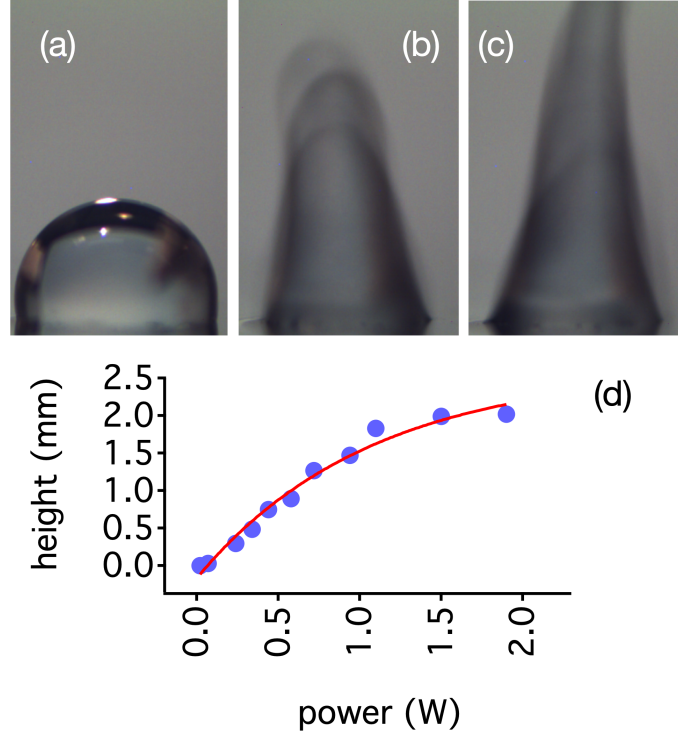


Figure 3.6: Experimental demonstration of jetting function. Subfigures (a-c) show snapshots while a droplet with a volume of $1 \mu\text{L}$ is manipulated at a fixed location over the surface.(d) The height of the manipulated droplet measured from its original height increases with applied power [17].

3.3.2 Electromagnetic Characteristics

In addition to the above microfluidic functionalities, we also characterised electromagnetic properties of the structure. When the transducer is electromagnetically excited using the antenna pair of Figure 3.1, the magnetic field perpendicular to the SAW IDT supports circulating current at its electromagnetic resonant frequency which is determined by the geometry of the IDTs. The resonant frequency, f_0 , and quality factor, Q , of the resonator can be expressed as follows [20].

$$f_0 = \frac{1}{2\pi\sqrt{L_m(C_m + C_b)}} \quad (3.2)$$

$$Q = \frac{1}{R} \sqrt{\frac{L_m}{C_m + C_b}} \quad (3.3)$$

Where C_m is the capacitance of the structure and C_b is the effective capacitance of the liquid sample placed within the vicinity of the resonator. L_m is the inductance of the structure and R is the equivalent resistance of the structure and the sample. Since the resonant frequency depends on total capacitance of the structure, which in turn depends on the relative permittivity of the sample, any changes in the physical property of the sample can be observed as changes in f_0 and Q .

Figure 3.7(a) shows the simulated S_{21} spectrum (transmission coefficient between the ports) of the device. We have used commercially available electromagnetic simulation software (CST Studio Suite, Darmstadt, Germany) for all our simulations. The energy is dissipated across the transducer at the resonance, resulting in a sharp dip signature in the S_{21} spectrum measured between the antenna ports. The spectrum indicates a sharp dip at the resonant frequency of 4.41 GHz with a quality factor of 294. A closer examination of the surface current density at the resonance reveals the pattern of circulating current along the IDT electrodes as shown in Figure 3.7(b). It is possible to obtain an electromagnetic resonant frequency at 4.41 GHz using a structure with an outer radius of 4 mm, attributed to the SRR-inspired metamaterial configuration that allows the miniaturising of the device to a subwavelength.

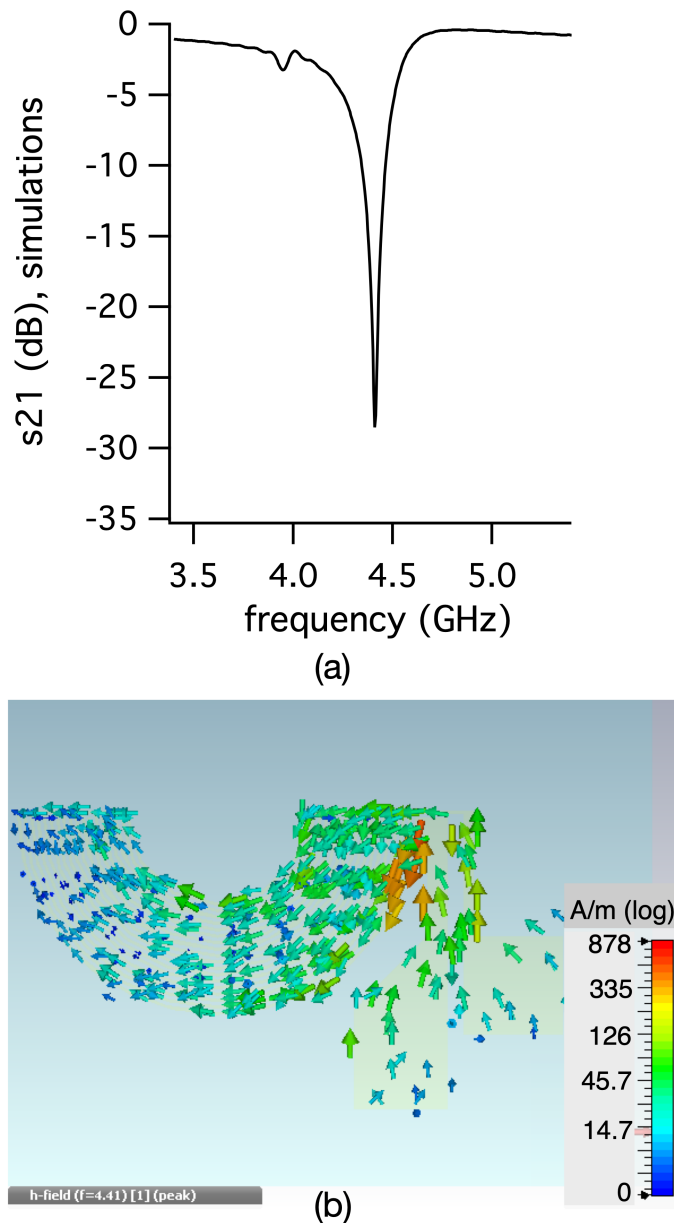


Figure 3.7: Simulated (a) S_{21} spectrum of the SAW device, (b) profile of surface current density at the resonance [17].

Both the circulating current pattern and the electromagnetic resonant frequency of the device are changed when a liquid droplet is placed within the vicinity of the structure. This can be utilised as a sensing mechanism for the location of the droplet. We characterised this mechanism by moving a deionized water droplet with a volume of $2 \mu\text{l}$ over the surface of the substrate by 4 mm. Figure 3.8(a) and (b) shows the simulated and experimentally obtained S_{21} spectra of the sensor while the droplet is moving, respectively. When the droplet was placed 1.5 mm away from the edge of the IDT electrodes, the resonant frequency of the device was dropped to 4 GHz due to

the increased value of C_b . Then, the droplet was gradually moved away from the device along the direction shown in the inset in Figure 3.8(b). As the droplet was moved away, the value of C_b was decreased, so the resonant frequency of the device was gradually increased. Figure 3.8(c) shows the simulated and experimentally obtained relationship between the resonant frequency and the droplet distance relative to the edge of the IDT electrodes. During the experiments, we used a vector network analyser to measure the S_{21} spectra of the device between the antenna ports depicted in Figure 3.1. We observed a linear relationship within the measured displacement range. The slope of the linear fit lines to the experimental and simulated data sets are 28.9 MHz/mm and 35.3 MHz/mm, respectively. The experimentally obtained values of resonant frequency are lower than the simulated ones, which may indicate lower values of dielectric constants in the simulated model as compared with the fabricated device. However, we have used nominal values of the material properties in the material library of the simulator without any fitting parameters. Nevertheless, the simulation results are in a good agreement with that of the experimental ones.

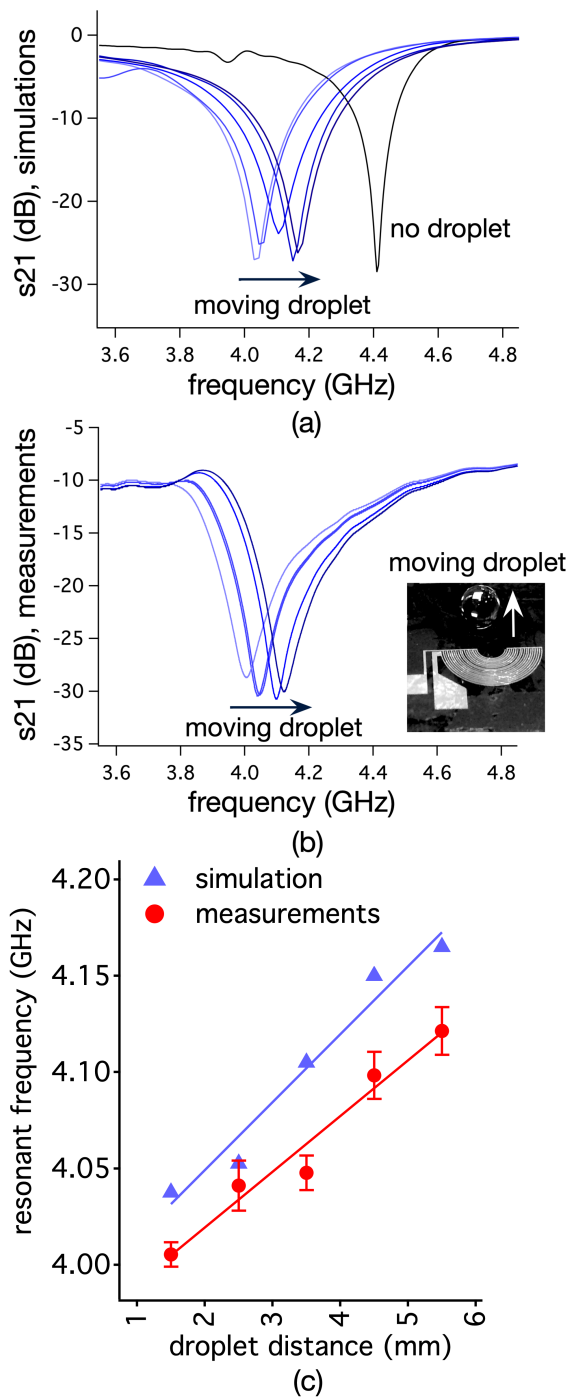


Figure 3.8: Simulated, b) measured S₂₁ spectra of the SAW device while a liquid droplet with a volume of 2 μl is actuated on its substrate. (c) The shift in the resonant frequency of the SAW device due to the movement of a liquid droplet with a volume of 2 μl . The distance of the droplet is measured from the edge of the IDT [17].

When the location of the droplet is fixed on the substrate, the composition of the droplet can be measured by monitoring the electromagnetic resonant frequency of the device. This approach is

simple to implement and relies mainly on the interaction of the sample and the structure under an electromagnetic field. This method is applicable to detect concentration of molecules inside a droplet. In this work, we have used our method for the detection of glucose as an exemplar of the wider applicability of our approach. The permittivity of a droplet of glucose solution decreases with increasing concentration of glucose [21], [22]. Therefore, C_b decreases with concentration of glucose, whereas L_m generally stays constant. Thus, the resonant frequency increases with the glucose concentration as demonstrated before [23].

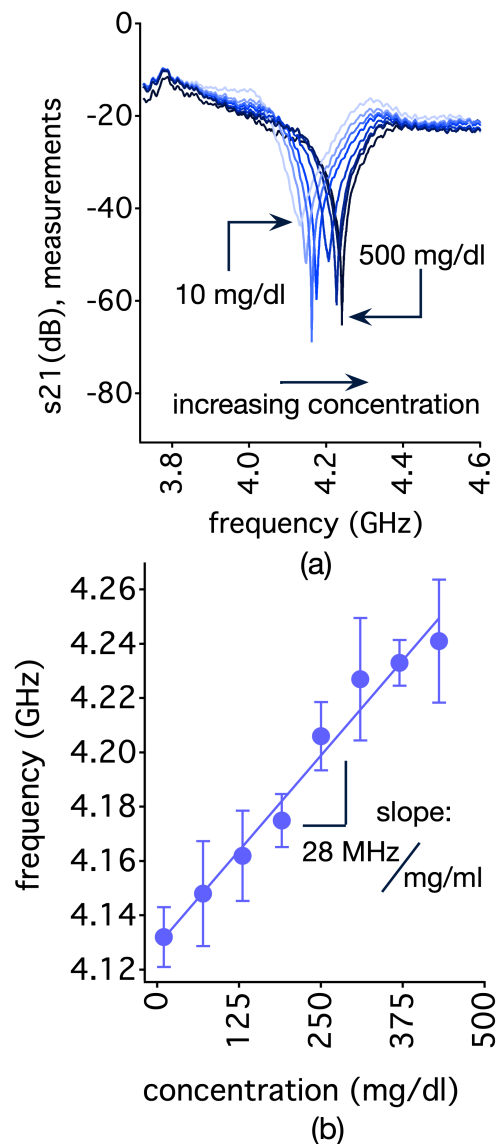


Figure 3.9: (a) Measured S_{21} spectra of the device while the concentration of glucose in a $2 \mu\text{L}$ -droplet is increased. (b) Change in the resonant frequency of the device with concentration of glucose [17].

We prepared glucose solutions with various concentrations within a physiological range of 10-500 mg/dl in droplets of 2 μ l. Then, we placed the droplets sequentially to the same location over the substrate while monitoring the S_{21} spectra of the sensor between the ports of the pair of antennas. Between the application of each droplet, we cleaned the surface using deionized water and dried the sample surface carefully. Figure 3.9(a) shows the recorded S_{21} spectra for the samples with different glucose concentrations. The electromagnetic resonant frequency of the transducer increases with glucose concentration as shown in Figure 3.8(b). We repeated the experiments 10 times and the error bars indicate the standard error of the mean. We observe a linear relationship between the resonant frequency and the concentration within its measurement range with a sensitivity of 28 MHz/(mg/ml), corresponding to 5.05 MHz/mM. This level is comparable to SAW-based acoustofluidic glucose sensors with reported sensitivities of 7.184 MHz/mM [24], 1.589 MHz/mM [25] and 0.93 MHz/log(M) [26]. Based on the above results, we can confirm that this newly developed concept and device can realise the integrated functions of both acoustofluidics and biosensing.

3.4 Conclusion

In summary, we present a new concept towards the realisation of integrated biosensing platforms. We have successfully demonstrated that a conventional SAW transducer can be employed as a metamaterial-based sensor, the readout of which can be implemented wirelessly using a simple setup.

In this work, we have used a curved IDT SAW device fabricated on a LiNbO₃ substrate. We demonstrated liquid mixing, pumping and jetting functions at power levels of 0.2-7 W. In addition to conventional acoustofluidic functionalities, the SAW device acts as an effective electromagnetic metamaterial under electromagnetic excitation. We used a simple setup comprising of a pair of monopole patch antennas on a FR4 substrate for the excitation. The nominal resonant frequency of the device is at 4.41 GHz and the quality factor is 294.

We present the liquid sensing capability of the wireless sensing architecture in two scenarios. Firstly, the droplet motion over the substrate can be measured effectively by monitoring the resonant frequency of the device. Secondly, for a droplet at a fixed location over the substrate, the

composition of the droplet can be measured. Consequently, we have used our device for glucose sensing. Our experiments confirm that the concentration of glucose in deionized water droplets with volumes of $2 \mu\text{l}$ can be measured with a sensitivity of $28 \text{ MHz}/(\text{mg}/\text{ml})$ within a range of $10\text{-}500 \text{ mg}/\text{dl}$. Moving the droplet further from the resonator, decreased the effective capacitance and therefore, the resonance was shifted towards higher frequencies. The obtained results were confirmed through simulations.

We expect the impact of our work will be beyond the case study with the potential of delivering portable, fast, affordable and accurate monitoring microsystems with intervention capabilities. In the next chapter, a geometry comprising circular IDTs on a LiNbO_3 substrate that is inspired by dual split-ring resonators (DSRRs) is proposed for an integrated biosensing platform. DSRRs are used conventionally in metamaterial-based sensors with high quality factors in order to lower the operating frequency of the device in microwave regime. DSRRs can also contribute to miniaturisation of the device for a target frequency by increasing the effective capacitance of the system. However, this geometry has not been explored in acoustic frequencies for microfluidic applications. The sensing capability of the proposed geometry is investigated through various experiments in microwave frequency band and in radio frequencies. Also, the streaming capability of the resonator is characterised by applying power to the electrodes of the device.

References

- [1] J. Friend and L. Y. Yeo, “Microscale acoustofluidics: Microfluidics driven via acoustics and ultrasonics,” *Reviews of Modern Physics*, vol. 83, no. 2, pp. 647–704, Jun. 2011, Publisher: American Physical Society. DOI: 10.1103/RevModPhys.83.647. [Online]. Available: <https://link.aps.org/doi/10.1103/RevModPhys.83.647> (visited on 01/15/2021).
- [2] A. J. Flewitt, J. K. Luo, Y. Q. Fu, *et al.*, “ZnO based SAW and FBAR devices for bio-sensing applications,” en, *Journal of Non-Newtonian Fluid Mechanics, Rheometry (and General Rheology): Festschrift dedicated to Professor K Walters FRS on the occasion of his 80th birthday*, vol. 222, pp. 209–216, Aug. 2015, ISSN: 0377-0257. DOI: 10.1016/j.jnnfm.2014.12.002. [Online]. Available: <http://www.sciencedirect.com/science/article/pii/S0377025714002195> (visited on 01/15/2021).
- [3] G. Destgeer, H. Cho, B. H. Ha, J. H. Jung, J. Park, and H. J. Sung, “Acoustofluidic particle manipulation inside a sessile droplet: Four distinct regimes of particle concentration,” en, *Lab on a Chip*, vol. 16, no. 4, pp. 660–667, Feb. 2016, Publisher: The Royal Society of Chemistry, ISSN: 1473-0189. DOI: 10.1039/C5LC01104C. [Online]. Available: <https://pubs.rsc.org/en/content/articlelanding/2016/lc/c5lc01104c> (visited on 01/15/2021).
- [4] Y. Q. Fu, J. K. Luo, X. Y. Du, *et al.*, “Recent developments on ZnO films for acoustic wave based bio-sensing and microfluidic applications: A review,” en, *Sensors and Actuators B: Chemical*, vol. 143, no. 2, pp. 606–619, Jan. 2010, ISSN: 0925-4005. DOI: 10.1016/j.snb.2009.10.010. [Online]. Available: <http://www.sciencedirect.com/science/article/pii/S0925400509007783> (visited on 01/15/2021).
- [5] Y. Q. Fu, J. K. Luo, N. T. Nguyen, *et al.*, “Advances in piezoelectric thin films for acoustic biosensors, acoustofluidics and lab-on-chip applications,” en, *Progress in Materials Science*, vol. 89, pp. 31–91, Aug. 2017, ISSN: 0079-6425. DOI: 10.1016/j.pmatsci.

- 2017.04.006. [Online]. Available: <http://www.sciencedirect.com/science/article/pii/S0079642517300403> (visited on 01/15/2021).
- [6] A. Mujahid and F. L. Dickert, "Surface Acoustic Wave (SAW) for Chemical Sensing Applications of Recognition Layers," en, *Sensors*, vol. 17, no. 12, p. 2716, Dec. 2017, Number: 12 Publisher: Multidisciplinary Digital Publishing Institute. DOI: 10.3390/s17122716. [Online]. Available: <https://www.mdpi.com/1424-8220/17/12/2716> (visited on 01/15/2021).
- [7] X. Ding, P. Li, S.-C. S. Lin, *et al.*, "Surface acoustic wave microfluidics," en, *Lab on a Chip*, vol. 13, no. 18, pp. 3626–3649, Aug. 2013, Publisher: The Royal Society of Chemistry, ISSN: 1473-0189. DOI: 10.1039/C3LC50361E. [Online]. Available: <https://pubs.rsc.org/en/content/articlelanding/2013/lc/c3lc50361e> (visited on 01/15/2021).
- [8] O. I. Guliy, B. D. Zaitsev, I. E. Kuznetsova, *et al.*, "Investigation of specific interactions between microbial cells and polyclonal antibodies using a resonator with lateral electric field," en, *Microbiology*, vol. 82, no. 2, pp. 215–223, Mar. 2013, ISSN: 1608-3237. DOI: 10.1134/S0026261713020057. [Online]. Available: <https://doi.org/10.1134/S0026261713020057> (visited on 01/15/2021).
- [9] O. I. Guliy, B. D. Zaitsev, I. A. Borodina, *et al.*, "The biological acoustic sensor to record the interactions of the microbial cells with the phage antibodies in conducting suspensions," en, *Talanta*, vol. 178, pp. 569–576, Feb. 2018, ISSN: 0039-9140. DOI: 10.1016/j.talanta.2017.09.076. [Online]. Available: <http://www.sciencedirect.com/science/article/pii/S0039914017310202> (visited on 01/15/2021).
- [10] F. Bender, R. E. Mohler, A. J. Ricco, and F. Josse, "Identification and Quantification of Aqueous Aromatic Hydrocarbons Using SH-Surface Acoustic Wave Sensors," *Analytical Chemistry*, vol. 86, no. 3, pp. 1794–1799, Feb. 2014, Publisher: American Chemical Society, ISSN: 0003-2700. DOI: 10.1021/ac403724f. [Online]. Available: <https://doi.org/10.1021/ac403724f> (visited on 01/15/2021).
- [11] D. Schurig, J. J. Mock, B. J. Justice, *et al.*, "Metamaterial Electromagnetic Cloak at Microwave Frequencies," en, *Science*, vol. 314, no. 5801, pp. 977–980, Nov. 2006, Publisher: American Association for the Advancement of Science Section: Report, ISSN: 0036-8075, 1095-9203. DOI: 10.1126/science.1133628. [Online]. Available: <https://science.sciencemag.org/content/314/5801/977> (visited on 01/15/2021).

- [12] H. Torun, S. Sadeghzadeh, and A. D. Yalcinkaya, “Note: Tunable overlapping half-ring resonator,” *Review of Scientific Instruments*, vol. 84, no. 10, p. 106 107, Oct. 2013, Publisher: American Institute of Physics, ISSN: 0034-6748. DOI: 10.1063/1.4825347. [Online]. Available: <https://aip.scitation.org/doi/10.1063/1.4825347> (visited on 01/15/2021).
- [13] H.-J. Lee, J.-H. Lee, H.-S. Moon, *et al.*, “A planar split-ring resonator-based microwave biosensor for label-free detection of biomolecules,” en, *Sensors and Actuators B: Chemical*, vol. 169, pp. 26–31, Jul. 2012, ISSN: 0925-4005. DOI: 10.1016/j.snb.2012.01.044. [Online]. Available: <http://www.sciencedirect.com/science/article/pii/S0925400512000676> (visited on 01/15/2021).
- [14] W. Withayachumnankul, K. Jaruwongrungssee, A. Tuantranont, C. Fumeaux, and D. Abbott, “Metamaterial-based microfluidic sensor for dielectric characterization,” en, *Sensors and Actuators A: Physical*, vol. 189, pp. 233–237, Jan. 2013, ISSN: 0924-4247. DOI: 10.1016/j.sna.2012.10.027. [Online]. Available: <http://www.sciencedirect.com/science/article/pii/S0924424712006371> (visited on 01/15/2021).
- [15] A. Salim and S. Lim, “Complementary Split-Ring Resonator-Loaded Microfluidic Ethanol Chemical Sensor,” en, *Sensors*, vol. 16, no. 11, p. 1802, Nov. 2016, Number: 11 Publisher: Multidisciplinary Digital Publishing Institute. DOI: 10.3390/s16111802. [Online]. Available: <https://www.mdpi.com/1424-8220/16/11/1802> (visited on 01/15/2021).
- [16] G. Hatipoglu and H. Ürey, “Fr4-based electromagnetic energy harvester for wireless sensor nodes,” *Smart Materials and Structures*, vol. 19, no. 1, p. 015 022, 2009.
- [17] S. Zahertar, Y. Wang, R. Tao, J. Xie, Y. Q. Fu, and H. Torun, “A fully integrated biosensing platform combining acoustofluidics and electromagnetic metamaterials,” en, *Journal of Physics D: Applied Physics*, vol. 52, no. 48, p. 485 004, Sep. 2019, Publisher: IOP Publishing, ISSN: 0022-3727. DOI: 10.1088/1361-6463/ab3f7d. [Online]. Available: <https://doi.org/10.1088/1361-6463/ab3f7d> (visited on 01/15/2021).
- [18] R. Shilton, M. K. Tan, L. Y. Yeo, and J. R. Friend, “Particle concentration and mixing in microdrops driven by focused surface acoustic waves,” *Journal of Applied Physics*, vol. 104, no. 1, p. 014 910, Jul. 2008, Publisher: American Institute of Physics, ISSN: 0021-8979. DOI: 10.1063/1.2951467. [Online]. Available: <https://aip.scitation.org/doi/10.1063/1.2951467> (visited on 01/15/2021).

- [19] W. Thielicke and E. Stamhuis, "PIVlab – Towards User-friendly, Affordable and Accurate Digital Particle Image Velocimetry in MATLAB," en, *Journal of Open Research Software*, vol. 2, no. 1, e30, Oct. 2014, Number: 1 Publisher: Ubiquity Press, ISSN: 2049-9647. DOI: 10.5334/jors.bl. [Online]. Available: <http://openresearchsoftware.metajnl.com/articles/10.5334/jors.bl/> (visited on 01/15/2021).
- [20] H. Torun, F. Cagri Top, G. Dundar, and A. D. Yalcinkaya, "An antenna-coupled splitting resonator for biosensing," *Journal of Applied Physics*, vol. 116, no. 12, p. 124 701, Sep. 2014, Publisher: American Institute of Physics, ISSN: 0021-8979. DOI: 10.1063/1.4896261. [Online]. Available: <https://aip.scitation.org/doi/10.1063/1.4896261> (visited on 01/15/2021).
- [21] V. Turgul and I. Kale, "Characterization of the complex permittivity of glucose/water solutions for noninvasive RF/Microwave blood glucose sensing," in *2016 IEEE International Instrumentation and Measurement Technology Conference Proceedings*, May 2016, pp. 1–5. DOI: 10.1109/I2MTC.2016.7520546.
- [22] I. U. of Radio Science, Ed., *2011 XXXth URSI general assembly and scientific symposium: [URSI GASS 2011] ; Istanbul, Turkey, 13 - 20 August 2011* (2011 XXXth URSI General Assembly and Scientific Symposium), eng. Piscataway, NJ: IEEE, 2011, Meeting Name: General assembly and scientific symposium. International Union of Radio Science (URSI) Pages: 1-4 Publication Title: Glucose-dependent dielectric properties of blood plasma, ISBN: 978-1-4244-6051-9 978-1-4244-5117-3. DOI: 10.1109/URSIGASS.2011.6051324.
- [23] B. Camli, E. Altinagac, H. Kizil, H. Torun, G. Dundar, and A. D. Yalcinkaya, "Loop Antenna Driven Double Microwave Resonator-Based Sensors Incorporating PDMS Microchannels on Glass Substrates," en, *Proceedings*, vol. 2, no. 13, p. 1064, 2018, Number: 13 Publisher: Multidisciplinary Digital Publishing Institute. DOI: 10.3390/proceedings2131064. [Online]. Available: <https://www.mdpi.com/2504-3900/2/13/1064> (visited on 01/15/2021).
- [24] J. Luo, P. Luo, M. Xie, *et al.*, "A new type of glucose biosensor based on surface acoustic wave resonator using Mn-doped ZnO multilayer structure," en, *Biosensors and Bioelectronics*, vol. 49, pp. 512–518, Nov. 2013, ISSN: 0956-5663. DOI: 10.1016/j.bios.2013.05.021. [Online]. Available: <http://www.sciencedirect.com/science/article/pii/S095656631300345X> (visited on 01/15/2021).

- [25] J. Luo, M. Xie, P. Luo, B. Zhao, K. Du, and P. Fan, “A sensitive glucose biosensor without using glucose test strips based on ZnO/SiO₂/Si surface acoustic wave device,” en, *Materials Letters*, vol. 130, pp. 14–16, Sep. 2014, ISSN: 0167-577X. DOI: 10.1016/j.matlet.2014.05.073. [Online]. Available: <http://www.sciencedirect.com/science/article/pii/S0167577X14008623> (visited on 01/15/2021).
- [26] F.-F. Chou and J.-S. Shih, “Electrochemical electrode/SAW system for metal ions and glucose in solutions,” en, *Sensors and Actuators B: Chemical*, vol. 129, no. 1, pp. 176–183, Jan. 2008, ISSN: 0925-4005. DOI: 10.1016/j.snb.2007.07.101. [Online]. Available: <http://www.sciencedirect.com/science/article/pii/S0925400507005874> (visited on 01/15/2021).

Chapter 4

DSRR-Inspired Geometry for Integration of Metamaterial-Based Sensing and Acoustofluidic-Based Streaming

In this chapter, a new single structure is defined, which can be utilised to generate streaming inside microfluids and also can be used for sensing purposes. The structures defining circular interdigitated electrodes, inspired by a dual split ring resonator geometry, are patterned on a piezoelectric substrate as an integrated device for sensing and actuation. The wireless-sensing capability of the device is presented based on detection of electrical permittivity of the samples followed by a case study in monitoring the fermentation process of yeast cells. Also, streaming is achieved using the same device to demonstrate the microfluidic manipulation capability of the actuator. This structure has the potential to be effectively integrated into Lab-on-chip systems for point-of-care applications.

This chapter is a modified version of a published article in *Sensors & Diagnostics*¹.

¹Shahzad Zahertar^A, Hamdi Torun^B, Ran Tao^{BA}, Pep Canyelles-Pericas^{CA}, Jingting Luo^{BA}, Qiang Wu^A, Yong-Qing Fu^A, “An integrated platform for metamaterial-based sensing and surface acoustic wave-based acoustofluidics utilising circular interdigital transducers”, *Sens. Diagn.*, vol. 1, no. 2, p. 270-279, 2022. RSC.

A Faculty of Engineering & Environment, University of Northumbria, Newcastle upon Tyne, UK

B Shenzhen Key Laboratory of Advanced Thin Films and Applications, College of Physics and Optoelectronic Engineering, Shenzhen University, China

We propose a new device based on circular interdigitated transducers that are configured in a dual split ring resonator (DSRR) geometry. The DSRR includes two individual SRRs with gaps positioned on the opposite direction from each other. The DSRRs are utilised to increase the effective capacitance of the resonator. This can be advantageous in several domains including lowering the resonant frequency in a specific frequency band, to be employed as multi-band sensors, controlling the frequency by altering the position of the gap on one of the resonators, and can help design a more compact device at a target frequency [1], [2]. Also, circular design of IDTs focuses traveling surface acoustic waves in a focal point and acoustic energy from various directions are accumulated in this point, which can be beneficial for effective mixing/streaming of the particle, efficient jetting and nebulisation [3]–[5]. In this chapter, we describe the design, fabrication and characterization of this device. Also, we demonstrate sensing capabilities of the device based on different experiments where we measured glucose concentration of droplets and monitored yeast fermentation process over time.

4.1 Fabrication and Materials

A device comprising two sets of circular IDT patterns based on a dual split-ring resonator geometry, DSRR (as shown in inset of Figure 4.1), was fabricated by patterning 20/100 nm Cr/Au circular interdigitated electrodes on a 500- μm thick piezoelectric Lithium Niobate (LiNbO_3) substrate through standard photolithography and lift-off processes. Each set of rings consists of 15 pairs of IDTs with the wavelength of $\lambda = 200\mu\text{m}$. The smaller ring has an inner radius of 4.4 mm, and an outer radius of 11 mm. The larger ring has an inner radius of 11 mm and an outer radius of 13.95 mm. The gap of each split is 1.2 mm.

4.2 Results and Discussions

4.2.1 Electromagnetic Characterisation

We characterised the electromagnetic properties of our design through simulations and experimentally. The obtained results are illustrated in Figure 4.1. Depending on the excitation conditions

C Department of Integrated Devices and Systems, MESA+ Institute, University of Twente, Enschede, 7522 NB, The Netherlands

and the directions of electric and magnetic fields, the structure would behave differently; the nature of each excited resonant frequency in the device can be electric, magnetic, or a combination of electric and magnetic resonances [6]. If a circulating current path is induced inside the device, then the resonant frequency is called a magnetic resonance and the fundamental magnetic resonant frequency can be modelled as a resistor-inductor-capacitor (RLC) resonator. A circulating current path can be induced inside the structure in various scenarios: a) when magnetic field is perpendicular to the plane of the device; b) when electric field is inducing polarization across the structure and generating a circulating current; c) when magnetic field is perpendicular to the plane of the structure and at the same time, electric field is supporting the circulation of the current through polarisation. The fundamental magnetic resonant frequency, and the quality factor, of the resonance in a structure can be calculated using a basic lumped RLC model [7]–[9] ($f_0 = \frac{1}{2\pi\sqrt{L_{eff}C_{eff}}}$ with $C_{eff} = C_{surface} + C_{gap}$; the L_{eff} is the effective inductance, and C_{eff} , $C_{surface}$, and C_{gap} are effective capacitance, surface capacitance attributed to the induced current inside the ring, and the capacitance resulted from the slits as well as IDTs of the structure; $Q = \frac{1}{R}\sqrt{\frac{L_{eff}}{C_{eff}}}$; R is the equivalent resistance of the device respectively). These parameters are determined by the geometry of the device, and the dielectric constant of the medium. Altering any of these parameters will translate into a shift in the resonant frequency, and therefore, this principle can be employed as a sensing mechanism.

In order to understand the behaviour of the resonator and the nature of the resonances, we used a commercially available electromagnetic simulation software (CST Studio Suite, Darmstadt, Germany). The boundary conditions in the simulation model were set so that the magnetic field is along x-axis, electric field is along y-axis and the propagation vector is perpendicular to the plane of the device. The directions of the electric and magnetic fields used in simulation are illustrated in the inset of Figure 4.1(a) with respect to the device. In this case, electric field polarizes the device in y-direction and supports two circulating current paths on right and left sides of the ring, resulting in a magnetic resonant frequency of 3.68 GHz. In the next step, we placed a cone-shape structure to model a droplet inside the inner circle of the device with varying electric permittivity to investigate the effects of changing the dielectric constant of the medium in the vicinity of the device. In one setting, the relative permittivity was set ($\epsilon_r = 1$) to mimic vacuum, and in the other setting, the permittivity was set to ($\epsilon_r = 80$) to model water as the droplet material. The reflection

scattering parameters (S_{11}) for both cases are presented in Figure 4.1 (a). For a higher dielectric constant ($\epsilon_r = 80$) of the material of the droplet, the resonant frequency shifted 11 MHz towards higher frequencies. We also extracted current density patterns that are induced in the device in both cases for a better understanding of the behaviour of the device. The results are depicted in Figure 4.1 (c-d). The current circulation is more intense in the case of vacuum compared to the case in which ($\epsilon_r = 80$); This phenomenon itself is an indicator of stronger effective capacitance and inductance in this excitation setting, and therefore explains a lower magnetic frequency of vacuum compared to the water droplet.

4.2.2 Experimental Setup

We performed experiments to confirm our simulation results in the next phase. We used a copper loop antenna with the perimeter of 8.8 cm and connected it to one port of a Vector Network Analyser (VNA) and recorded S_{11} spectrum. The electromagnetic wave is fluctuated around the antenna and the direction and strength of electric and magnetic fields vary spatially and temporally with respect to antenna position. The direction of the electric and magnetic fields can excite the device under study differently, and lead to a distinct resonant behaviour [6], [10]. We placed the fabricated resonator underneath of the loop antenna to couple with each other as shown in inset of Figure 4.1(b). After measuring the reflection parameters of the coupled system, we added a droplet of 30 μL of deionised water (DI) water at the centre of the inner circle and measured the S_{11} spectrum again as shown in Figure 4.1(b). The resonant frequency of the device shifts towards higher frequencies (21 MHz) with the presence of DI droplet as predicted by the simulations. The slight discrepancies between simulations and experiments can be due to several factors; one of them can be because the use of the loop antenna in the experimental setup, whereas planar boundaries were used in simulations to excite the resonator. Also, in simulations, the ideal environment is considered for ease of use and there might be inevitable differences between material properties loaded from the simulator library and the actual experimental setting.

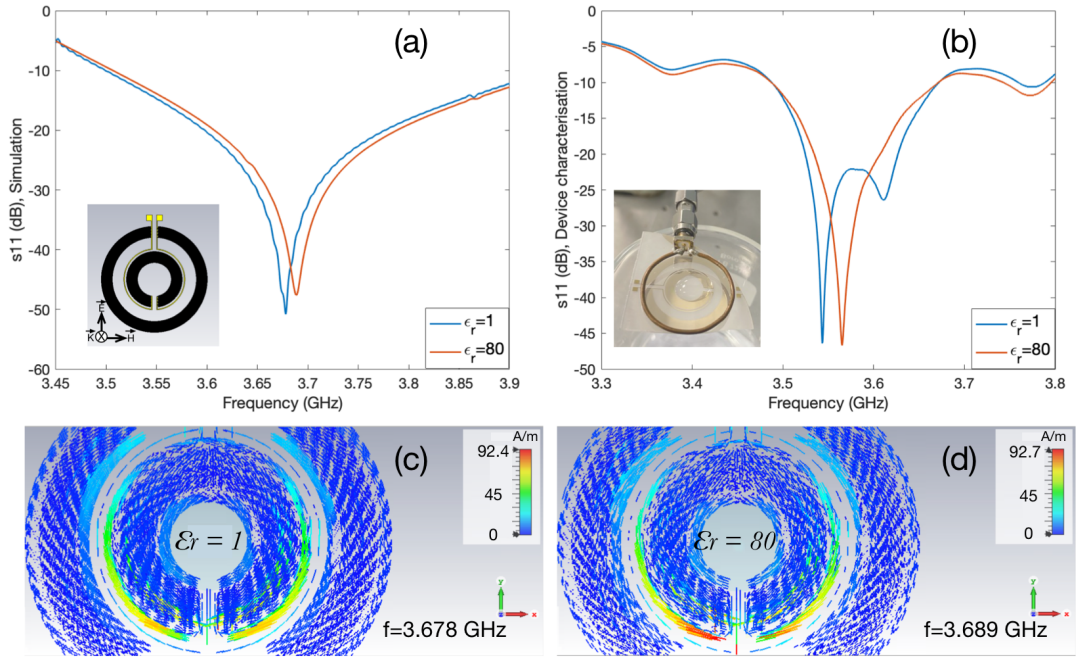


Figure 4.1: Simulation and experimental characterisation of the fabricated device. (a) Simulated reflection (S_{11}) spectrum of the device where magnetic field is along x-axis, electric field is along y-axis and propagation vector is perpendicular to the plane of the device when a water droplet is defined inside the inner circle with $\epsilon_r = 1$ (blue), and with $\epsilon_r = 80$ (red) (b) Measured S_{11} spectrum of the device in the absence ($\epsilon_r = 1$) and presence ($\epsilon_r = 80$) of $30\mu\text{L}$ of DI droplet. The simulated current density patterns are shown (c) at 3.678 GHz for $\epsilon_r = 1$, and (d) at 3.678 GHz for $\epsilon_r = 80$ [11].

4.2.3 Glucose Sensing

We investigated the sensing capability of the fabricated device by only altering the dielectric constant of the medium. For this purpose, we selected the inner circle area of the resonator for the location of droplets with different permittivity, the same as in the experimental characterisation measurements. As a case study, we prepared various glucose concentrations ranging from 0 to 250 mg/dL. Increasing the glucose concentration, decreases the relative permittivity [12], and therefore, reduces the effective capacitance. This translates to higher resonant frequency of the device for higher concentrations. We first captured the frequency of the device (f_0) without presence of any droplet. In the next step, we added a drop $30\mu\text{L}$ from each concentration ($f_{concentration}$) on the sensing area and noted the resonant frequency of the system. We calculated the difference in resonant frequency in each case per concentration with respect to the resonant frequency of the device in the absence of the droplet as below:

$$\Delta f = f_{concentration} - f_0 \quad (4.1)$$

We repeated the measurements for each concentration for at least five times to ensure the repeatability of the process. The average of Δf versus different concentrations of glucose is plotted in Figure 4.2, the error bars represent the standard deviation of the shift in frequency. The inset of the figure includes S_{11} spectra of the DI and several concentrations of glucose to demonstrate the shift in the frequency more clearly. Increasing the concentration of glucose led to a shift towards higher resonant frequencies as predicted. The sensitivity of the resonator for this location is 18 kHz/mg/dL, which is the slope of the plotted figure.

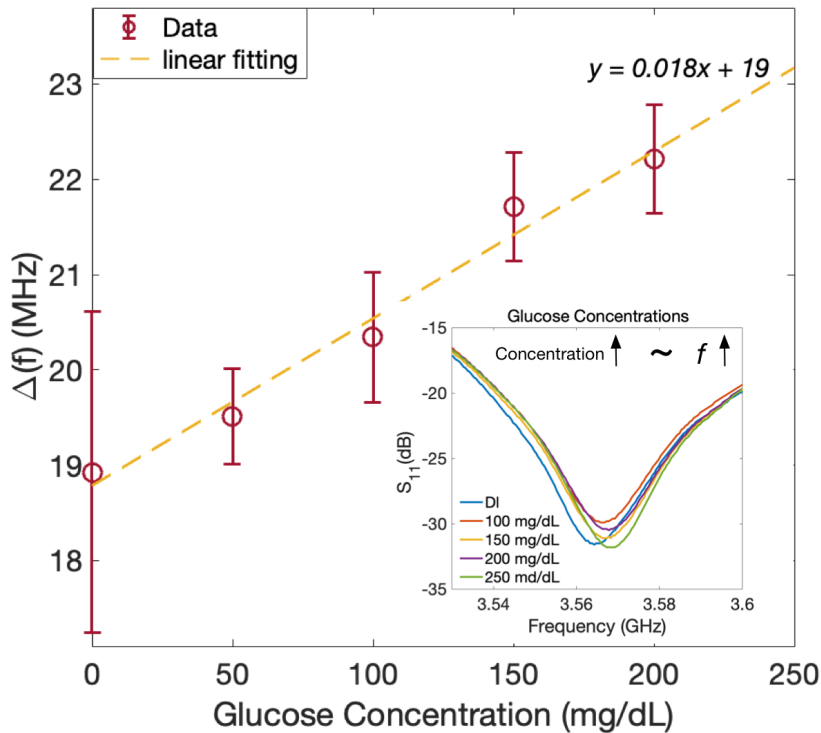


Figure 4.2: Effect of different glucose concentrations on the operational frequency of the device.

4.2.4 Dielectric Material Characterisation

In these set of experiments, we investigated the influence of various materials on the operating frequency of the resonator. We started the experiment by fixing the position of the device with regards to the loop antenna, where there is an apparent magnetic frequency with a high quality factor and then we recorded the data. As the simulation results can be a guidance towards selecting the most sensitive location of the electromagnetic frequency of the device, we referred back to simulation results to decide the most suitable location on the device for this round of our experiments. As can be seen from the simulation results in Figure 4.2(c-d), the current density is more prominent around the outer edges of the gap of the inner circular IDTs. Therefore, in order to investigate the effects of different substances on the resonant frequency of the device, we chose a container with the capacity of 2 mL, which covers the area around the gap when it is placed properly on the device. The picture of the setup is inserted as the inset in Figure 4.3(b). We first obtained the S_{11} characterisation of the device, when the container was empty. For the next steps, we used identical containers that were filled with 0.1 g of dried yeast, 0.1 g of glucose powder, glucose solution with concentration of 0.1 g/mL, and 1 mL of water. We repeated the experiment by placing each specific container on the exact position: the gap of the inner circular IDTs and recorded the data. The obtained results are plotted in Figure 4.3(a). The dielectric properties of the measured materials are summarised in Table 4.1. The frequency of the device, when there is no container placed on top of it, is 3.5 GHz. By utilising the glass container together with different materials, the dielectric constant of the area around the resonator is altered and increased compared to the case where there is no container. This results in a change in the effective capacitance of the sensor. Increasing the dielectric constant results in higher effective capacitance, and therefore, lower resonant frequency. Among the materials inside the container, air (empty glass container) has the lowest relative permittivity ($\epsilon_r = 1$) and water has the highest value ($\epsilon_r = 80$). The relative permittivity of dried yeast powder and glucose powder are 2 [13] and 3-4, [14] respectively and the relative permittivity of the glucose solution would be 76 [12], which is slightly lower than the DI water. Hence, it is expected that among these materials, water would have the lowest frequency, whereas the empty bottle would exhibit the highest frequency. Our results in Figure 4.3 (a) are in agreement with our expectations. We repeated the experiment for each container for at least five times to ensure the reliability and repeatability of the sensor. The shift of resonant frequency of each container with

respect to the resonance of the device is calculated and summarised in Figure 4.3(b). The points in the Figure 4.3(b) represent the average shift in resonant frequency of the device in the presence of an external substance for all the repeated experiments for each container. The error bars represent the standard deviation of obtained shift in frequency for each set of experiments per container. The average shifts of the resonance per container for empty bottle, dried yeast, glucose powder, glucose solution and water with respect to the operating frequency of the device are 9, 11.5, 11, 19.81, 22.31 MHz respectively towards lower frequencies.

$$\Delta f = f_{container} - f_0 \quad (4.2)$$

Where f_0 , is the reference frequency of the resonator without the presence of the container.

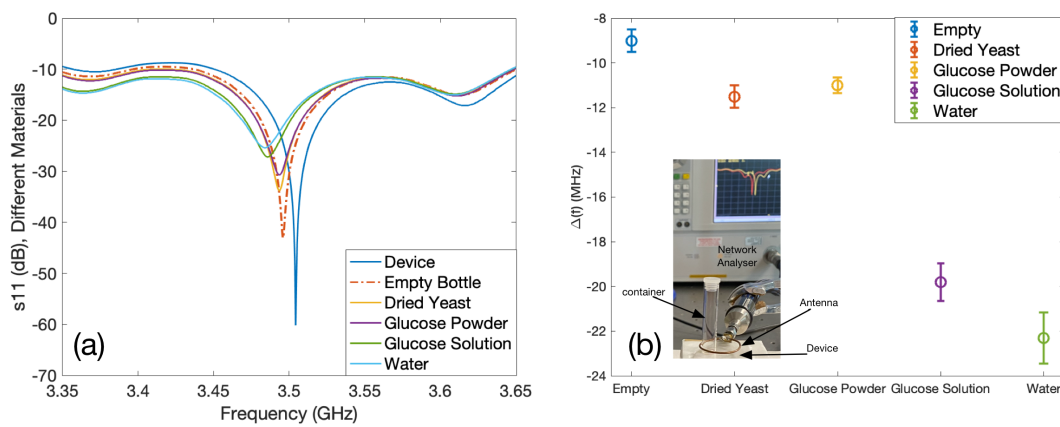


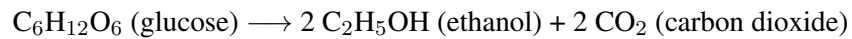
Figure 4.3: Effects of different materials inside the container on the frequency of the device. (a) S₁₁ spectra of the materials that were used in the experiment. (b) Measured shift in the resonant frequency with and without the container for different materials. Setup is shown in the inset.

Table 4.1: Material properties and the measured shift in the frequencies for different materials[11].

Material	Relative Permittivity	Average Resonant Frequency Shift (MHz)	Standard Deviation (MHz)
Water	80	-22.31	1.15
Glucose Solution	76	-19.81	0.84
Glucose Powder	3-4	-11	0.35
Dried Yeast	2	-11.5	0.5
Air	1	-9	0.5

4.2.5 Yeast Fermentation Process

In the next experiment in Figure 4.4, we monitored the fermentation process of the yeast. The fermentation is the natural process in which a micro-organism consumes carbohydrates such as glucose and produces alcohol or acid. The fermentation process is commonly used in producing alcoholic beverages as well as bread. The fermentation process of the yeast can be written as below [15]:



This is a metabolic reaction, in which yeast cells consume glucose to obtain energy, and ethanol and carbon dioxide are produced as by-products. Where the amount of oxygen is limited during the process, not enough ATP for yeast cells are produced and therefore, after some time, ethanol will accumulate and the fermentation will stop [15].

For our experiment, we prepared a solution of glucose with the concentration of 0.1 g/ml. In the next step, we added 0.1 g of dried yeast on top of the solution. Afterwards, we placed the container to the specified location in the previous experiment, covering the gap of the inner circular IDTs of the resonator for duration of 140 minutes and recorded the S_{11} spectra every 10 minutes. The S_{11} spectra are presented in Figure 4.4(b). A narrower range in x-axis of S_{11} spectra is also selected to illustrate the shift more clearly and is presented as an inset in Figure 4.4(b). After positioning the container, we noted the initial resonant frequency before the process as the reference frequency of the system. We observed that during this experiment, the resonant frequency was shifted towards lower frequencies and stabilized after about an hour. The results of the shift in frequency over time is plotted in Figure 4.4(a). During the monitoring time duration, the glucose concentration in the solution decreases, so relative permittivity increases around the sensor. At the same time, ethanol is produced which has higher relative permittivity compared to air and the same principle applies [16], [17]. The fermentation reaction leads to an increase in effective capacitance of the device and as a result, to a lower resonant frequency. Also, by accumulation of the ethanol over time, the fermentation will cease leading to stabilization of the resonant frequency.

A curve with a dash-line representation was fitted to the obtained data in Figure 4.4(a) using the Curve Fitting Tool in MATLAB, which effectively shows the occurring reaction during the fermentation process and follows the equation below:

$$y = 4.618e^{-0.02965x} - 3.533 \quad (4.3)$$

We also performed a control experiment, in which we repeated the same steps utilising a yeast-only solution. For the control experiment, we added 1 mL of water to 0.1 g of dried yeast and placed the container on the nominated location for 80 minutes. We noted the initial resonant frequency as the reference frequency of the system and we monitored the resonant frequency in every 10 minutes. We observed that during this time, the resonant frequency remained almost constant during these intervals. The measured shift in frequency is presented in Figure 4.4 (c) and the S_{11} spectra for several intervals are plotted in Figure 4.4 (d). The minor fluctuations in Figure 4.4 (c) is attributed to slight movements of yeast lumps in water.

The fermentation process is summarised in Figure 4.4 (a-b), the control experiments are illustrated in Figure 4.4(c-d) and the photos of the container used in fermentation reaction are presented in Figure 4.4 (e-g) over time from the beginning towards the end of the experiment respectively.

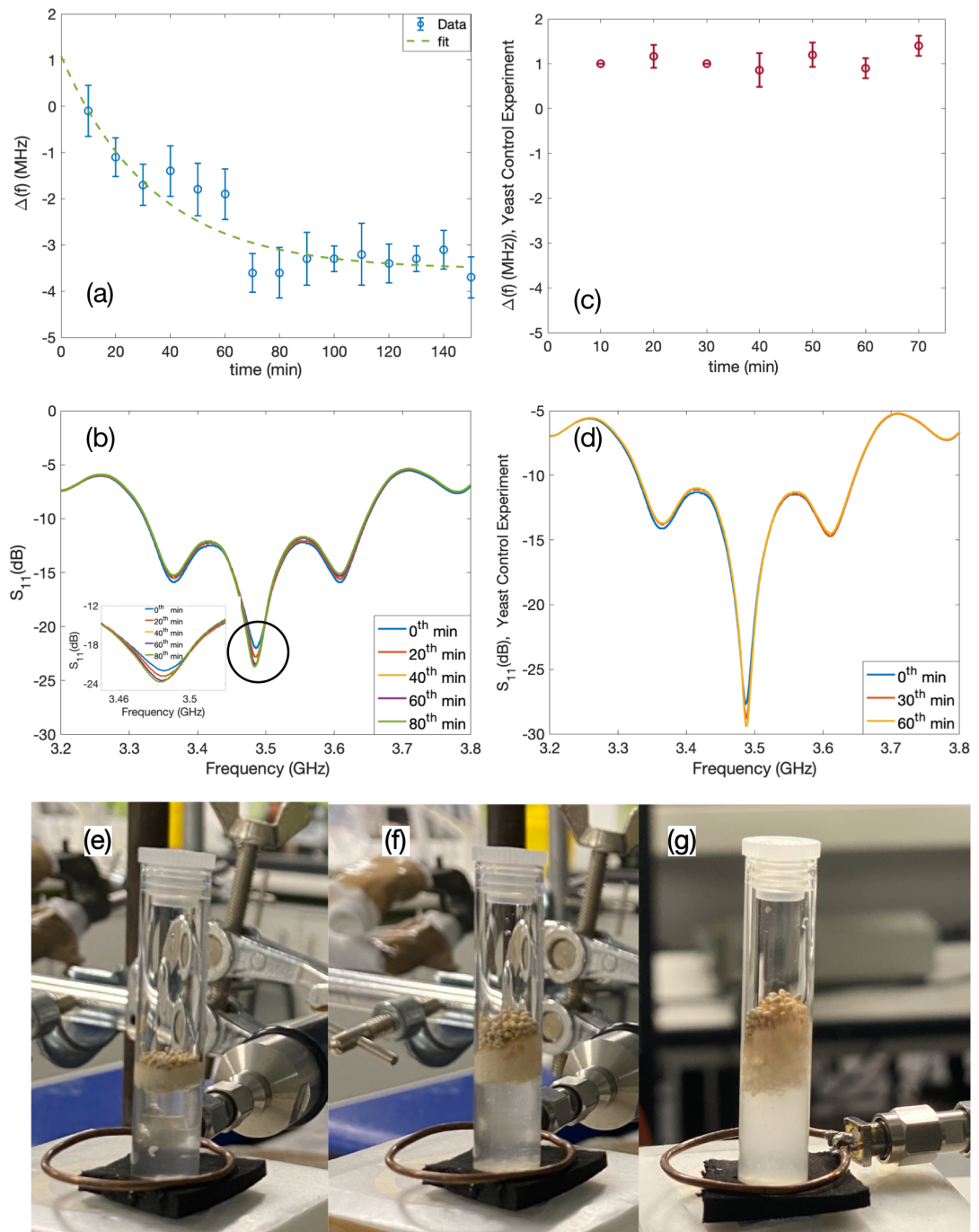


Figure 4.4: Yeast fermentation process and yeast control experiment. (a) measured shift in resonant frequency of the system over time. (b) S_{11} spectra of various intervals of time in fermentation process, including an inset representing a narrower range of frequency in reflection spectra of the system. (c) measured shift in resonant frequency of the control experiment (d) reflection spectra of different intervals of time for the control experiment. (e-g) the container used in fermentation process from beginning of the experiment towards the end respectively.

4.2.6 Acoustofluidic-based Characterisation

When RF power is applied to the IDT electrode pads at a certain frequency, surface acoustic waves (SAW) can be generated and utilised to manipulate micro droplets. The frequency of the structure for generating SAW depends on the period of the interdigitated transducers and also the speed of the acoustic wave in the piezoelectric substrate ($f = \nu/\lambda$). We characterized the device by measuring the reflection efficient from the port (S_{11}) of a network analyser in acoustic frequency range. We observed multiple peaks between the ranges of 5-30 MHz and the reason is that acoustic waves travel in various speeds along x, and y axes in LiNbO_3 piezoelectric substrate due to its anisotropic crystalline structure. The S_{11} characterisation of the device is demonstrated in Figure 4.5 in the frequency range of 5-30 MHz.

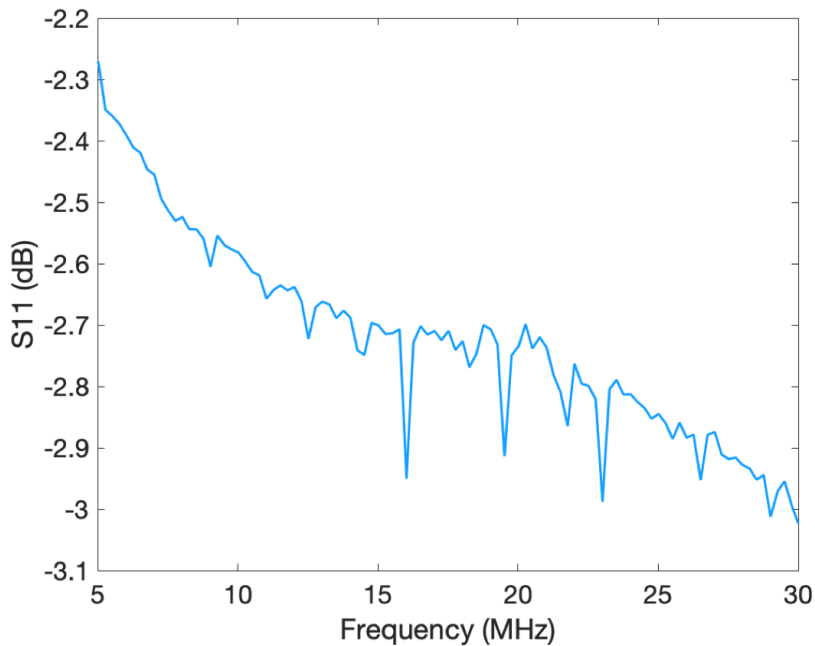


Figure 4.5: S_{11} characterisation of DSRR device within the range of 5-20MHz.

For actuation purposes, we used a signal generator to produce power at a certain frequency and we fed the output of the signal generator to an amplifier to intensify the signal. We connected the output of the amplifier to the electrode pads of the device to generate surface acoustic waves. The circular IDTs are used to intensify the traveling surface acoustic wave in the focal point of the actuator and can be efficiently utilised as mechanisms for microfluidic function such as streaming, jetting and nebulisation [3]–[5].

To demonstrate the streaming/mixing phenomenon, we diluted polystyrene microbeads with diameter of $10\ \mu\text{m}$ in DI water and utilised droplets of this solution to perform the experiment. Figure 4.6(a-f) depicts the top-view results of the mixing of polystyrene particles in a $10\ \mu\text{L}$ droplet of the prepared solution, and when a power of $\sim 0.5\ \text{W}$ is applied at $18\ \text{MHz}$ to the electrode pads of the IDTs from beginning towards the end of the experiments. We analyzed particle movements using a digital particle image velocimetry, PIVlab tool, in MATLAB [18].

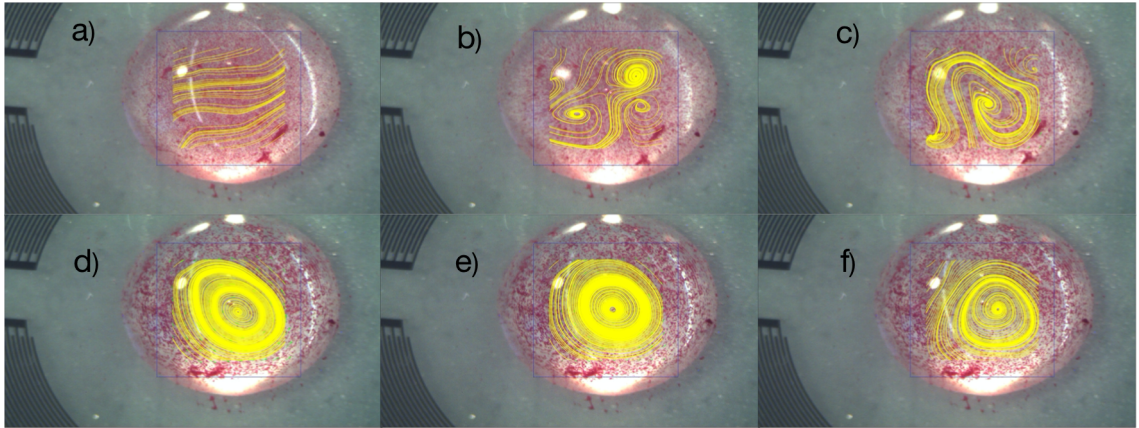


Figure 4.6: (a-f) Streaming patterns of polystyrene particles inside a $10\ \mu\text{L}$ droplet over time when the power applied to the electrode is $0.5\ \text{W}$ at the frequency of $18\ \text{MHz}$.

When the RF power is applied to the electrodes of a circular IDT device, generated surface acoustic waves, from various directions, travel towards and focus in the center. When the acoustic energy is accumulated in the center, circulation of the particles inside the droplet starts and momentum increases over time till the application of the power is ceased. This function can be effectively used for mixing particles with each other inside a droplet.

4.3 Conclusion

We designed and fabricated a device consisting of circular IDTs based on a dual split ring resonator geometry on LiNbO_3 substrates. We characterized the device for its sensing and acoustofluidic manipulation capabilities. For the sensing part, the centre location of the device was used to monitor glucose concentration in liquid droplets, and the location on the inner gap of the resonator was used to characterize different dielectric materials inside a glass container. We also presented a case study where the device was employed to monitor the yeast fermentation process. For acoustofluidic manipulation, the device was investigated for its capability in streaming. The obtained results

demonstrate that the structure has the potential to be employed and integrated in LoC and PoC applications.

In the next chapter, a conventional straight IDT design that is fabricated on a woven carbon fibre coated with polyimide and ZnO is proposed. The device's capability as a temperature control sensor for liquid droplets in its acoustic frequency is explored. Also, the response of the device to various intensities of UV exposure within this region is monitored. The sensing capability of the devices by placing a droplet with different concentration of glucose on a specific location on the device is demonstrated in microwave band.

References

- [1] H. Zhang, Y.-Q. Li, X. Chen, Y.-Q. Fu, and N.-C. Yuan, "Design of circular/dual-frequency linear polarization antennas based on the anisotropic complementary split ring resonator," *IEEE transactions on Antennas and Propagation*, vol. 57, no. 10, pp. 3352–3355, 2009, ISBN: 0018-926X Publisher: IEEE.
- [2] B. Sauviac, C. R. Simovski, and S. A. Tretyakov, "Double split-ring resonators: Analytical modeling and numerical simulations," *Electromagnetics*, vol. 24, no. 5, pp. 317–338, 2004, ISBN: 0272-6343 Publisher: Taylor & Francis.
- [3] S. Zahertar, Y. Wang, R. Tao, J. Xie, Y. Q. Fu, and H. Torun, "A fully integrated biosensing platform combining acoustofluidics and electromagnetic metamaterials," en, *Journal of Physics D: Applied Physics*, vol. 52, no. 48, p. 485 004, Sep. 2019, Publisher: IOP Publishing, ISSN: 0022-3727. DOI: 10.1088/1361-6463/ab3f7d. [Online]. Available: <https://doi.org/10.1088/1361-6463/ab3f7d> (visited on 01/15/2021).
- [4] M. K. Tan, J. R. Friend, and L. Y. Yeo, "Interfacial jetting phenomena induced by focused surface vibrations," *Physical Review Letters*, vol. 103, no. 2, p. 024 501, 2009, Publisher: APS.
- [5] R. Shilton, M. K. Tan, L. Y. Yeo, and J. R. Friend, "Particle concentration and mixing in microdrops driven by focused surface acoustic waves," *Journal of Applied Physics*, vol. 104, no. 1, p. 014 910, Jul. 2008, Publisher: American Institute of Physics, ISSN: 0021-8979. DOI: 10.1063/1.2951467. [Online]. Available: <https://aip.scitation.org/doi/10.1063/1.2951467> (visited on 01/15/2021).
- [6] S. Zahertar, A. D. Yalcinkaya, and H. Torun, "Rectangular split-ring resonators with single-split and two-splits under different excitations at microwave frequencies," *AIP Advances*, vol. 5, no. 11, p. 117 220, Nov. 2015, Publisher: American Institute of Physics. DOI: 10.

- 1063/1.4935910. [Online]. Available: <https://aip.scitation.org/doi/10.1063/1.4935910> (visited on 01/15/2021).
- [7] H. Torun, F. Cagri Top, G. Dundar, and A. D. Yalcinkaya, “An antenna-coupled splitting resonator for biosensing,” *Journal of Applied Physics*, vol. 116, no. 12, p. 124 701, Sep. 2014, Publisher: American Institute of Physics, ISSN: 0021-8979. DOI: 10.1063/1.4896261. [Online]. Available: <https://aip.scitation.org/doi/10.1063/1.4896261> (visited on 01/15/2021).
- [8] O. Sydoruk, E. Tatartschuk, E. Shamonina, and L. Solymar, “Analytical formulation for the resonant frequency of split rings,” *Journal of applied physics*, vol. 105, no. 1, p. 014 903, 2009, ISBN: 0021-8979 Publisher: American Institute of Physics.
- [9] R. C. Dorf, *The Electrical Engineering Handbook-Six Volume Set*. CRC press, 2018, ISBN: 1-4200-4975-5.
- [10] S. Zahertar, J. Wu, G. Chatzipirpiridis, *et al.*, “A Flexible PVDF-based Platform Combining Acoustofluidics and Electromagnetic Metamaterials,” in *2020 IEEE International Conference on Flexible and Printable Sensors and Systems (FLEPS)*, IEEE, 2020, pp. 1–4, ISBN: 1-72815-278-X.
- [11] S. Zahertar, H. Torun, R. Tao, *et al.*, “An integrated platform for metamaterial-based sensing and surface acoustic wave-based acoustofluidics utilising circular interdigital transducers,” *Sensors & Diagnostics*, vol. 1, no. 2, pp. 270–279, 2022.
- [12] V. Turgul and I. Kale, “Characterization of the complex permittivity of glucose/water solutions for noninvasive RF/Microwave blood glucose sensing,” in *2016 IEEE International Instrumentation and Measurement Technology Conference Proceedings*, May 2016, pp. 1–5. DOI: 10.1109/I2MTC.2016.7520546.
- [13] *List of dielectric constants*. [Online]. Available: https://www.vega.com/-/media/pdf-files/list_of_dielectric_constants_en.pdf (visited on 01/21/2021).
- [14] *Table of dielectric constants of substances — Level meters and level switches by Yamaden*. [Online]. Available: http://www.ydic.co.jp/english/technology/table_E.html (visited on 01/21/2021).
- [15] S. Maicas, *The role of yeasts in fermentation processes*. Multidisciplinary Digital Publishing Institute, 2020.

- [16] S. Zahertar, L. E. Dodd, and H. Torun, “Embroidered Rectangular Split-Ring Resonators for Material Characterisation,” in *2019 IEEE International Conference on Flexible and Printable Sensors and Systems (FLEPS)*, Jul. 2019, pp. 1–3. DOI: 10.1109/FLEPS.2019.8792233.
- [17] I. Smallwood, *Handbook of organic solvent properties*. Butterworth-Heinemann, 2012, ISBN: 0-08-052378-1.
- [18] W. Thielicke and E. Stamhuis, “PIVlab—towards user-friendly, affordable and accurate digital particle image velocimetry in MATLAB,” *Journal of open research software*, vol. 2, no. 1, 2014, ISBN: 2049-9647 Publisher: Ubiquity Press.

Chapter 5

Flexible and Integrated Sensing

Platform of Acoustic Waves and

Metamaterials based on

Polyimide-Coated Woven Carbon

Fibers

In this chapter, the integration concept is explored by fabricating straight IDTs on a thin zinc oxide film deposited on a carbon fiber substrate. The difference of this chapter is that the generated surface acoustic waves are utilised for controlling the temperature of a microfluid and also for sensing various UV intensities. The same device is used for characterising different concentrations of glucose solutions similar to previous chapters in microwave frequencies.

This chapter is based on a published manuscript in ACS Sensors¹.

¹Adapted with permission from Ran Tao^{A,D}, Shahrzad Zahertar^A, Hamdi Torun^A, Yi Ru Liu^B, Meng Wang^B, Yuchao Lu^C, Jing Ting Luo^D, Jethro Vernon^A, Richard Binns^A, Yang He^C, Kai Tao^C, Qiang Wu^A, Hong Long Chang^C, and Yong Qing Fu^A, “Flexible and Integrated Sensing Platform of Acoustic Waves and Metamaterials based on Polyimide-Coated Woven Carbon Fibers,” ACS sensors, vol. 5, no. 8, pp. 2563–2569, 2020. Copyright 2020 American Chemical Society.”

A Department of Mathematics, Physics and Electrical Engineering, Northumbria University, Newcastle upon Tyne, UK

B China-EU Institute for Clean and Renewable Energy, Huazhong University of Science and Technology, Wuhan 430074, P. R. China

C Key Laboratory of Micro and Nano Systems for Aerospace, Ministry of Education, Northwestern Polytechnical University, Xi’an 710072, P. R. China

D Shenzhen Key Laboratory of Advanced Thin Films and Applications, College of Physics and Optoelectronic Engineering, Shenzhen University, Shenzhen 518060, P. R. China

Abstract

Versatile, in situ sensing and continuous monitoring capabilities are critically needed, but challenging, for components made of solid woven carbon fibers in aerospace, electronics, and medical applications. In this work, we proposed a unique concept of integrated sensing technology on woven carbon fibers through integration of thin-film surface acoustic wave (SAW) technology and electromagnetic metamaterials, with capabilities of noninvasive, in situ, and continuous monitoring of environmental parameters and biomolecules wirelessly. First, we fabricated composite materials using a three-layer composite design, in which the woven carbon fiber cloth was first coated with a polyimide (PI) layer followed by a layer of ZnO film. Integrated SAW and metamaterials devices were then fabricated on this composite structure. The temperature of the functional area of the device could be controlled precisely using the SAW devices, which could provide a proper incubation environment for biosampling processes. As an ultraviolet light sensor, the SAW device could achieve a good sensitivity of 56.86 ppm/(mW/cm²). On the same integrated platform, an electromagnetic resonator based on the metamaterials was demonstrated to work as a glucose concentration monitor with a sensitivity of 0.34 MHz/(mg/dL).

5.1 Introduction

Solid woven carbon fibers are widely used in various fields such as aerospace [1] electronics [2], [3] and medical transducers[4], where low weight, high stiffness, and high conductivity are critically required. For these applications, in situ, versatile sensing and continuous monitoring capabilities are often required. For example, built-in sensors are often required for monitoring structural health of composite aircrafts made of woven carbon fibers [5] to detect crack generation and propagation in these structures [6]. However, currently few studies are focused on new types of applications using carbon fiber-based composites for various environmental applications such as temperature and ultraviolet (UV) light sensing or biological applications such as biomolecular and biochemical sensing. For these applications, a key challenge is to develop an integrated approach with the capabilities of efficient biosampling, liquid actuation, high-precision detection, and wireless operation/monitoring capabilities.

Surface acoustic wave (SAW) devices including those thin-film ones based on ZnO and AlN have

been extensively explored for a wide range of applications including gas sensing [7], [8] environmental sensing [9], [10] biomolecular detection [11], [12] microfluidics [13]–[15] acoustic tweezers [16], [17] and lab-on-a-chip [18], [19]. SAW sensors have the capability to be developed into a wireless operation platform, which can be realized by integrating antennas to the electrodes for signal transmission [20], [21]. Alternatively, a new approach of utilizing the same SAW structure as an electromagnetic resonator or metamaterials has been introduced recently [22]. This is based on defining an electromagnetic metamaterial-based resonator on the SAW device structure, which can be excited using external antennas [23]. It allows a new mode of sensing based on subwavelength-sized structures defined by the SAW geometries that are usually made of metals on dielectric substrates, and the changes of electromagnetic resonant frequencies of this structure can be applied to monitor parameters of interest for sensing applications [22]. Using this new design, the operation using metamaterials can be utilized in addition to the conventional operation of SAWs for sensing or acoustofluidics, where the interdigitated transducers (IDTs) are powered directly and remotely.

In this study, we explored a new concept of integrated sensing technology on woven carbon fibers through the integration of electromagnetic metamaterials and thin-film acoustic wave sensors, with capabilities of noninvasive, in situ, and continuous monitoring of environmental parameters and biomolecules wirelessly. It is well known that the woven structure of carbon fibers poses challenges to define efficient SAW and electromagnetic resonators due to its highly flexible, extremely porous, and rough surface, which causes significant difficulties in coating uniform piezoelectric layers such as ZnO. In addition to mechanical imperfections, the porosity and flexibility of the woven structure could lead to significant damping and reduction of quality factor for both the SAW and metamaterials devices[24]. We addressed this challenge by fabricating composite materials using a three-layer composite design. The carbon fiber was first coated with a polyimide (PI) layer, and then a ZnO film was deposited onto this PI/carbon fiber structure. We then fabricated SAW and metamaterials devices on this composite material using a conventional photolithography method and optimized the electrodes of the designs for integrated functions including liquid temperature control, UV sensing, and glucose monitoring as case studies for different applications.

5.2 Experimental Section

A ZnO thin film ($5 \mu\text{m}$ thick) was deposited on the PI-coated carbon fiber substrate using a DC magnetron sputter with the sputtering power of 400 W, Ar/O₂ gas flow rate of 10/15 sccm, and chamber pressure of 4×10^{-4} mbar. A zinc target with 99.99% purity was used, while the sample holder was rotated during the deposition to achieve the uniformity of the film thickness. The IDTs were patterned using the conventional photolithography and lift-off process, where Cr/Au films with thicknesses of 10 nm/120 nm were selected as the electrode materials and deposited using a thermal evaporator (EDWARDS AUTO306).

The crystal orientation and surface roughness of the sputtered ZnO thin film were characterized using X-ray diffraction (XRD, SIEMENS D5000) and atomic force microscopy (AFM, Veeco Dimension 3100), respectively. The reflection and transmission spectra of the integrated platform were acquired continuously during the UV- and glucose-sensing experiments using a high-frequency network analyzer (Agilent N5230A) with a LabVIEW data acquisition program. The SAW devices were acoustically excited using a signal generator and a power amplifier while the temperature of the droplet placed on top of the device was recorded using an infrared camera.

The finite element analysis (FEA) simulation of SAWs in this work was performed using the COMSOL software with solid mechanics and electrostatics modules. A two-dimensional (2D) model with a simplified SAW structure was used comprising the carbon fiber layer, PI layer, ZnO thin film, and IDT fingers from bottom to top, with thicknesses of $600 \mu\text{m}$, $150 \mu\text{m}$, $5 \mu\text{m}$, and 130 nm, respectively. The width of the model was defined by the wavelengths of the SAW devices, varying from 64 to $160 \mu\text{m}$. The wave modes and reflection spectra S_{11} of SAWs were obtained from the simulation results, with periodic boundary conditions.

The electromagnetic behavior of the coupled device with a wavelength of $64 \mu\text{m}$ was studied using a commercially available simulator (CST Studio Suite, Darmstadt, Germany). The computational environment was created based on the geometry, and the waveguide ports were defined to obtain scattering parameters. The mesh sizes were refined considering the convergence of the simulations. Plane wave excitations were used during the simulations.

5.3 Results and Discussion

Design and Characterization of the Integrated Platform

The design of SAW devices relies on the definition of the IDTs so that the device supports specified acoustic wave modes. Rayleigh waves are generated when the IDTs are excited electrically at their resonant frequencies, which are determined by the velocity of sound on the composite structure and the wavelength of the IDT: e.g., $f_0 = \nu/\lambda$, where ν is the acoustic phase velocity and λ is the designed wavelength. Since the phase velocity of piezoelectric materials is altered by different factors, the resonant frequency of the SAW devices can be monitored to track these changes, based on Equation 2.7 [25].

Meanwhile, this structure of a single-metallic layer on a dielectric substrate is also an ideal platform to realize a metamaterial-based electromagnetic resonator at microwave frequencies. The structure supports circulating currents along the metallic layer when the device is excited appropriately. For example, when the magnetic field is perpendicular to the device, a circulating current path is generated due to the induced current on the metallic layer as shown in Figure 5.1(a).

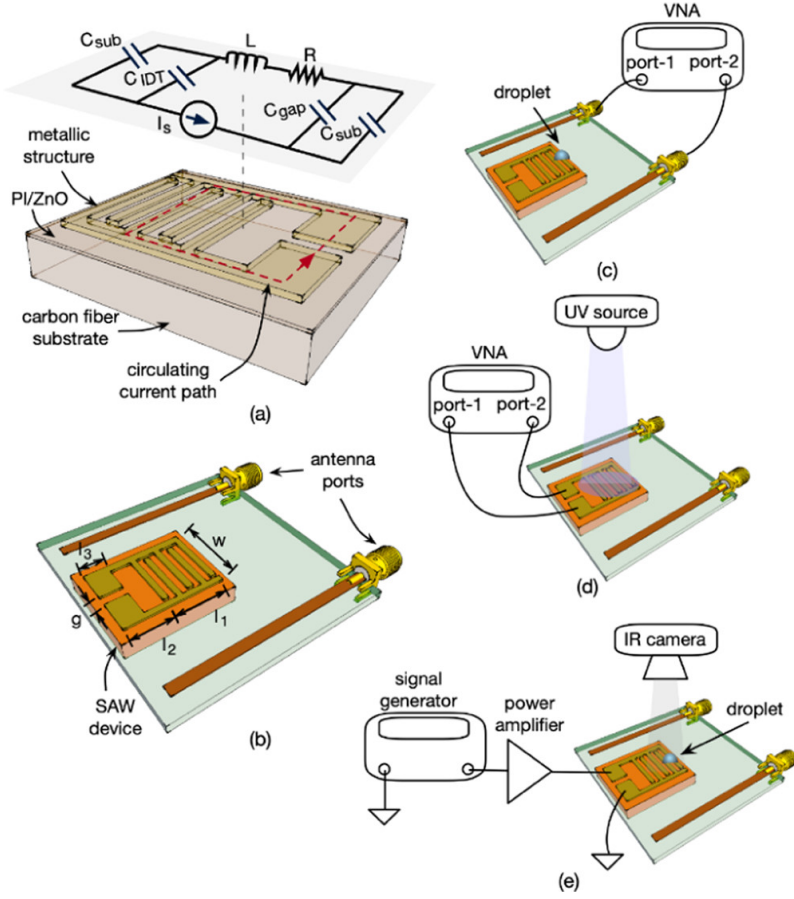


Figure 5.1: (a) Schematic illustration of the integrated platform combining surface acoustic waves and metamaterials with the equivalent circuit of the device at resonance. (b) Schematic illustration of the integrated platform. Schematic illustrations of the experimental setups for (c) glucose sensing, (d) UV sensing, and (e) temperature control [26].

The induced current can be supported at a specific resonant frequency determined by the geometry of the structure; therefore, its resonant frequency depends on the electrical characteristics imposed by the device geometry. Along the path, the equivalent circuit components can be simplified using lumped elements as labeled in Figure 5.1(a). The resonant frequency and the quality factor of the device can be expressed using Equations 5.1 and 5.2 [27].

$$f_0 = \frac{1}{2\pi\sqrt{LC_{eff}}} \quad (5.1)$$

$$Q = \frac{1}{R}\sqrt{\frac{L}{C_{eff}}} \quad (5.2)$$

where L is the inductance of the structure, R is the equivalent resistance of the structure, and

C_{eff} is the effective capacitance of the structure. The effective capacitance is determined by the combination of the capacitive elements along the current path including those of the IDTs, gap, and substrate surface. Therefore, any changes in the effective inductance and the capacitance of the structure will alter the resonant frequency of the device. We designed this type of metamaterial device, which is sensitive to the changes in relative permittivity of its substrate and of a sample placed within its vicinity. The changes in the relative permittivity of the device or the sample result in a change in the effective capacitance, thus altering the resonant frequency of the device. The resonant frequency of the device can be simply measured using a pair of monopole patch antennas as shown in Figure 5.1(b).

In this configuration, the sensing structure is electrically passive and electromagnetically coupled to the readout antennas. This eliminates the need for active electronics and power transfer on the sensing structure; therefore, the sensor can be realized in a smaller footprint and consumes negligible power on itself. In comparison, conventional wireless sensing architectures are based on electrically active sensors that are powered using inductively coupled coils [28], [29].

To integrate SAW and metamaterials devices on the woven carbon fiber surfaces, we created a trilayer structure, as shown in Figure 5.1(a). The commercially available woven carbon fiber layer with a thickness of ~ 1 mm was coated with a layer of $150 \mu\text{m}$ thick polyimide (PI) to create a relatively smooth surface for the subsequent processes. Then, a ZnO film layer with a thickness of $\sim 5 \mu\text{m}$ was deposited using a DC magnetron sputter. The metallic layer was then patterned on top of the ZnO layer to form the IDTs using a standard lift-off process. The IDTs were made of 20/120 nm thick Cr/Au layers evaporated on the surface. We fabricated devices with different IDT wavelengths of 64, 100, and $160 \mu\text{m}$, where the width, length, and gap of the pattern (see Figure 1b) are $w = 9$ mm, $l_1 = 5.6$ mm, $l_2 = 6.2$ mm, $l_3 = 4$ mm, and $g = 3.2$ mm.

Figure 5.2(a) shows the XRD pattern of the fabricated tri-layer composite material. There is a dominant peak at $2\theta = 34^\circ$, suggesting that the ZnO film is composed of polycrystalline phases with a strong texture along the c-axis (e.g., with strong (0002) orientation). The topographic image of the ZnO film over an area of $10 \times 10 \mu\text{m}^2$ obtained using the AFM reveals that its surface roughness is ~ 38.6 nm (see Figure 5.2(b)).

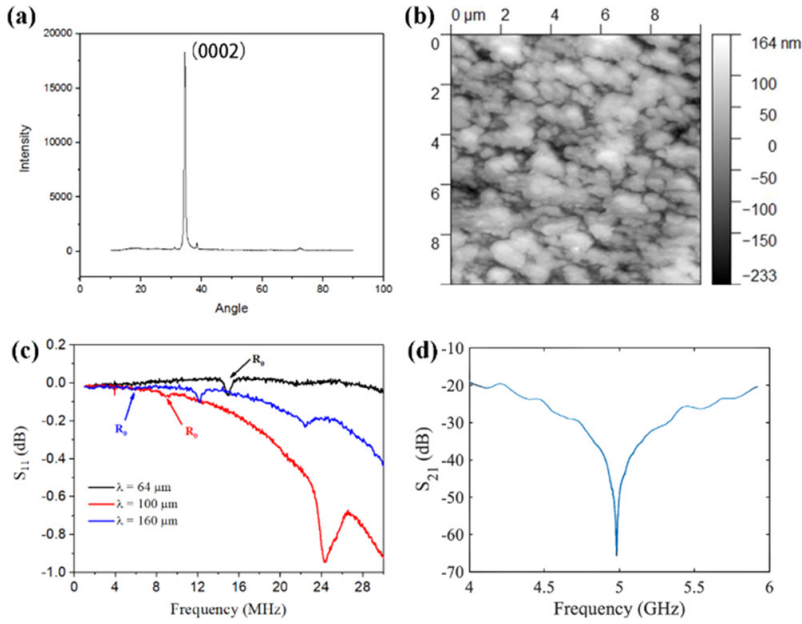


Figure 5.2: (a) XRD patterns of the ZnO/PI/carbon fiber tri-layer structure. (b) AFM image of the ZnO thin film. (c) Reflection spectra S_{11} of SAWs with the designed wavelengths of 64, 100, and 160 μm . (d) Transmission spectrum S_{21} of the electromagnetic resonator of the SAW device with a wavelength of 64 μm [26].

The reflection spectra S_{11} of SAW devices were measured using a vector network analyzer connected to their electrodes, and the results are shown in Figure 5.2(c). The obtained frequencies of the Rayleigh wave (R_0) modes are decreased from 14.95 to 5.92 MHz with the wavelength increased from 64 to 160 μm . On the other hand, the electromagnetic resonance of the devices with a wavelength of 64 μm was also characterized, and the results of transmission spectra S_{21} are shown in Figure 5.2(d). The electromagnetic resonant frequency was measured as 4.98 GHz. In this design, the wavelength of the IDT does not alter the resonant frequency as the C_{eff} parameter of Equation 5.2 is dominated by the surface capacitance of the structure.

Acoustic Wave Modes and Electromagnetic Fields

FEA methods were used to investigate the Rayleigh wave modes and reflection spectra of SAW devices based on ZnO/PI/carbon fibers. Figure 5.3(a) displays the surface vibration modes of Rayleigh waves with wavelength of 64 and 160 μm . Since the Young's modulus of the carbon fiber (97-228 GPa)[30] is much larger than that of PI (~ 2.5 GPa), the acoustic wave-induced mechanical energy is largely confined within the ZnO/PI structure. As the wavelength is increased and becomes comparable to the thickness of the trilayer structure, more energy becomes dissi-

pated into the carbon fiber substrate as shown in Figure 5.3(a). Simulation results present a similar changing trend of R_0 frequency with increasing wavelength to those obtained from the experiments (Figure 5.3(b)). There is a minor divergence between experimental and simulation results (comparing the results shown in Figures 5.2(b) and 5.3(b)), which could be explained by the following reasons: (a) the chosen material parameters were obtained from those reported in the literature [31]–[33] (b) periodic boundary conditions were applied during the simulation, and (c) only one pair of IDT fingers were chosen during the simulation.

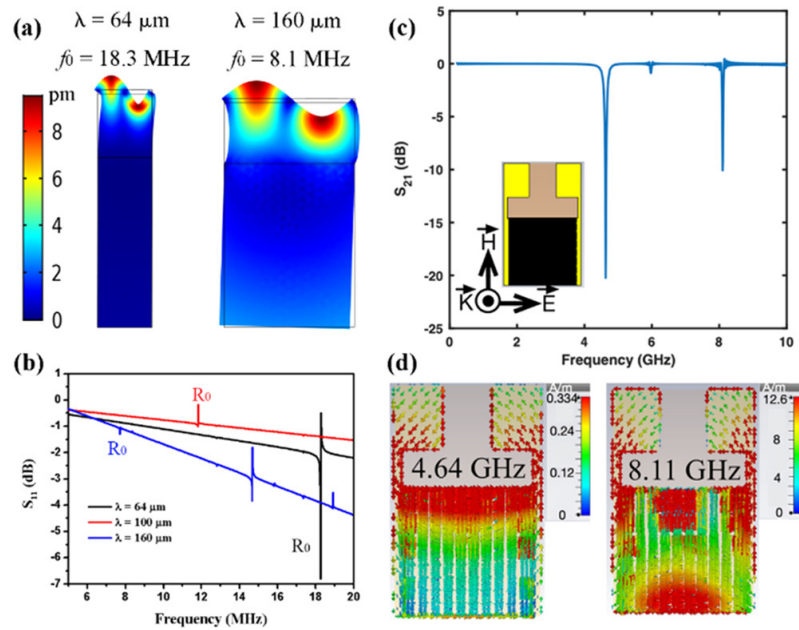


Figure 5.3: FEA simulation of vibration modes of SAW devices based on the ZnO/PI/carbon fiber structure: (a) Rayleigh wave modes with $\lambda = 64 \mu\text{m}$ and $\lambda = 160 \mu\text{m}$ and (b) reflection spectra S_{11} of devices with $\lambda = 64, 10, \text{ and } 160 \mu\text{m}$. Simulated patterns of (c) S_{21} spectrum of the electromagnetic resonator (the corresponding coupled SAW has a wavelength of $64 \mu\text{m}$) and (d) profile of surface current density at the resonance (the corresponding coupled SAW has a wavelength of $64 \mu\text{m}$) [26].

We also simulated the electromagnetic behavior of the device with a wavelength of $64 \mu\text{m}$ using a commercially available simulator. Figure 5.3(c) shows the transmission spectrum S_{21} of the device within a frequency range of 1-10 GHz, where the sharp dips at 4.6 and 8.1 GHz indicate two resonance modes. Here, the electric field is along the electrodes inducing electric polarization on the opposite bonding pads, which results in a circulating current pattern at 4.6 GHz as shown in Figure 5.3(d). The electromagnetic signal is dissipated in the device at this frequency due to the induced current. A higher order resonance at 8.1 GHz results in a different pattern of circulating current as shown in Figure 5.3(d). However, the resonance at 4.6 GHz is stronger than that at 8.1

GHz as the dip magnitude of the resonance is larger as observed in Figure 5.3(c). Thus, we used this 4.6 GHz resonance for the metamaterial sensing work.

5.3.1 Demonstration of Liquid Temperature Control using the Integrated Platform

Precise temperature control of droplets is often desired for biosensors and bioreactors requiring biomolecular functionalization[34]. The SAW devices can be used to increase and maintain the temperature of the liquid samples placed in the functional region of the sensor above the environmental temperature. The temperature rise in the liquid mainly results from an acousto-thermal heating phenomenon[35], depending on the input energy density of the acoustic waves and the energy dissipation into the liquid (mainly determined by the intrinsic properties of the liquid and its volume). Compared to the Al foil substrate, which we previously reported for use in the flexible SAW devices[36], the woven carbon fiber cloth substrate (which is polymer matrix based) has a relatively lower thermal conductivity on the order of $1\text{-}10\text{ W/m}\cdot\text{K}$ [37]. Together with the PI film between the ZnO layer and the carbon fiber substrate having an even smaller thermal conductivity of $0.12\text{ W/m}\cdot\text{K}$, most of the acoustic heat has been confined on the surface of the SAW device.

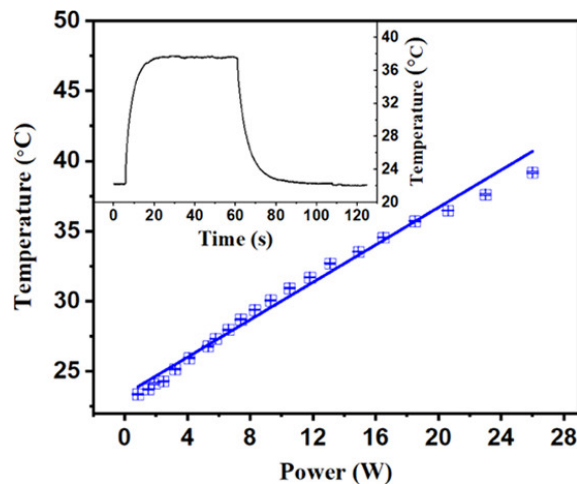


Figure 5.4: Measured average temperatures of a $5\ \mu\text{L}$ distilled water droplet on top of the SAW device with increasing input power. The inset shows that the average temperature is controlled by the input power (23 W) over time [26].

We used the setup schematically shown in Figure 5.1(e) to measure the temperature of a droplet while the SAW device was activated. As a proof-of-concept demonstration, Figure 5.4 shows the

average temperature of a 5 μL distilled water droplet on top of the SAW device with a wavelength of 160 μm controlled by the input SAW power. The obtained temperature readings are changed according to the following relationship with the applied power: $T = 23.34$ ($^{\circ}\text{C}$) + $0.67 P$ (W), in which T is the droplet temperature and P is the input power applied to the IDTs at 12.33 MHz (Sezawa mode wave). The inset of Figure 5.4 displays an example of a heating cycle. The temperature was increased immediately after the power was applied, taking ~ 10 s to reach the set value of 37.5 $^{\circ}\text{C}$. Then, it was maintained at the set temperature for 1 min with a minor fluctuation of 0.1 $^{\circ}\text{C}$. Clearly, SAW devices can be used to precisely control the liquid temperature, which can meet the requirements of biological processes.

Multiple Sensing Functions Based on the Integrated Platform

5.3.2 UV Sensing using SAW

The SAW device with a wavelength of 64 μm was used for demonstration of sensing functions such as UV sensing. We used the setup schematically shown in Figure 5.1(d) to measure the shift in resonant frequency of the SAW device under the UV exposure. As shown in Figure 5.5(a), the device was exposed to the UV light with different controlled intensities (from 0 mW/cm^2 to 151.2 mW/cm^2) at durations of 20-40 s and then kept in the dark environment for another 20 s until the external UV irradiation influence disappeared, while the resonant frequency shift was continuously recorded for the whole process. As the device was exposed to the UV light, the frequency shift of the R_0 mode was increased linearly for the first 10-15 s and then saturated at the corresponding intensity values until UV light was switched off. Afterward, the frequency shift was decreased to zero as the device recovered to the equilibrium state. Figure 5.5(b) shows that there is a linear relationship between the frequency shift and UV intensity, which produces an estimated sensitivity of 0.85 $\text{kHz}/(\text{mW}/\text{cm}^2)$. Considering that the initial frequency is 14.95 MHz, the sensitivity can also be written as 56.86 $\text{ppm}/(\text{mW}/\text{cm}^2)$.

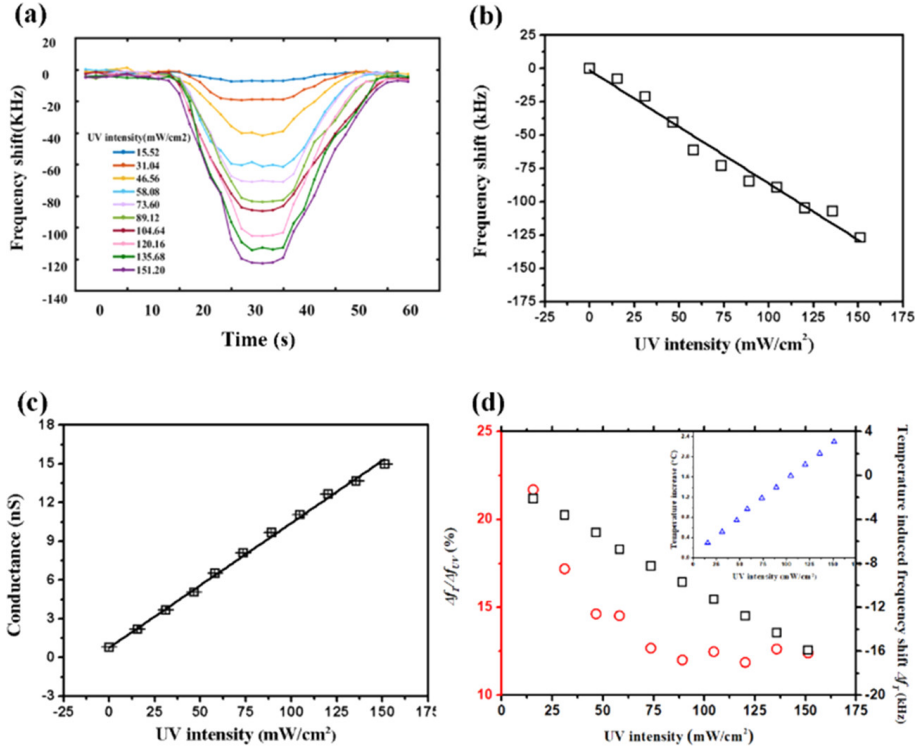


Figure 5.5: (a) Real-time frequency shift of the SAW UV sensor with a wavelength of $64 \mu m$ under UV light. (b) Total frequency shift varying with the UV intensity. (c) Sheet conductance varying with the UV intensity. (d) Temperature-change-induced frequency shift Δf_T and the ratio between Δf_T and the total shift varying with the UV intensity. The inset shows the temperature increase with the UV intensity [26].

According to Equation 2.7, the frequency shift caused by the UV light is mainly composed of two parts: i.e., (a) from the conductivity change of ZnO thin films; and (b) from the increase of the temperature. For the frequency shift due to the changes of conductivity, the following equation is generally applied [38], [39].

$$\frac{\Delta f}{f_0} = \frac{\Delta \nu}{\nu_0} = -\frac{k^2}{2} \frac{1}{1 + (\nu_0 C_s / \sigma_s)} \quad (5.3)$$

where k^2 is the coupling coefficient, C_s is the capacitance per unit length of the surface, and σ_s the sheet conductivity. By measuring the current-voltage ($I - V$) curves of the device under different intensities of the UV illumination, the obtained sheet conductance G_s is shown in Figure 5.5(c), and the readings increase with the UV intensity. As σ_s is proportional to G_s , the sheet conductivity is also increased with the UV intensity, thus contributing to the increase of the total frequency shift.

However, thermal heating effect can also be generated in the device during the UV illumination due to the actuation of SAW and the low thermal conductivity of the PI-coated carbon fiber composites. This will surely change the shift of the frequency. We have also measured the temperature of the device as a function of UV exposure duration. The surface temperature rise was 0.3-2.3 K during the 20 s exposure at different UV intensities (Figure 5.5(d)). To evaluate the temperature-induced frequency shift, the temperature coefficient of frequency (TCF) of the same SAW device was measured and calculated, and the obtained reading was 465 ppm/K (with the initial frequency $f_0 = 14.95$ MHz). The frequency shift Δf_T can be calculated using the following equation

$$\Delta f_T = f_0 \Delta T \text{ TCF} \quad (5.4)$$

where ΔT is the change of temperature. Therefore, the temperature-induced frequency shift was estimated to be -2 to -16 kHz, which contributes to less than 25% of the total frequency shift as shown in Figure 5.5(d). Besides, this fraction was decreased as the UV intensity was increased and saturated at 12%. In addition to temperature, humidity as another key environmental parameter can also affect the UV-sensing performance of SAW sensors. We have previously explored this effect for Al-foil-based flexible SAW sensors and explained how the measurements can be decoupled [38].

Our experimental results showed that the SAW resonant frequency can be used for UV sensing and indicated the conductivity change of the ZnO thin film is dominant in the physical mechanism.

5.3.3 Glucose Concentration Monitoring using the Electromagnetic Resonator

The same SAW device (with the wavelength of $64 \mu m$) was further used as the metamaterial device to measure glucose concentrations in a droplet of deionized water with a volume of $0.5 \mu L$ placed directly on top of the IDTs (see Figure 5.1(c) for the schematics of the experimental setup). We kept the droplet at the exactly same location on the device with a position error of less than 0.2 mm using the IDT itself as the marker under the video camera. We then varied the concentrations of glucose within a range of 10-500 mg/dL and also washed the surface with deionized water between each measurement to clean the residues. Figure 5.6(a) shows an exemplary set

of recorded S_{21} spectra at different glucose concentrations. We repeated each measurement at a particular glucose concentration for 10 times and repeated the measurement protocol on three different days. Figure 5.6(b) shows the variation of the resonant frequency with the concentration of glucose, where the error bars represent the standard error of the mean values. The resonant frequency of the metamaterial device increases with the concentration of glucose. This is expected since the permittivity of a droplet of glucose solution decreases with increased concentration of glucose[22]. We observed a linear decrease in resonant frequency within the measurement range with a sensitivity of 0.34 MHz/(mg/dL). This level allows measurement of glucose with a resolution of 3 $\mu\text{g/dL}$ with a frequency resolution of 1 kHz at the measurement band.

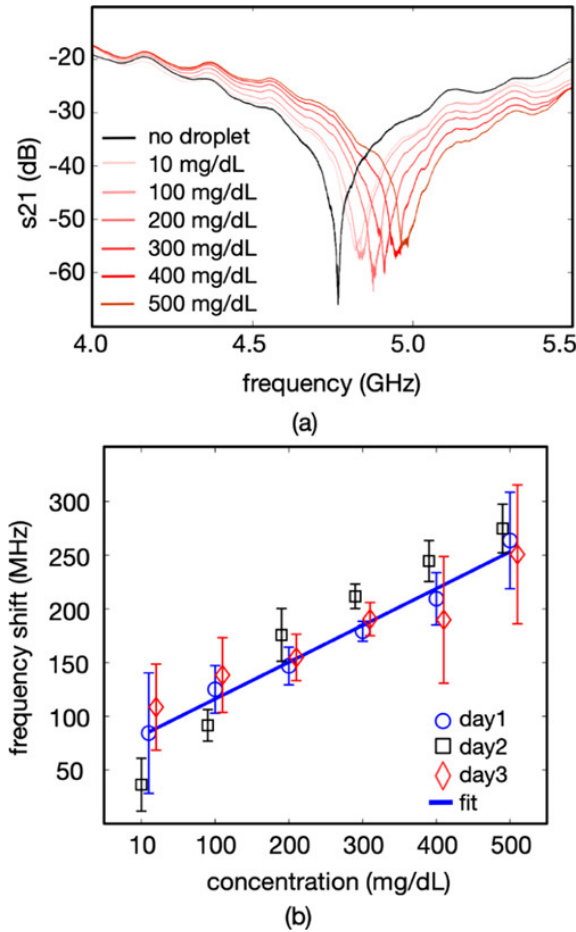


Figure 5.6: (a) S_{21} spectra of the device with droplets with varying concentrations of glucose and (b) frequency shift of the device with glucose concentration, measured on three different days. The concentration values for each day were the same at 10, 100, 200, 300, 400, and 500 mg/dL. The markers in the figures are shifted slightly in the horizontal direction for better readability [26].

5.4 Conclusions

A flexible and integrated platform of acoustic waves and electromagnetic metamaterials based on polyimide-coated woven carbon fibres was proposed in this work for potential application in bioassays and multifunction sensing. The designed platform was based on a SAW device, where the acoustic wave was agitated to control the temperature of a liquid droplet placed in the functional area and was also used as a UV sensor with the sensitivity of 56.86 ppm/(mW/cm²).

Meanwhile, the same device presented excellent performance in glucose concentration monitoring when it worked as an electromagnetic metamaterial device, giving a sensitivity of 0.34 MHz/(mg/dL). Our integrated platform has shown its capability for versatile sensing functions in a liquid environment as well as the capability to simulate the biological incubating conditions.

In the next chapter, PVDF is used a piezoelectric flexible substrate with straight IDTs patterned on top of it using laser milling. The device is investigated for its electromagnetic behaviour under different excitation conditions through simulations and possible resonant frequencies in microwave regime are identified. Next, the device is characterised with a network analyser to obtain its electromagnetic and acoustic response. The acoustic response is further investigated by placing the fabricated device on a bare lithium niobate substrate.

References

- [1] P. Chowdhury, H. Sehitoglu, and R. Rateick, “Damage tolerance of carbon-carbon composites in aerospace application,” en, *Carbon*, vol. 126, pp. 382–393, Jan. 2018, ISSN: 0008-6223. DOI: 10.1016/j.carbon.2017.10.019. [Online]. Available: <http://www.sciencedirect.com/science/article/pii/S0008622317310126> (visited on 01/15/2021).
- [2] A. B. Dalton, S. Collins, E. Muñoz, *et al.*, “Super-tough carbon-nanotube fibres,” en, *Nature*, vol. 423, no. 6941, pp. 703–703, Jun. 2003, Number: 6941 Publisher: Nature Publishing Group, ISSN: 1476-4687. DOI: 10.1038/423703a. [Online]. Available: <https://www.nature.com/articles/423703a> (visited on 01/15/2021).
- [3] K. Jost, D. Stenger, C. R. Perez, *et al.*, “Knitted and screen printed carbon-fiber supercapacitors for applications in wearable electronics,” en, *Energy & Environmental Science*, vol. 6, no. 9, pp. 2698–2705, Aug. 2013, Publisher: The Royal Society of Chemistry, ISSN: 1754-5706. DOI: 10.1039/C3EE40515J. [Online]. Available: <https://pubs.rsc.org/en/content/articlelanding/2013/ee/c3ee40515j> (visited on 01/15/2021).
- [4] T. Kondo, “Carbon-Fiber Composite Materials for Medical Transducers,” en, in *Piezoelectric and Acoustic Materials for Transducer Applications*, A. Safari and E. K. Akdoğan, Eds., Boston, MA: Springer US, 2008, pp. 179–188, ISBN: 978-0-387-76540-2. DOI: 10.1007/978-0-387-76540-2_9. [Online]. Available: https://doi.org/10.1007/978-0-387-76540-2_9 (visited on 01/15/2021).
- [5] Z. Su, X. Wang, Z. Chen, L. Ye, and D. Wang, “A built-in active sensor network for health monitoring of composite structures,” *Smart Materials and Structures*, vol. 15, p. 1939, Nov. 2006. DOI: 10.1088/0964-1726/15/6/050.
- [6] H. Kim, “Enhanced crack detection sensitivity of carbon fiber composites by carbon nanotubes directly grown on carbon fibers,” en, *Composites Part B: Engineering*, vol. 60,

- pp. 284–291, Apr. 2014, ISSN: 1359-8368. DOI: 10.1016/j.compositesb.2013.12.063. [Online]. Available: <http://www.sciencedirect.com/science/article/pii/S1359836813007932> (visited on 01/15/2021).
- [7] D.-T. Phan and G.-S. Chung, “Surface acoustic wave hydrogen sensors based on ZnO nanoparticles incorporated with a Pt catalyst,” en, *Sensors and Actuators B: Chemical*, vol. 161, no. 1, pp. 341–348, Jan. 2012, ISSN: 0925-4005. DOI: 10.1016/j.snb.2011.10.042. [Online]. Available: <http://www.sciencedirect.com/science/article/pii/S0925400511009348> (visited on 01/15/2021).
- [8] V. B. Raj, H. Singh, A. T. Nimal, M. U. Sharma, M. Tomar, and V. Gupta, “Distinct detection of liquor ammonia by ZnO/SAW sensor: Study of complete sensing mechanism,” en, *Sensors and Actuators B: Chemical*, vol. 238, pp. 83–90, Jan. 2017, ISSN: 0925-4005. DOI: 10.1016/j.snb.2016.07.040. [Online]. Available: <http://www.sciencedirect.com/science/article/pii/S0925400516310759> (visited on 01/15/2021).
- [9] R. Tao, S. A. Hasan, H. Z. Wang, *et al.*, “Bimorph material/structure designs for high sensitivity flexible surface acoustic wave temperature sensors,” en, *Scientific Reports*, vol. 8, no. 1, p. 9052, Jun. 2018, Number: 1 Publisher: Nature Publishing Group, ISSN: 2045-2322. DOI: 10.1038/s41598-018-27324-1. [Online]. Available: <https://www.nature.com/articles/s41598-018-27324-1> (visited on 01/15/2021).
- [10] H.-S. Hong and G.-S. Chung, “Controllable growth of oriented ZnO nanorods using Ga-doped seed layers and surface acoustic wave humidity sensor,” en, *Sensors and Actuators B: Chemical*, vol. 195, pp. 446–451, May 2014, ISSN: 0925-4005. DOI: 10.1016/j.snb.2013.12.120. [Online]. Available: <http://www.sciencedirect.com/science/article/pii/S0925400514000070> (visited on 01/15/2021).
- [11] Z. Xu and Y. J. Yuan, “Implementation of guiding layers of surface acoustic wave devices: A review,” eng, *Biosensors & Bioelectronics*, vol. 99, pp. 500–512, Jan. 2018, ISSN: 1873-4235. DOI: 10.1016/j.bios.2017.07.060.
- [12] A. Mujahid, A. Afzal, and F. L. Dickert, “An Overview of High Frequency Acoustic Sensors—QCMs, SAWs and FBARs—Chemical and Biochemical Applications,” *Sensors (Basel, Switzerland)*, vol. 19, no. 20, Oct. 2019, ISSN: 1424-8220. DOI: 10.3390/s19204395. [Online]. Available: <https://www.ncbi.nlm.nih.gov/pmc/articles/PMC6833005/> (visited on 01/15/2021).

- [13] M. Jangi, J. Luo, R. Tao, *et al.*, “Concentrated vertical jetting mechanism for isotropically focused ZnO/Si surface acoustic waves,” *International Journal of Multiphase Flow*, vol. 114, Feb. 2019. DOI: 10.1016/j.ijmultiphaseflow.2019.02.002.
- [14] J. Zhou, H. F. Pang, L. Garcia-Gancedo, *et al.*, “Discrete microfluidics based on aluminum nitride surface acoustic wave devices,” en, *Microfluidics and Nanofluidics*, vol. 18, no. 4, pp. 537–548, Apr. 2015, ISSN: 1613-4990. DOI: 10.1007/s10404-014-1456-1. [Online]. Available: <https://doi.org/10.1007/s10404-014-1456-1> (visited on 01/15/2021).
- [15] R. Tao, G. McHale, J. Reboud, *et al.*, “Hierarchical Nanotexturing Enables Acoustofluidics on Slippery yet Sticky, Flexible Surfaces,” *Nano Letters*, vol. 20, no. 5, pp. 3263–3270, May 2020, Publisher: American Chemical Society, ISSN: 1530-6984. DOI: 10.1021/acs.nanolett.0c00005. [Online]. Available: <https://doi.org/10.1021/acs.nanolett.0c00005> (visited on 01/15/2021).
- [16] Z. Tian, S. Yang, P.-H. Huang, *et al.*, “Wave number–spiral acoustic tweezers for dynamic and reconfigurable manipulation of particles and cells,” en, *Science Advances*, vol. 5, no. 5, eaau6062, May 2019, Publisher: American Association for the Advancement of Science Section: Research Article, ISSN: 2375-2548. DOI: 10.1126/sciadv.aau6062. [Online]. Available: <https://advances.sciencemag.org/content/5/5/eaau6062> (visited on 01/15/2021).
- [17] Z. Tian, C. Shen, J. Li, *et al.*, “Programmable Acoustic Metasurfaces,” en, *Advanced Functional Materials*, vol. 29, no. 13, p. 1808489, 2019, eprint: <https://onlinelibrary.wiley.com/doi/pdf/10.1002/adfm.201808489>, ISSN: 1616-3028. DOI: <https://doi.org/10.1002/adfm.201808489>. [Online]. Available: <https://onlinelibrary.wiley.com/doi/abs/10.1002/adfm.201808489> (visited on 01/15/2021).
- [18] R. Tao, J. Reboud, H. Torun, *et al.*, “Integrating microfluidics and biosensing on a single flexible acoustic device using hybrid modes,” en, *Lab on a Chip*, vol. 20, no. 5, pp. 1002–1011, Mar. 2020, Publisher: The Royal Society of Chemistry, ISSN: 1473-0189. DOI: 10.1039/C9LC01189G. [Online]. Available: <https://pubs.rsc.org/en/content/articlelanding/2020/lc/c9lc01189g> (visited on 01/15/2021).
- [19] H. Jin, J. Zhou, X. He, *et al.*, “Flexible surface acoustic wave resonators built on disposable plastic film for electronics and lab-on-a-chip applications,” eng, *Scientific Reports*, vol. 3, p. 2140, 2013, ISSN: 2045-2322. DOI: 10.1038/srep02140.

- [20] A. Stelzer, G. Schimetta, L. Reindl, A. Springer, and R. Weigel, “Wireless SAW sensors for surface and subsurface sensing applications,” in *Subsurface and Surface Sensing Technologies and Applications III*, vol. 4491, International Society for Optics and Photonics, Nov. 2001, pp. 358–366. DOI: 10.1117/12.450181. [Online]. Available: <https://www.spiedigitallibrary.org/conference-proceedings-of-spie/4491/0000/Wireless-SAW-sensors-for-surface-and-subsurface-sensing-applications/10.1117/12.450181.short> (visited on 01/15/2021).
- [21] V. K. Varadan, P. T. Teo, K. A. Jose, and V. V. Varadan, “Design and development of a smart wireless system for passive temperature sensors,” en, *Smart Materials and Structures*, vol. 9, no. 4, pp. 379–388, Jun. 2000, Publisher: IOP Publishing, ISSN: 0964-1726. DOI: 10.1088/0964-1726/9/4/301. [Online]. Available: <https://doi.org/10.1088/0964-1726/9/4/301> (visited on 01/15/2021).
- [22] S. Zahertar, Y. Wang, R. Tao, J. Xie, Y. Q. Fu, and H. Torun, “A fully integrated biosensing platform combining acoustofluidics and electromagnetic metamaterials,” en, *Journal of Physics D: Applied Physics*, vol. 52, no. 48, p. 485 004, Sep. 2019, Publisher: IOP Publishing, ISSN: 0022-3727. DOI: 10.1088/1361-6463/ab3f7d. [Online]. Available: <https://doi.org/10.1088/1361-6463/ab3f7d> (visited on 01/15/2021).
- [23] H. Torun, F. Cagri Top, G. Dundar, and A. D. Yalcinkaya, “An antenna-coupled splitting resonator for biosensing,” *Journal of Applied Physics*, vol. 116, no. 12, p. 124 701, Sep. 2014, Publisher: American Institute of Physics, ISSN: 0021-8979. DOI: 10.1063/1.4896261. [Online]. Available: <https://aip.scitation.org/doi/10.1063/1.4896261> (visited on 01/15/2021).
- [24] A. P. Mayer and M. Lehner, “Effect of random surface and interface roughness on the propagation of surface acoustic waves,” *Waves in Random Media*, vol. 4, no. 3, pp. 321–335, Jul. 1994, Publisher: Taylor & Francis. eprint: <https://doi.org/10.1088/0959-7174/4/3/007>, ISSN: 0959-7174. DOI: 10.1088/0959-7174/4/3/007. [Online]. Available: <https://doi.org/10.1088/0959-7174/4/3/007> (visited on 01/15/2021).
- [25] Y. Q. Fu, J. K. Luo, N. T. Nguyen, *et al.*, “Advances in piezoelectric thin films for acoustic biosensors, acoustofluidics and lab-on-chip applications,” en, *Progress in Materials Science*, vol. 89, pp. 31–91, Aug. 2017, ISSN: 0079-6425. DOI: 10.1016/j.pmatsci.

- 2017.04.006. [Online]. Available: <http://www.sciencedirect.com/science/article/pii/S0079642517300403> (visited on 01/15/2021).
- [26] R. Tao, S. Zahertar, H. Torun, *et al.*, “Flexible and Integrated Sensing Platform of Acoustic Waves and Metamaterials based on Polyimide-Coated Woven Carbon Fibers,” *ACS sensors*, vol. 5, no. 8, pp. 2563–2569, 2020, ISBN: 2379-3694 Publisher: ACS Publications.
- [27] B. Camli, E. Kusakci, B. Lafci, S. Salman, H. Torun, and A. D. Yalcinkaya, “Cost-Effective, Microstrip Antenna Driven Ring Resonator Microwave Biosensor for Biospecific Detection of Glucose,” *IEEE Journal of Selected Topics in Quantum Electronics*, vol. 23, no. 2, pp. 404–409, Mar. 2017, Conference Name: IEEE Journal of Selected Topics in Quantum Electronics, ISSN: 1558-4542. DOI: 10.1109/JSTQE.2017.2659226.
- [28] J. Kim, G. A. Salvatore, H. Araki, *et al.*, “Battery-free, stretchable optoelectronic systems for wireless optical characterization of the skin,” *en, Science Advances*, vol. 2, no. 8, e1600418, Aug. 2016, Publisher: American Association for the Advancement of Science Section: Research Article, ISSN: 2375-2548. DOI: 10.1126/sciadv.1600418. [Online]. Available: <https://advances.sciencemag.org/content/2/8/e1600418> (visited on 01/15/2021).
- [29] Y. R. Jeong, J. Kim, Z. Xie, *et al.*, “A skin-attachable, stretchable integrated system based on liquid GaInSn for wireless human motion monitoring with multi-site sensing capabilities,” *en, NPG Asia Materials*, vol. 9, no. 10, e443–e443, Oct. 2017, Number: 10 Publisher: Nature Publishing Group, ISSN: 1884-4057. DOI: 10.1038/am.2017.189. [Online]. Available: <https://www.nature.com/articles/am2017189> (visited on 01/15/2021).
- [30] L. P. Kobets and I. S. Deev, “Carbon fibres: Structure and mechanical properties,” *en, Composites Science and Technology*, vol. 57, no. 12, pp. 1571–1580, Jan. 1998, ISSN: 0266-3538. DOI: 10.1016/S0266-3538(97)00088-2. [Online]. Available: <http://www.sciencedirect.com/science/article/pii/S0266353897000882> (visited on 01/15/2021).
- [31] G. Carlotti, G. Socino, A. Petri, and E. Verona, “Acoustic investigation of the elastic properties of ZnO films,” *Applied Physics Letters*, vol. 51, no. 23, pp. 1889–1891, Dec. 1987, Publisher: American Institute of Physics, ISSN: 0003-6951. DOI: 10.1063/1.98502. [Online]. Available: <https://aip.scitation.org/doi/10.1063/1.98502> (visited on 01/15/2021).
- [32] T. B. Bateman, “Elastic Moduli of Single-Crystal Zinc Oxide,” *Journal of Applied Physics*, vol. 33, no. 11, pp. 3309–3312, Nov. 1962, Publisher: American Institute of Physics, ISSN:

- 0021-8979. DOI: 10.1063/1.1931160. [Online]. Available: <https://aip.scitation.org/doi/abs/10.1063/1.1931160> (visited on 01/15/2021).
- [33] N. Ashkenov, B. N. Mbenkum, C. Bundesmann, *et al.*, “Infrared dielectric functions and phonon modes of high-quality ZnO films,” *Journal of Applied Physics*, vol. 93, no. 1, pp. 126–133, Dec. 2002, Publisher: American Institute of Physics, ISSN: 0021-8979. DOI: 10.1063/1.1526935. [Online]. Available: <https://aip.scitation.org/doi/10.1063/1.1526935> (visited on 01/15/2021).
- [34] H. Bartsch, M. Baca, U. Fernekorn, J. Müller, A. Schober, and H. Witte, “Functionalized Thick Film Impedance Sensors for Use in In Vitro Cell Culture,” *eng, Biosensors*, vol. 8, no. 2, Apr. 2018, ISSN: 2079-6374. DOI: 10.3390/bios8020037.
- [35] P. K. Das, A. D. Snider, and V. R. Bhethanabotla, “Acoustothermal heating in surface acoustic wave driven microchannel flow,” *Physics of Fluids*, vol. 31, no. 10, p. 106 106, Oct. 2019, Publisher: American Institute of Physics, ISSN: 1070-6631. DOI: 10.1063/1.5121307. [Online]. Available: <https://aip.scitation.org/doi/abs/10.1063/1.5121307> (visited on 01/15/2021).
- [36] Y. Liu, Y. Li, A. M. el-Hady, *et al.*, “Flexible and bendable acoustofluidics based on ZnO film coated aluminium foil,” English, *Sensors and Actuators B: Chemical*, vol. 221, pp. 230–235, Dec. 2015, Publisher: Elsevier. DOI: 10.1016/j.snb.2015.06.083. [Online]. Available: [https://researchportal.northumbria.ac.uk/en/publications/flexible-and-bendable-acoustofluidics-based-on-zno-film-coated-aluminium-foil\(67a954f9-4bc0-4508-94fc-e2e94c93c3c2\)/export.html](https://researchportal.northumbria.ac.uk/en/publications/flexible-and-bendable-acoustofluidics-based-on-zno-film-coated-aluminium-foil(67a954f9-4bc0-4508-94fc-e2e94c93c3c2)/export.html) (visited on 01/15/2021).
- [37] C. A. Silva, E. (Marotta, M. Schuller, L. Peel, and M. O’Neill, “In-Plane Thermal Conductivity in Thin Carbon Fiber Composites,” *Journal of Thermophysics and Heat Transfer*, vol. 21, no. 3, pp. 460–467, Jul. 2007, Publisher: American Institute of Aeronautics and Astronautics. DOI: 10.2514/1.27859. [Online]. Available: <https://arc.aiaa.org/doi/10.2514/1.27859> (visited on 01/15/2021).
- [38] X. Tao, H. Jin, M. Mintken, *et al.*, “Three-Dimensional Tetrapodal ZnO Microstructured Network Based Flexible Surface Acoustic Wave Device for Ultraviolet and Respiration Monitoring Applications,” *ACS Applied Nano Materials*, vol. 3, no. 2, pp. 1468–1478, Feb. 2020, Publisher: American Chemical Society. DOI: 10.1021/acsanm.9b02300. [Online]. Available: <https://doi.org/10.1021/acsanm.9b02300> (visited on 01/15/2021).

- [39] Y. J. Guo, C. Zhao, X. S. Zhou, *et al.*, “Ultraviolet sensing based on nanostructured ZnO/Si surface acoustic wave devices,” en, *Smart Materials and Structures*, vol. 24, no. 12, p. 125 015, Nov. 2015, Publisher: IOP Publishing, ISSN: 0964-1726. DOI: 10.1088/0964-1726/24/12/125015. [Online]. Available: <https://doi.org/10.1088/0964-1726/24/12/125015> (visited on 01/15/2021).

Chapter 6

A Flexible PVDF-based Platform Combining Acoustofluidics and Electromagnetic Metamaterials

In this chapter, the feasibility of the proposed concept for integration is investigated on a flexible piezoelectric polymer. For this purpose, a rectangular geometry containing straight interdigital transducers is fabricated on a polyvinylidene fluoride (PVDF) substrate and the device is characterised in radio and microwave frequency bands.

This chapter is based on a conference paper presented in 2020 IEEE International Conference on Flexible and Printable Sensors and Systems (FLEPS), IEEE, 2020¹.

¹© 2020 IEEE. Reprinted, with permission, from Shahrzad Zahertar^A, Jiaen Wu^B, George Chatzipirpiridis^B, Olgac Ergeneman^B, Pep Canyelles-Pericas^C, Ran Tao^A, Yong Qing Fu^A, Hamdi Torun^A, “A Flexible PVDF-based Platform Combining Acoustofluidics and Electromagnetic Metamaterials,” in 2020 IEEE International Conference on Flexible and Printable Sensors and Systems (FLEPS), IEEE, 2020, pp. 1–4

A Department of Mathematics, Physics and Electrical Engineering, Northumbria University, Newcastle upon Tyne, UK

B Institute of Robotics & Intelligent Systems (IRIS), ETH Zürich, Zurich, Switzerland

C University of Twente, Department of Integrated Devices and Systems, Enschede, The Netherlands

Abstract

Acoustofluidic devices have been demonstrated effectively for liquid manipulation functionalities. Likewise, electromagnetic metamaterials have been employed as highly sensitive and wireless sensors. In this work, we introduced a new design combining the concepts of acoustofluidics and electromagnetic metamaterials on a single device realised on a flexible PVDF substrate. We characterise the operation of the device at acoustic and microwave frequencies. The device can be used in wearable biosensors with integrated liquid sampling and continuous wireless sensing capabilities.

6.1 Introduction

A major focus in wearable biosensing technology is on the development of devices and methods to realise liquid manipulation, highly sensitive detection and wireless operation on flexible platforms. Although these functionalities have been demonstrated using individual devices, the need for a comprehensive approach to integrate these functionalities and beyond on a single platform towards a next generation of wearable devices still remains. Among different technologies, acoustofluidic devices have been proven to be effective for liquid manipulation and actuation with some promise to realise sensitive detection and wireless operation [1], [2]. On the other hand, electromagnetic metamaterials offer excellent capabilities for sensitive and wireless detection [3], [4].

In this work, we show the feasibility for a wearable sensing platform integrating two emerging technologies: electromagnetic metamaterial sensors and piezoelectric polymer-based acoustofluidic actuators on a single device. This platform will enable us to address three key challenges for future wearable devices: i) wireless and sensitive detection; ii) liquid manipulation and actuation; iii) personalisation. Metamaterials will enable fast, accurate, and wireless sensing capabilities, whereas piezoelectric polymers will enable liquid actuation capabilities with energy harvesting options in flexible implementations. There has been significant amount of work recently for the development of these individual technologies, however, our research is focused on the integration of these technologies on a single device for the development of a new affordable, scalable, and customised platform for wearable devices. In this work, we used polyvinylidene fluoride (PVDF) metallised with patterned electrodes to realise the devices.

PVDF is a functional piezopolymer that has found several applications, such as an electrical insulator, a binder in lithium ion batteries or as a membrane for protein blotting attributed to its distinct chemical, mechanical, and electrical properties. Additionally, the piezoelectric properties of PVDF have been exploited for manufacturing electroacoustic transducers, tactile sensors, and actuators [5]. Unlike its state-of-the-art stiff and fragile piezoelectric material counterparts, PVDF can be easily shaped and is suitable for bending, a requirement for wearable sensors. Another advantage of PVDF is that its mechanical and electric properties can be tailored by copolymerizing PVDF with monomers such as trifluoroethylene (TrFE), chlorotrifluoroethylene (CTFE) and HFP (hexafluoropropylene). PVDF is also a piezoelectric building block in magnetically coupled piezoelectric devices and magnetoelectric composites.

6.2 Design and Fabrication of the Devices

Surface acoustic wave (SAW) resonators are one of the building blocks of acoustofluidic devices where a metallised interdigitated transducer (IDT) is defined on a piezoelectric substrate.

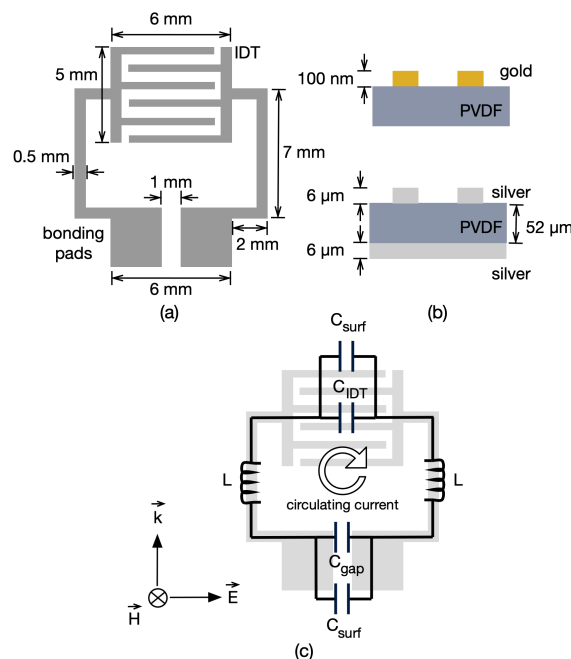


Figure 6.1: (a) Schematics of the metallised layer on a PVDF substrate, (b) cross-sectional overview of the fabricated devices, (c) induced circulating current and the equivalent circuit of the device operating as an electromagnetic metamaterial [6].

The characteristics of the resonator are determined by the geometry of the IDT and are relatively independent to the geometry of the conductors connecting the IDT to the bonding pads where electrical connection is made. Careful design of the conducting line, bonding pad and the IDT can define an electromagnetic resonator at the resonant frequency of which induced current can circulate as we demonstrated recently [7]. Figure 6.1(a) shows a design where we designed the metallic layer to serve both functionalities. The IDT comprises 20 pairs of fingers with a wavelength of $300\ \mu\text{m}$ to generate surface acoustic waves on the PVDF substrate. We fabricated two variations of devices using a single gold layer sputtered on a PVDF layer and double silver ink layers on another PVDF layer as shown in Figure 6.1(b). Under an electromagnetic field excitation, the metallic structure electrically forms an LC resonator at its magnetic resonance as schematically shown in Figure 6.1(c). A circulating resonant current is induced along its surface with its resonant frequency being determined by the geometry of the structure. The inductance (L) is given by the conductor geometry, the capacitance is determined by the gap (C_g), the IDT (C_{IDT}) and the surface (C_s) of the structure. These resonators in centimetre to millimetre-scale are usually used for applications in microwave bands, exhibiting very sharp resonant behaviour with quality factors larger than 1,000 unlike conventional types of passive resonators [8]. Owing to high quality factors, the change in resonant frequency of an SRR structure can effectively be used as a sensing mechanism, which can be induced by a change in dielectric properties of the medium and the geometry of the structure.

6.3 Characterisation of the Devices

We characterised the acoustic and electromagnetic characteristics of the fabricated devices. First, we measured the reflection spectra (S_{11}) of the devices at acoustic frequencies by connecting the bonding pads to a vector network analyser. Figure 6.2 shows the fundamental resonant frequency of the PVDF/silver-electrode device is 3.2 MHz. This corresponds to a speed of sound in the PVDF sample as 960 m/s.

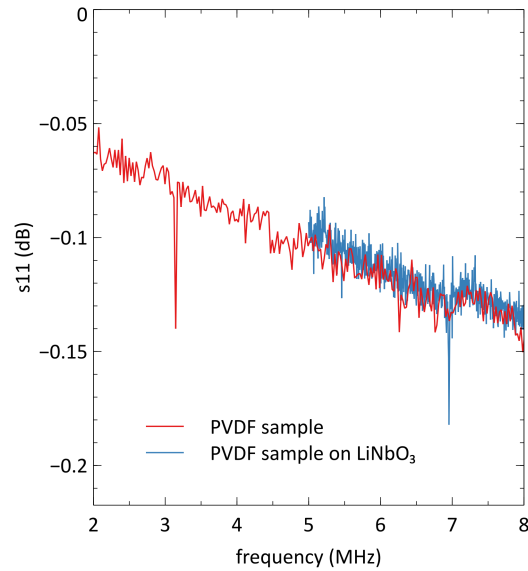


Figure 6.2: S_{11} spectra of the PVDF/silver-electrode device measured between the bonding pads [6].

We repeated this measurement after placing the PVDF sample on top of a LiNbO_3 plate. The resonant frequency is shifted to 7 MHz, corresponding to a speed of sound of 2100 m/s. The PVDF film is thin and travelling waves can be transmitted to the LiNbO_3 plate resulting in increased frequency and effective speed of sound.

In addition to acoustic characterisation, we excited the devices electromagnetically using a pair of monopole antennas to measure the electromagnetic resonant frequency of them. We used monopole patch antennas that are 26 mm in length and 3 mm in width, realised on a 35 μm -thick Cu layer on a PCB substrate. We connect the antennas to the ports of a vector network analyser to excite the device electromagnetically and to measure the transmission (S_{21}) spectra of the devices between the antennas. Figure 6.3 shows the S_{21} spectrum of a device with a fundamental resonant frequency of 3.4 GHz and a quality factor of 300.

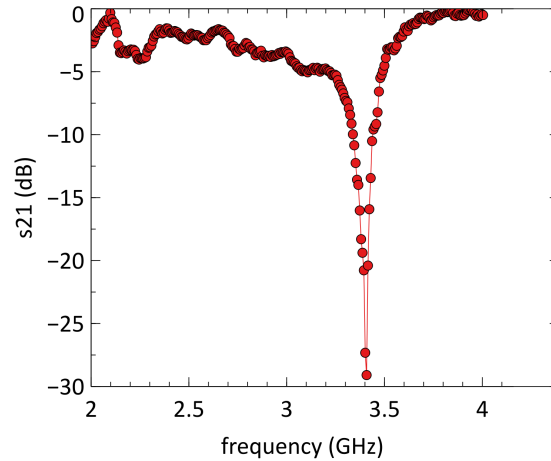


Figure 6.3: S_{21} spectra of the PVDF/gold-electrode device measured using a pair of monopole antennas connected to a vector network analyser [6].

The measured electromagnetic resonant frequency of the device corresponds to a case where circulating current is induced along the conducting path shown in Figure 6.1(c). We investigated the electromagnetic resonances based on different excitations of the device as shown in Fig 4 using an electromagnetic simulator (CST Microwave Studio). When the electric field is along the gap (Figure 6.4(a) and Figure fig:c4-4 (b)), the field can polarise the opposing pads resulting in a circulating current. Likewise, when the magnetic field is normal to the device (Figure 6.4(b) and Figure 6.4(c)), a circulating current is induced. In addition, when the electric current is also perpendicular the fingers (Figure 6.4(c)), the alternating fingers can be polarised resulting in complex current paths on the IDT area. This excites additional resonances as observed in Figure 6.4(c). When neither the magnetic field is normal to the device nor the electric field polarises the gap, no resonance is observed within the range of 3-4.5 GHz (Figure 6.4(d)).

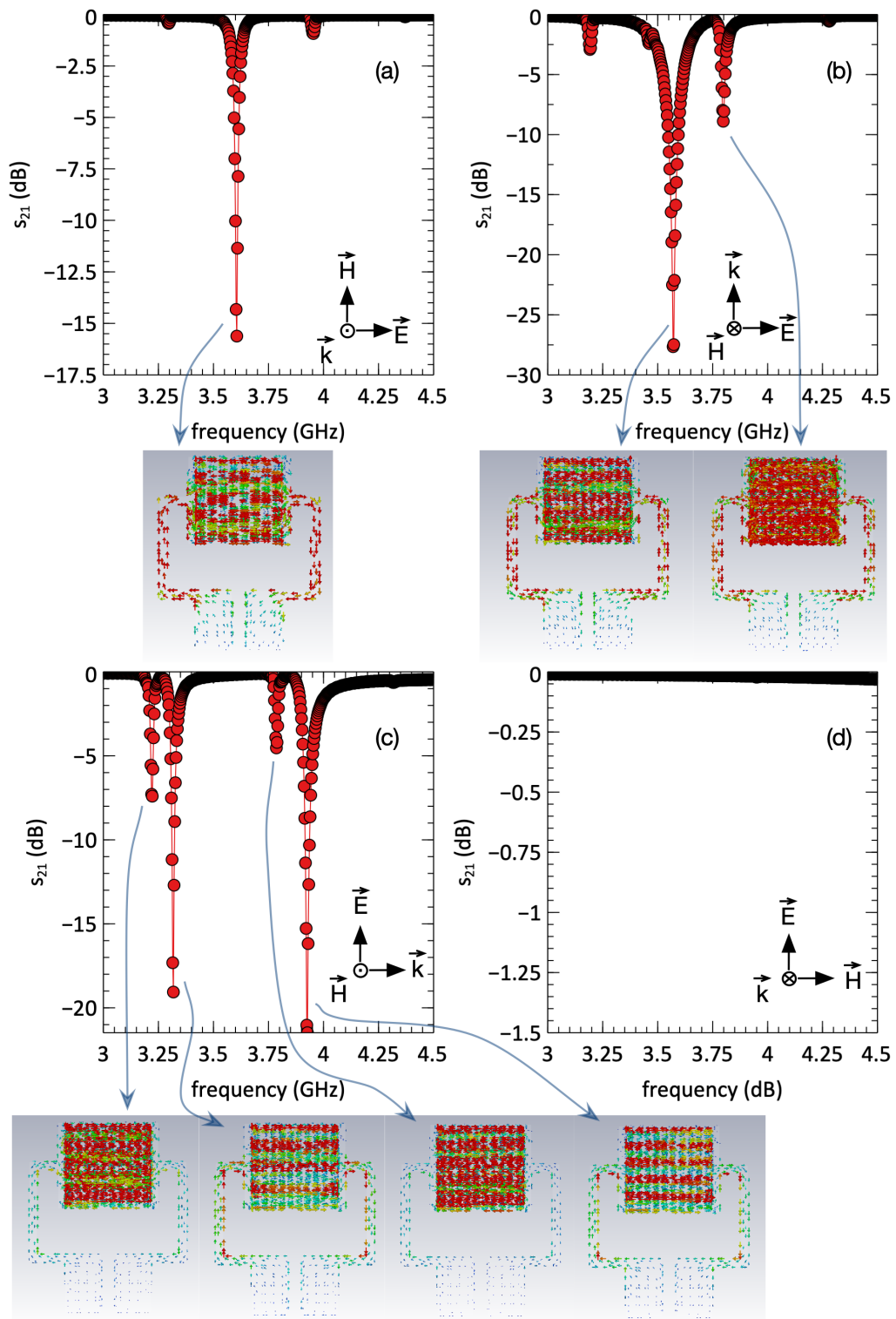


Figure 6.4: Simulated electromagnetic resonances of the device with different excitation conditions [6].

We tested the device for its capability in microfluidic actuation using a similar experimental setup explained in previous chapters. However, we found out that the device in its acoustic frequency is not efficient to perform any microfluidic function. One reason could be the excessive acoustic power attenuated in the polymer substrate. The other reason could be the technology involved in the fabrication process for patterning the IDTs; surface acoustic actuation relies on at least a pair of IDTs patterned on a piezoelectric substrate. In this set of devices, laser milling was utilised to develop the IDTs on PVDF. This technique can cause localised heating in the substrate and as a result, the PVDF film may have lost its piezoelectric material property after the fabrication due to the heating. Therefore, optimisation in fabrication parameters and further experiments are required to be able to proceed further.

6.4 Conclusions

In this work, we introduced a new design combining surface acoustic waves and electromagnetic metamaterials on a single device realised on a PVDF substrate. The device exhibits an acoustic resonance at 3.2 MHz and an electromagnetic resonance at 3.4 GHz. The acoustic resonance can be used for liquid manipulation whereas the electromagnetic resonance can be used for sensing functionalities. However, the device optimisation and further experiments are needed to achieve these objectives.

In the next chapter, the focus is on design and fabrication of a flexible sensor for characterising dielectric materials. For this purpose, an embroidered rectangular SRR is fabricated on a cloth. The device is wrapped around a bottle and has been excited utilising monopole antennas. The behaviour of the device is identified through simulations and is verified by experiments. Next, the bottle is filled with various dielectric materials per experiment. The change in frequency by altering material is observed in microwave regime.

References

- [1] Y. Q. Fu, J. K. Luo, X. Y. Du, *et al.*, “Recent developments on ZnO films for acoustic wave based bio-sensing and microfluidic applications: A review,” en, *Sensors and Actuators B: Chemical*, vol. 143, no. 2, pp. 606–619, Jan. 2010, ISSN: 0925-4005. DOI: 10.1016/j.snb.2009.10.010. [Online]. Available: <http://www.sciencedirect.com/science/article/pii/S0925400509007783> (visited on 01/15/2021).
- [2] P. Zhu and L. Wang, “Passive and active droplet generation with microfluidics: A review,” *Lab on a Chip*, vol. 17, no. 1, pp. 34–75, 2017.
- [3] T. Chen, S. Li, and H. Sun, “Metamaterials Application in Sensing,” *Sensors (Basel, Switzerland)*, vol. 12, no. 3, pp. 2742–2765, Feb. 2012, ISSN: 1424-8220. DOI: 10.3390/s120302742. [Online]. Available: <https://www.ncbi.nlm.nih.gov/pmc/articles/PMC3376603/> (visited on 01/15/2021).
- [4] A. Salim and S. Lim, “Review of recent metamaterial microfluidic sensors,” *Sensors*, vol. 18, no. 1, p. 232, 2018.
- [5] B. Stadlober, M. Zirkl, and M. Irimia-Vladu, “Route towards sustainable smart sensors: Ferroelectric polyvinylidene fluoride-based materials and their integration in flexible electronics,” *Chemical Society Reviews*, vol. 48, no. 6, pp. 1787–1825, 2019.
- [6] S. Zahertar, J. Wu, G. Chatzipirpiridis, *et al.*, “A Flexible PVDF-based Platform Combining Acoustofluidics and Electromagnetic Metamaterials,” in *2020 IEEE International Conference on Flexible and Printable Sensors and Systems (FLEPS)*, IEEE, 2020, pp. 1–4, ISBN: 1-72815-278-X.
- [7] S. Zahertar, Y. Wang, R. Tao, J. Xie, Y. Q. Fu, and H. Torun, “A fully integrated biosensing platform combining acoustofluidics and electromagnetic metamaterials,” en, *Journal of Physics D: Applied Physics*, vol. 52, no. 48, p. 485 004, Sep. 2019, Publisher: IOP Pub-

lishing, ISSN: 0022-3727. DOI: 10.1088/1361-6463/ab3f7d. [Online]. Available: <https://doi.org/10.1088/1361-6463/ab3f7d> (visited on 01/15/2021).

- [8] H. Torun, F. Cagri Top, G. Dunder, and A. D. Yalcinkaya, “An antenna-coupled splitting resonator for biosensing,” *Journal of Applied Physics*, vol. 116, no. 12, p. 124 701, Sep. 2014, Publisher: American Institute of Physics, ISSN: 0021-8979. DOI: 10.1063/1.4896261. [Online]. Available: <https://aip.scitation.org/doi/10.1063/1.4896261> (visited on 01/15/2021).

Chapter 7

Embroidered Rectangular Split-Ring Resonators for the Characterization of Dielectric Materials

Another key progress towards fabrication of next-generation sensing platforms is development of flexible wireless sensors; the focus is centred on this objective within this chapter. For this purpose, a rectangular split-ring resonator is embroidered on a cloth and is wrapped around a bottle. The SRR is excited by monopole antennas and the frequency response of the device is monitored in microwave frequencies when the bottle is filled with various chemical substances.

This chapter is based on a manuscript published in IEEE Sensors¹.

¹© 2020 IEEE. Reprinted, with permission, from Shahrzad Zahertar^A, Emma Laurin^B, Linzi E. Dodd^A, and Hamdi Torun^A, “Embroidered Rectangular Split-Ring Resonators for the Characterization of Dielectric Material,” in 2019 IEEE Sensors Journal, 2019, pp. 2434-2439

A Department of Mathematics, Physics and Electrical Engineering, Northumbria University, Newcastle upon Tyne, UK

B Université de Poitiers, IUT Mesures Physiques Chatellerault Châtellerault, France

Abstract

In this chapter, we report an embroidered rectangular split-ring resonator (SRR) operating at S band for material characterization based on the differences in dielectric parameters. We designed, fabricated and characterized SRR sensors on a conventional fabric that can be conformally attached over the surface of samples under investigation. The structures are made of conductive threads and can be embroidered on any dielectric fabric at low cost using conventional embroidery methods. We have demonstrated material characterization capability of the sensors using a specific design with a length of 60 mm and a width of 30 mm. We wrapped the sensors on low-density polyethylene (LDPE) bottles filled with deionized (DI) water and common solvents (ethanol, methanol, isopropanol and acetone) in our experiments. We measured the nominal resonant frequency of a specific sensor wrapped around an empty bottle as 2.07 GHz. The shifts in resonant frequencies when the bottle was filled with the solvents follow the dielectric constants of the solvents.

7.1 Introduction

Split-ring resonators (SRR) are the basic building blocks for metamaterials. SRR structures have been successfully demonstrated for the control and manipulation of electromagnetic waves in a broad spectral range from microwaves [1] to terahertz [2] and infrared [3]. The geometry of the structure, usually a circular or rectangular metallic ring with one or multiple splits, determines the frequency of operation. Structures with millimeter- to centimeter-scale are usually employed as microwave resonators. The structures are driven in electrical resonance when they polarize electric field or when they support induced circulating current over their surface. The resonance is known as an electric resonance in the former case, and a magnetic resonance in the latter case. Any change in the geometry or electrical characteristics of the medium alters the resonant frequency as the polarization of the electric field or induction of the circulating current relies on the effective capacitance and inductance defined by the structure. Tracking the changes in resonant frequency has been exploited as an effective sensing mechanism to determine changes in the geometry of SRR structures [4] and in the permittivity of the environment [5]–[10]. This is especially advantageous since the quality factor of the resonators can be over 1000 in microwave band [11].

Flexible sensors have been at the focus of delivering mechanically conformal structures for various applications including smart skins, wearable devices and microfluidic platforms. SRR structures fabricated on thin flexible substrates have been introduced as flexible devices. Among these, different configurations based on conventional metallic electrodes on flexible substrates such as polypropylene [12], polyimide [13] and poly-ethylene terephthalate(PET) [14] have been reported. Another configuration is based on inkjet-printed electrodes on PET [15]. The electrodes can also be defined using silver conductive paint as reported for strain sensing on a flexible latex substrate [4]. In an unconventional implementation, liquid metal (Galinstan) electrodes were employed in a microfluidic channel made of polydimethylsiloxane (PDMS) [16]. Also, a substrate-free configuration made of conductive rubber was reported for strain sensing applications [17].

An emerging field for the realization of flexible devices is embroidery that has been used to deliver electronic textiles using inherently flexible conductive threads on flexible fabric substrates. The developments in new electronic elements and interconnects in electronic textiles have made it possible to develop devices for a range of wearable applications from sensors to computers [18], [19]. Conductive threads, as the basic interconnect element that are inherently flexible has enabled the realization of metallic structures on conventional fabrics. Antennas are typical examples for which the whole structure can be implemented using only conductive threads [20]. Similar to antennas, metamaterials based on SRRs [21]–[23] and radio frequency identification (RFID) tags [24] are usually realized using a few layers of metallic structures on fabrics for sensing and electromagnetic signal conditioning applications.

In this work, we report an embroidered rectangular SRR operating at S band for material characterization based on the differences in dielectric parameters. The SRR geometry is based on a previous work of ours, using which we investigated the operating principles of rectangular SRRs and explained an unexpected observation based on a particular excitation of the structures that induces magnetic resonance [25], [26]. The rectangular SRR configuration with the particular excitation method is advantageous for sensing applications. We fabricated a new structure using a conductive thread, which contains 316L stainless steel fibers on a calico cotton fabric. We employed this structure as a flexible sensor that can be wrapped around samples to measure their electromagnetic properties. The sensor is electrically passive and can be measured wirelessly. Our method can be used for the measurement of arbitrary geometries for material characterization

applications attributed to the mechanically conformal structure and the wireless readout capability. The breadth of applications in material characterization using microwave-based sensors have been expanding including biosensing, impurity measurements, ensuring food safety and quality assessment [27]–[34].

7.2 Materials and Methods

We fabricated the SRR sensors using an embroidery machine (Brother PR1050X) with stainless-steel conductive threads (Sparkfun). A typical sensor and its dimensions are shown in Figure 7.1. We fabricated the designs using a 6 mm wide design consisting of a 4 mm wide satin ‘fill’ stitch, an overlapping line stitch around the edge with a zig-zag width of 1.5 mm, both with a stitch density of 4.5 lines/mm and 7 rows of under sewing to reduce the resonator impedance. We measured the sheet resistance of the resonator as $4.67 \text{ m } \Omega\text{-per-square}$. We implemented an inverted methodology to create the stitch patterns, whereby we placed the conductive thread in the lower bobbin of the embroidery machine, while we used standard polyester thread (#50, Brother) as the top spool thread. We used high thread tensions to reduce the amount of polyester thread visible on the conductive side of the design and to ensure the correct dimensions of the resonator design. Furthermore, we used the combined satin fill stitch and line edging pattern to ensure accuracy of the design width, as previous experiments using a wider satin stitch without an edge were generally too thin, compared to their design parameters, caused by this stitch pull-through effect. This approach ensured that the parameters of the fabricated resonator matched that of the design. We also used tear away stabilizer on the underside of the design to provide additional stability and to reduce fabric gather, which could have further affected the critical dimensions.

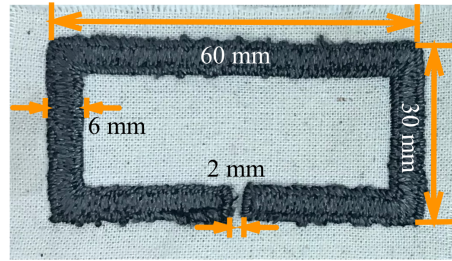


Figure 7.1: Photograph of the fabricated SRR structure with a single split using an inverted embroidery method [26].

Then, we attached the embroidered sensor on curved surfaces of low-density polyethylene (LDPE) bottles for measurements using a vector network analyzer (VNA, Agilent N5230A PNA – L) as shown in Figure 7.2. We used a pair of monopole patch antennas with a length of 30 mm and a width of 3.5 mm to excite the resonators while we measured S_{21} spectra between the ports of the VNA. During our measurements, we measured the spectra when the LDPE bottle was empty and filled with deionized water and different solvents of ethanol, methanol, and isopropanol (IPA) and acetone. We repeated the measurements for each case for 15 times.

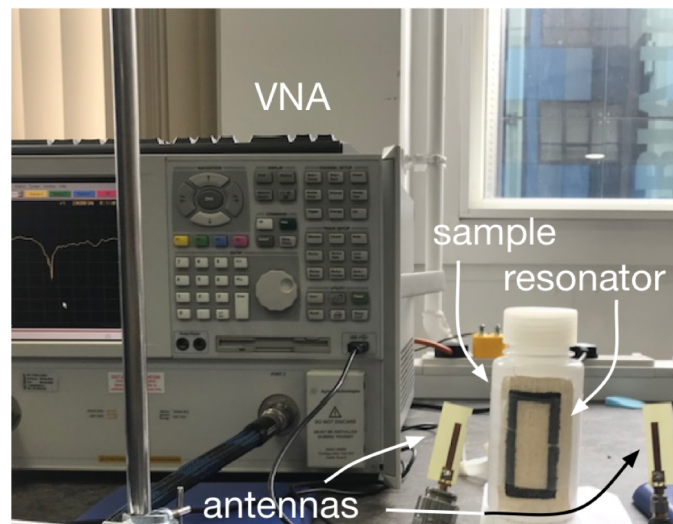


Figure 7.2: Photograph of the experimental setup where an embroidered sensor is attached to an LDPE bottle filled with solvents [26].

We modelled the electromagnetic behavior of the resonators using commercially available electromagnetic simulation software (CST Studio Suite, Darmstadt Germany). We used plane wave conditions for the excitation of the structures with different boundary conditions. We varied the relative permittivity of the medium in our simulations to model the presence of the fabric substrate

and the LDPE bottle during the measurements. We used an effective relative permittivity value of 1.4 that matches well with the different modes of resonances we report in this chapter.

7.3 Results and Discussion

Figure 7.3(a) shows the simulated S_{21} spectra for a specific excitation condition, where the electric field is along short sides of the SRR, the magnetic field is along long sides of the SRR, and the propagation vector is perpendicular to the surface of the resonator. When the electric field is along the short sides, the field can induce dipole formation along the direction of electric field. If the field is strong enough for the dipole formation and if the geometry of the structure can support this, two similar circulating current paths that are flowing in opposite directions are created as shown in Figure 7.3 (b). We observe this formation indicating an electric-field assisted magnetic resonance at two distinct frequencies. When we aligned the antennas to support this excitation, we clearly observed the second resonance at 2.07 GHz. Our experimental results show the first resonance in this band to be broad and at 1.74 GHz. The experimental spectrum is presented after the values are normalized to the maximum value of S_{21} in the measurement band. The monopoles antennas have omnidirectional radiation pattern and can be used to excite different modes of resonances. Hence, it is also possible to excite a coupled mode, and the experimentally measured first resonance can be a result of a coupled mode. We varied the directions of field vectors to observe different modes of resonances using our simulation model.

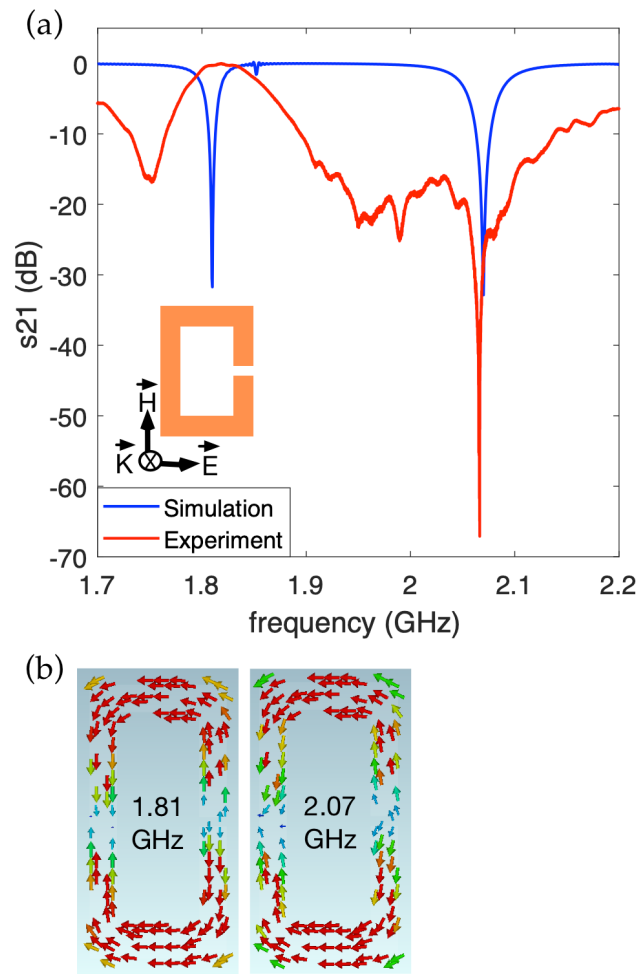


Figure 7.3: (a) Simulation and experimental results (b) Current density patterns at 1.81, and 2.07 GHz for the excitation configuration shown in the figure [26].

Figure 7.4(a) shows the simulation results for another excitation condition, where the propagation vector is along short sides of the resonator, the electric field is along long sides of the resonator, and the magnetic field is perpendicular to the surface of the SRR. When the electric field is along the long side of the structure, it is possible to form an electrical dipole along this side rather than forming patterns of circulating current. Thus, this configuration excites electric resonances. Figure 7.4(b) shows the patterns of current densities at four different resonant frequencies in this band. The resonances within the simulation range indicates the incidences of electric field polarization. The efficient polarization occurs at 2.07 GHz where the incident power is dissipated effectively across the resonator as observed with a deeper signature of S_{21} spectrum. We also measured the spectrum after we aligned the antennas to excite these resonances. Figure 7.4(a) shows the experimentally obtained spectrum after the values are normalized to the maximum value of S_{21} in the

measurement band. The additional resonance at 1.95 GHz observed in Figure 7.4(a) as compared to the results of Figure 7.3(a) indicates the excitation of the device supports the polarization of the electric field along the gap. This resonance corresponds to the resonance we observed at 1.93 GHz in our simulations.

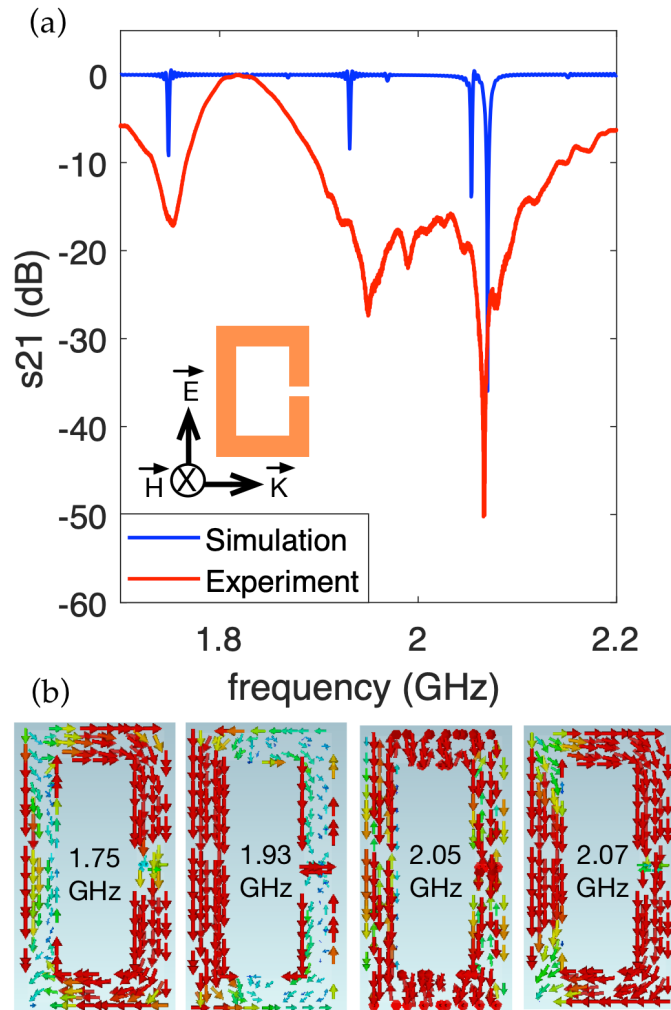


Figure 7.4: (a) Simulation and experimental results (b) Current density patterns at 1.75, 1.93, 2.05, and 2.07 GHz for the excitation setting shown in the figure [26].

Experimentally obtained spectra shown in Figure 7.3(a) and Figure 7.4(a) show different resonant frequencies that can be used for sensing applications. The electromagnetic simulations help us to understand the nature of these resonances. Among these, the second resonance in Figure 7.3(a) at 2.07 GHz exhibits the highest quality factor with a value of 2070. In addition, it is the result of a magnetic resonance where the current path can be altered easily when the dielectric parameters of the medium are altered. Consequently, we monitored this resonance for sensing applications. The

resonant frequency, f_0 , is determined by the effective capacitance, C_{eff} , and the inductance, L_{eff} , of the device along the path of the circulating current as given in Equation 7.1.

$$f_0 = \frac{1}{2\pi\sqrt{L_{eff}C_{eff}}} \quad (7.1)$$

The circulating current density for the second resonance in Figure 7.3(b) at 2.07 GHz reveals two identical paths where the effective capacitance is determined by the nodal points, i.e. the gap and the mid-point along the long side of the rectangle to the left of the gap. The capacitance associated with the surface charges is known as surface capacitance and is contributing to the effective capacitance in addition to the gap capacitance [1]. Each capacitance term is proportional to the permittivity of the medium. Hence, the change in permittivity results in a change in resonant frequency. The structure can be optimized for permittivity sensing based on a specific resonant mode by ensuring the current is interacting with the environment.

We tracked the resonant frequency of the resonator when it was attached to LDPE bottles filled with DI water, methanol, ethanol, IPA, and acetone. Each solvent has a different relative permittivity, leading to a different value of effective capacitance along the current path shown in Figure 7.3(b). Thus, a change in relative permittivity results in a change in resonant frequency. The relative permittivity for DI water, methanol, ethanol, acetone, IPA, and air are 80, 32.6, 22.4, 20.6, 18.3, and 1 respectively [35].

Figure 7.5(a) shows a set of experimentally obtained S_{21} spectra for different solvents and the empty bottle. Each spectrum is presented after it is normalized in the measurement band. The measured frequencies for DI water, methanol, ethanol, acetone, IPA, and empty bottles are 1.88, 1.89, 1.90, 2.01, 2.05, and 2.07 GHz, respectively. The values of quality factor at resonance are in the range of 2010 and 5265. The measured values of quality factor correspond to a frequency resolution of 1 MHz within the measurement range. This is a narrower range as compared to the spectra of Figure 7.3, tracking the second frequency in that figure. The order of frequencies is in agreement with the values of relative permittivity for the samples. The dependency of the resonant frequency to the value of relative permittivity is shown in Figure 7.5(b). We measured samples with relative permittivity values distributed in a wide range within which we do not observe linear response. This is expected based on the operation of the sensor. The relative permittivity of the

samples determines part of the effective capacitance term of equation 1 as the effective capacitance comprises the capacitance terms of the fabric, the bottle and the sample inside the bottle. The shifts in resonant frequencies indicate the changes in real part of the permittivity. The imaginary value of the permittivity contributes to the loss of the resonator and affects the quality factor at resonance. The quality factor of the resonator is determined by all the loss mechanisms in the system including the radiation loss of the resonator and the antennas together with the losses in the fabric, bottle and the sample. We have not observed significant and repeatable changes in quality factor of the resonator during our measurements.

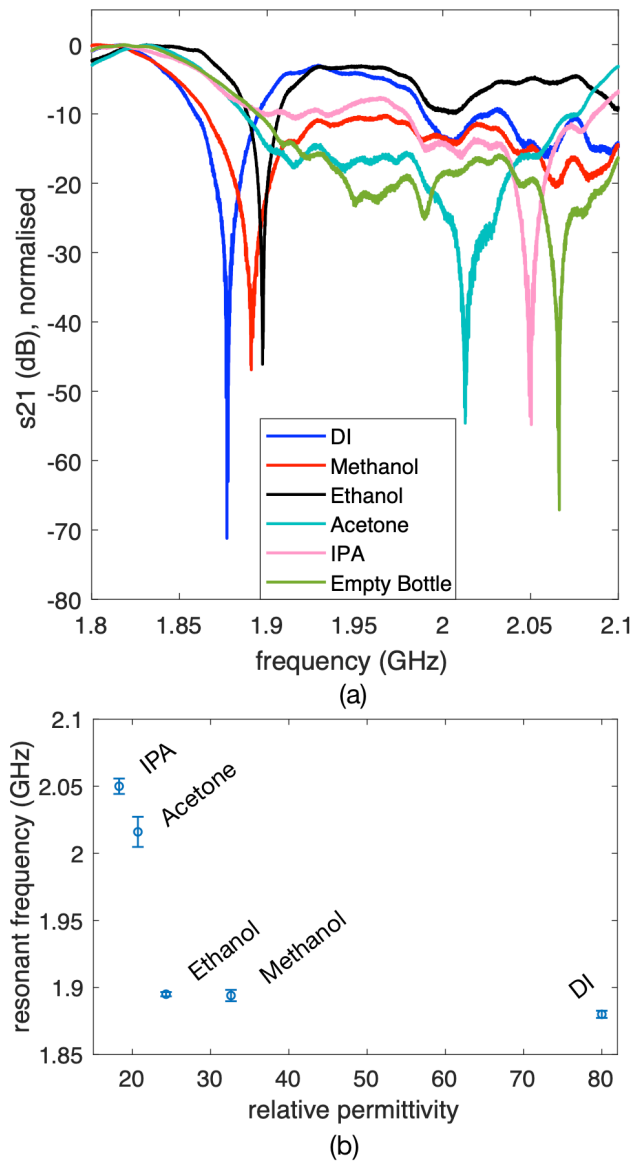


Figure 7.5: (a) Normalized S_{21} spectra of the SRR structure, where the sensor is wrapped around the LDPE bottles filled with DI water, methanol, ethanol, acetone, IPA, and empty bottle. (b) Measured resonant frequencies for different bottles [26].

We repeated the measurement for 15 times to assess the repeatability. Figure 7.6 depicts the histograms of the measured frequencies for the solvents and the empty bottle. Table 7.1 summarizes the material properties and the mean values of measured frequencies.

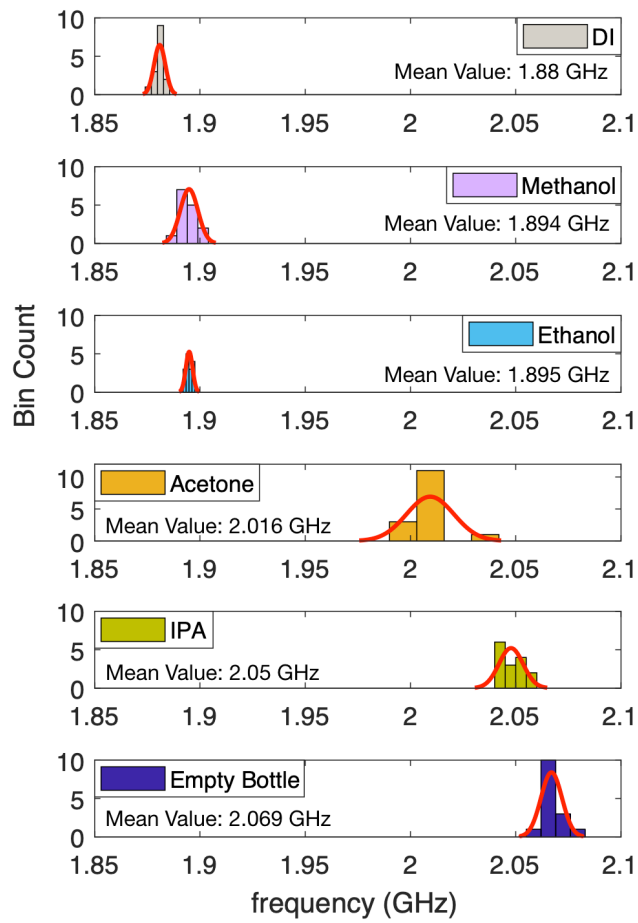


Figure 7.6: Histogram and mean value of the set of experiments for solvents and empty bottle [26].

Table 7.1: Material properties and the mean value of the measured frequencies for solvents.

Material	Relative Permittivity	Resonant Frequency (Mean \pm Standard Deviation) (GHz)
Deionised Water	80	1.88 ± 0.0027
Methanol	32.6	1.894 ± 0.0042
Ethanol	24.3	1.895 ± 0.0016
Acetone	20.7	2.016 ± 0.0112
Isopropanol	18.3	2.05 ± 0.0057
Air	1	2.069 ± 0.0050

7.4 Conclusion

In this chapter, an embroidered rectangular SRR for material characterisation applications is introduced. The SRR has been fabricated using a conductive thread by implementing embroidery methods on an ordinary fabric substrate. The architecture is advantageous for the applications where the sensor needs to be conformally covering sample surfaces. As a case study, the SRR sensor has been wrapped around LDPE bottles filled with DI water and different solvents to demonstrate that the solvents can be identified by tracking the resonant frequency of the SRR, exploiting the fact that the changes in relative permittivity of the samples result in changes in resonant frequency. Also, different modes of resonances are investigated with the help of electromagnetic simulations to select the optimum one for sensing applications. The embroidery method is advantageous for the fabrication of SRR-based sensors where the active device can be defined using a single layer of metallization. This method can be applied to define SRR-based sensors, filters and absorbers on flexible substrates and daily items such as cloth. The study is focused on a device that can be used as a method for substance characterization and has a potential in identifying impurities in liquids for contamination measurements. This configuration can be extended to wearable sensing scenarios where the sensors can be implemented on a conformal structure that can be wrapped around arbitrary shapes depending on the needs. The fabrication method is simple, cost-effective and allows the realization of the sensors very quickly.

References

- [1] H. Torun, F. Cagri Top, G. Dundar, and A. D. Yalcinkaya, “An antenna-coupled splitting resonator for biosensing,” *Journal of Applied Physics*, vol. 116, no. 12, p. 124 701, Sep. 2014, Publisher: American Institute of Physics, ISSN: 0021-8979. DOI: 10.1063/1.4896261. [Online]. Available: <https://aip.scitation.org/doi/10.1063/1.4896261> (visited on 01/15/2021).
- [2] H.-T. Chen, W. J. Padilla, J. M. O. Zide, A. C. Gossard, A. J. Taylor, and R. D. Averitt, “Active terahertz metamaterial devices,” en, *Nature*, vol. 444, no. 7119, pp. 597–600, Nov. 2006, Number: 7119 Publisher: Nature Publishing Group, ISSN: 1476-4687. DOI: 10.1038/nature05343. [Online]. Available: <https://www.nature.com/articles/nature05343> (visited on 01/15/2021).
- [3] C. Rockstuhl, T. Zentgraf, H. Guo, *et al.*, “Resonances of split-ring resonator metamaterials in the near infrared,” en, *Applied Physics B*, vol. 84, no. 1, pp. 219–227, Jul. 2006, ISSN: 1432-0649. DOI: 10.1007/s00340-006-2205-2. [Online]. Available: <https://doi.org/10.1007/s00340-006-2205-2> (visited on 01/15/2021).
- [4] G. Ekinici, A. Calikoglu, S. N. Solak, A. D. Yalcinkaya, G. Dundar, and H. Torun, “Split-ring resonator-based sensors on flexible substrates for glaucoma monitoring,” en, *Sensors and Actuators A: Physical*, vol. 268, pp. 32–37, Dec. 2017, ISSN: 0924-4247. DOI: 10.1016/j.sna.2017.10.054. [Online]. Available: <http://www.sciencedirect.com/science/article/pii/S0924424717304387> (visited on 01/15/2021).
- [5] A. Salim, S. Ghosh, and S. Lim, “Low-Cost and Lightweight 3D-Printed Split-Ring Resonator for Chemical Sensing Applications,” en, *Sensors*, vol. 18, no. 9, p. 3049, Sep. 2018, Number: 9 Publisher: Multidisciplinary Digital Publishing Institute. DOI: 10.3390/

- s18093049. [Online]. Available: <https://www.mdpi.com/1424-8220/18/9/3049> (visited on 01/15/2021).
- [6] E. Reyes-Vera, G. Acevedo-Osorio, M. Arias-Correa, and D. E. Senior, “A Submersible Printed Sensor Based on a Monopole-Coupled Split Ring Resonator for Permittivity Characterization,” en, *Sensors*, vol. 19, no. 8, p. 1936, Jan. 2019, Number: 8 Publisher: Multidisciplinary Digital Publishing Institute. DOI: 10.3390/s19081936. [Online]. Available: <https://www.mdpi.com/1424-8220/19/8/1936> (visited on 01/15/2021).
- [7] W. Withayachumnankul, K. Jaruwongrungrsee, A. Tuantranont, C. Fumeaux, and D. Abbott, “Metamaterial-based microfluidic sensor for dielectric characterization,” en, *Sensors and Actuators A: Physical*, vol. 189, pp. 233–237, Jan. 2013, ISSN: 0924-4247. DOI: 10.1016/j.sna.2012.10.027. [Online]. Available: <http://www.sciencedirect.com/science/article/pii/S0924424712006371> (visited on 01/15/2021).
- [8] A. A. Abduljabar, D. J. Rowe, A. Porch, and D. A. Barrow, “Novel Microwave Microfluidic Sensor Using a Microstrip Split-Ring Resonator,” *IEEE Transactions on Microwave Theory and Techniques*, vol. 62, no. 3, pp. 679–688, Mar. 2014, Conference Name: IEEE Transactions on Microwave Theory and Techniques, ISSN: 1557-9670. DOI: 10.1109/TMTT.2014.2300066.
- [9] I. M. Rusni, A. Ismail, A. R. H. Alhawari, M. N. Hamidon, and N. A. Yusof, “An Aligned-Gap and Centered-Gap Rectangular Multiple Split Ring Resonator for dielectric sensing applications,” eng, *Sensors (Basel, Switzerland)*, vol. 14, no. 7, pp. 13134–13148, Jul. 2014, ISSN: 1424-8220. DOI: 10.3390/s140713134.
- [10] C. Lee and C. Yang, “Complementary Split-Ring Resonators for Measuring Dielectric Constants and Loss Tangents,” *IEEE Microwave and Wireless Components Letters*, vol. 24, no. 8, pp. 563–565, Aug. 2014, Conference Name: IEEE Microwave and Wireless Components Letters, ISSN: 1558-1764. DOI: 10.1109/LMWC.2014.2318900.
- [11] H. Torun, S. Sadeghzadeh, and A. D. Yalcinkaya, “Note: Tunable overlapping half-ring resonator,” *Review of Scientific Instruments*, vol. 84, no. 10, p. 106107, Oct. 2013, Publisher: American Institute of Physics, ISSN: 0034-6748. DOI: 10.1063/1.4825347. [Online]. Available: <https://aip.scitation.org/doi/10.1063/1.4825347> (visited on 01/15/2021).
- [12] P. M. Ragi, K. S. Umadevi, P. Nees, J. Jose, M. V. Keerthy, and V. P. Joseph, “Flexible split-ring resonator metamaterial structure at microwave frequencies,” en, *Microwave*

- and Optical Technology Letters*, vol. 54, no. 6, pp. 1415–1416, 2012, eprint: <https://onlinelibrary.wiley.com/doi/pdf/10.1002/mop.26814>, ISSN: 1098-2760. DOI: <https://doi.org/10.1002/mop.26814>. [Online]. Available: <https://onlinelibrary.wiley.com/doi/abs/10.1002/mop.26814> (visited on 01/15/2021).
- [13] R. Melik, E. Unal, N. Kosku Perkgoz, C. Puttlitz, and H. V. Demir, “Flexible metamaterials for wireless strain sensing,” *Applied Physics Letters*, vol. 95, no. 18, p. 181 105, Nov. 2009, Publisher: American Institute of Physics, ISSN: 0003-6951. DOI: 10.1063/1.3250175. [Online]. Available: <https://aip.scitation.org/doi/abs/10.1063/1.3250175> (visited on 01/15/2021).
- [14] M. E. Jalil, M. K. A. Rahim, N. A. Samsuri, and R. Dewan, “Flexible printed chipless RFID tag using metamaterial–split ring resonator,” en, *Applied Physics A*, vol. 122, no. 4, p. 348, Mar. 2016, ISSN: 1432-0630. DOI: 10.1007/s00339-016-9865-5. [Online]. Available: <https://doi.org/10.1007/s00339-016-9865-5> (visited on 01/15/2021).
- [15] H. K. Kim, K. Ling, K. Kim, and S. Lim, “Flexible inkjet–printed metamaterial absorber for coating a cylindrical object,” *Optics Express*, vol. 23, Mar. 2015. DOI: 10.1364/OE.23.005898.
- [16] R. A. Awang, T. Baum, M. Nasabi, S. Sriram, and W. S. T. Rowe, “Mechanically tolerant fluidic split ring resonators,” en, *Smart Materials and Structures*, vol. 25, no. 7, p. 075 023, Jun. 2016, Publisher: IOP Publishing, ISSN: 0964-1726. DOI: 10.1088/0964-1726/25/7/075023. [Online]. Available: <https://iopscience.iop.org/article/10.1088/0964-1726/25/7/075023/meta> (visited on 01/15/2021).
- [17] F. Zhang, Z. Liu, K. Qiu, W. Zhang, C. Wu, and S. Feng, “Conductive rubber based flexible metamaterial,” *Applied Physics Letters*, vol. 106, no. 6, p. 061 906, Feb. 2015, Publisher: American Institute of Physics, ISSN: 0003-6951. DOI: 10.1063/1.4908253. [Online]. Available: <https://aip.scitation.org/doi/10.1063/1.4908253> (visited on 01/15/2021).
- [18] M. Stoppa and A. Chiolerio, “Wearable Electronics and Smart Textiles: A Critical Review,” *Sensors (Basel, Switzerland)*, vol. 14, no. 7, pp. 11 957–11 992, Jul. 2014, ISSN: 1424-8220. DOI: 10.3390/s140711957. [Online]. Available: <https://www.ncbi.nlm.nih.gov/pmc/articles/PMC4168435/> (visited on 01/15/2021).
- [19] K. Mondal, “Recent Advances in Soft E-Textiles,” en, *Inventions*, vol. 3, no. 2, p. 23, Jun. 2018, Number: 2 Publisher: Multidisciplinary Digital Publishing Institute. DOI: 10.3390/

- inventions3020023. [Online]. Available: <https://www.mdpi.com/2411-5134/3/2/23> (visited on 01/15/2021).
- [20] J. Zhong, A. Kiourti, T. Sebastian, Y. Bayram, and J. Volakis, "Conformal Load-Bearing Spiral Antenna on Conductive Textile Threads," *IEEE Antennas and Wireless Propagation Letters*, 2017. DOI: 10.1109/LAWP.2016.2570807.
- [21] B. Moradi, R. Fernández-García, and I. Gil, "E-Textile Embroidered Metamaterial Transmission Line for Signal Propagation Control," eng, *Materials (Basel, Switzerland)*, vol. 11, no. 6, Jun. 2018, ISSN: 1996-1944. DOI: 10.3390/ma11060955.
- [22] M. S. Hesarian, S. S. Najar, and R. S. Shirazi, "Design and fabrication of a fabric for electromagnetic filtering application (experimental and modeling analysis)," *The Journal of The Textile Institute*, vol. 109, no. 6, pp. 775–784, Jun. 2018, Publisher: Taylor & Francis _eprint: <https://doi.org/10.1080/00405000.2017.1369346>, ISSN: 0040-5000. DOI: 10.1080/00405000.2017.1369346. [Online]. Available: <https://doi.org/10.1080/00405000.2017.1369346> (visited on 01/15/2021).
- [23] F. Raval, S. Purohit, and Y. P. Kosta, "Dual-band wearable antenna using split ring resonator," *Waves in Random and Complex Media*, vol. 26, no. 2, pp. 235–242, Apr. 2016, Publisher: Taylor & Francis _eprint: <https://doi.org/10.1080/17455030.2015.1137374>, ISSN: 1745-5030. DOI: 10.1080/17455030.2015.1137374. [Online]. Available: <https://doi.org/10.1080/17455030.2015.1137374> (visited on 01/15/2021).
- [24] M. Hasani, A. Vena, L. Sydänheimo, L. Ukkonen, and M. Tentzeris, "Implementation of a Dual-Interrogation-Mode Embroidered RFID-Enabled Strain Sensor," *IEEE Antennas and Wireless Propagation Letters*, vol. PP, Sep. 2013. DOI: 10.1109/LAWP.2013.2283539.
- [25] S. Zahertar, A. D. Yalcinkaya, and H. Torun, "Rectangular split-ring resonators with single-split and two-splits under different excitations at microwave frequencies," *AIP Advances*, vol. 5, no. 11, p. 117 220, Nov. 2015, Publisher: American Institute of Physics. DOI: 10.1063/1.4935910. [Online]. Available: <https://aip.scitation.org/doi/10.1063/1.4935910> (visited on 01/15/2021).
- [26] S. Zahertar, L. E. Dodd, and H. Torun, "Embroidered Rectangular Split-Ring Resonators for Material Characterisation," in *2019 IEEE International Conference on Flexible and Printable Sensors and Systems (FLEPS)*, Jul. 2019, pp. 1–3. DOI: 10.1109/FLEPS.2019.8792233.

- [27] X. Zhang, C. Ruan, T. u. Haq, and K. Chen, “High-Sensitivity Microwave Sensor for Liquid Characterization Using a Complementary Circular Spiral Resonator,” en, *Sensors*, vol. 19, no. 4, p. 787, Jan. 2019, Number: 4 Publisher: Multidisciplinary Digital Publishing Institute. DOI: 10.3390/s19040787. [Online]. Available: <https://www.mdpi.com/1424-8220/19/4/787> (visited on 01/15/2021).
- [28] R. Joffe, E. O. Kamenetskii, and R. Shavit, “Novel microwave near-field sensors for material characterization, biology, and nanotechnology,” *Journal of Applied Physics*, vol. 113, no. 6, p. 063 912, Feb. 2013, Publisher: American Institute of Physics, ISSN: 0021-8979. DOI: 10.1063/1.4791713. [Online]. Available: <https://aip.scitation.org/doi/abs/10.1063/1.4791713> (visited on 01/15/2021).
- [29] K. Staszek, I. Piekarz, J. Sorocki, S. Koryciak, K. Wincza, and S. Gruszczynski, “Low-Cost Microwave Vector System for Liquid Properties Monitoring,” *IEEE Transactions on Industrial Electronics*, vol. 65, no. 2, pp. 1665–1674, Feb. 2018, Conference Name: IEEE Transactions on Industrial Electronics, ISSN: 1557-9948. DOI: 10.1109/TIE.2017.2733423.
- [30] S. Ryyänen, “The electromagnetic properties of food materials: A review of the basic principles,” en, *Journal of Food Engineering*, vol. 26, no. 4, pp. 409–429, Jan. 1995, ISSN: 0260-8774. DOI: 10.1016/0260-8774(94)00063-F. [Online]. Available: <http://www.sciencedirect.com/science/article/pii/026087749400063F> (visited on 01/15/2021).
- [31] O. Korostynska, R. Blakey, A. Mason, and A. Al-Shamma’a, “Novel method for vegetable oil type verification based on real-time microwave sensing,” en, *Sensors and Actuators A: Physical*, Selected Papers from the 26th European Conference on Solid-State Transducers Kraków, Poland, 9-12 September 2012, vol. 202, pp. 211–216, Nov. 2013, ISSN: 0924-4247. DOI: 10.1016/j.sna.2012.12.011. [Online]. Available: <http://www.sciencedirect.com/science/article/pii/S0924424712007480> (visited on 01/15/2021).
- [32] S. Trabelsi and S. O. Nelson, “Microwave sensing of quality attributes of agricultural and food products,” *IEEE Instrumentation Measurement Magazine*, vol. 19, no. 1, pp. 36–41, Feb. 2016, Conference Name: IEEE Instrumentation Measurement Magazine, ISSN: 1941-0123. DOI: 10.1109/MIM.2016.7384959.
- [33] M. H. Zarifi, M. Rahimi, M. Daneshmand, and T. Thundat, “Microwave ring resonator-based non-contact interface sensor for oil sands applications,” en, *Sensors and Actuators*

B: Chemical, vol. 224, pp. 632–639, Mar. 2016, ISSN: 0925-4005. DOI: 10.1016/j.snb.2015.10.061. [Online]. Available: <http://www.sciencedirect.com/science/article/pii/S092540051530527X> (visited on 01/15/2021).

- [34] S. Trabelsi, A. W. Kraszewski, and S. O. Nelson, “A microwave method for on-line determination of bulk density and moisture content of particulate materials,” *IEEE Transactions on Instrumentation and Measurement*, vol. 47, no. 1, pp. 127–132, Feb. 1998, Conference Name: IEEE Transactions on Instrumentation and Measurement, ISSN: 1557-9662. DOI: 10.1109/19.728804.
- [35] *Handbook of Organic Solvent Properties*, en. Elsevier, 1996, ISBN: 978-0-08-052378-1. DOI: 10.1016/C2009-0-23646-4. [Online]. Available: <https://linkinghub.elsevier.com/retrieve/pii/C20090236464> (visited on 01/15/2021).

Chapter 8

Conclusion and Future Outlook

In summary, the aim of this thesis is to develop a new method of integrating biosensing and fluid manipulation capabilities in a single structure for LoC applications. This is realised by combining SRR-based electromagnetic sensors and SAW actuators in a single geometry that can be employed for multiple applications in various frequency bands. The proposed device can be employed as an SRR-based sensor when excited wirelessly under microwave frequencies and the same geometry can be utilised to generate acoustic waves on the surface when RF power is applied to its electrodes. As a result, microfluidic functions can be accomplished. Some parameters are needed to be taken into consideration: the design of the device should include interdigitated transducers (IDTs) fabricated on a piezoelectric substrate; this would satisfy the generation of acoustic waves. Another factor is that the electrode pads should be designed close to each other with a gap similar to splits in SRRs, as the effective capacitance is dominated by gap capacitance and surface capacitance, and also the substrate should be a dielectric material to satisfy the condition needed for SRR-based sensing.

The concept of the integrated system is presented for different designs in this thesis. In chapter 3, as a proof of concept, a geometry with curved IDT patterns was introduced and fabricated on a lithium niobate substrate. Streaming, pumping and jetting functions were achieved when the RF power of 0.2-7 W was applied to the electrode pads. The device was characterised by simulation and experiments and its electromagnetic resonant frequency was identified. Monopole antennas were utilised to generate electromagnetic waves and to excite the device wirelessly in microwave

frequencies. The device had a fundamental magnetic frequency of 4.41 GHz with a quality factor of 294. To demonstrate the sensing capability of the resonator, a droplet of $2 \mu\text{L}$ with different glucose concentrations was placed on the device and as expected the resonant frequency shifted towards higher frequencies by increasing the concentration. The reason is that by increasing the glucose concentration in a solution, the relative permittivity is reduced and therefore, the effect capacitance decreases. The sensitivity of 28 MHz/(mg/ml) was achieved. In another experiment, the shift in resonant frequency of the device was monitored by changing the location of the DI droplet that was placed close to the sensor.

In chapter 4, the design composed of circular IDTs patterned on a lithium niobate substrate was based on a dual split ring resonator geometry (DSRRs). Although DSRRs can be commonly used in metamaterial-based sensing application, they are not among conventional geometries in acoustofluidics. The sensing capability of the resonator was verified by monitoring the shift in frequency when a droplet with a volume of $30 \mu\text{L}$ was placed in the center of the rings. In another experiment, a glass container filled with various materials was placed on the gap area of the inner resonator and the frequency response of the device was obtained. The materials with a higher relative permittivity resulted in a lower resonant frequency. Yeast fermentation process was also monitored as a case study using this device. The device had acoustic frequencies between 5-30 MHz and 18 MHz was picked to mix polystyrene particles inside a DI droplet that was placed on the center of the device.

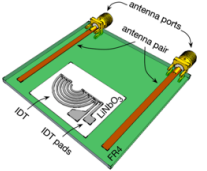
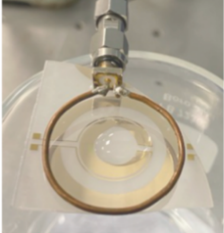
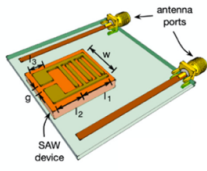
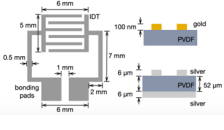
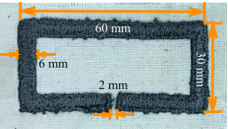
In chapter 5, straight IDTs were patterned on a woven carbon fiber substrate that was coated with polyimide and ZnO. The device was utilised to control temperature inside a liquid droplet using acoustic waves and also was utilised as a UV sensor with sensitivity of 56.86 ppm/(mW/cm²). The sensing capability of the device was investigated by placing droplets with different concentrations of glucose on a specific location on the device and by monitoring the shift in frequency by altering the glucose concentration. The device exhibited a sensitivity of 0.34 MHz/(mg/dL).

In the next chapter, the proposed concept was implemented on a flexible PVDF substrate. Straight IDTs were patterned on the substrate using laser milling. The resonances of the devices under various excitation configurations were obtained through simulation. Monopole antennas were used in experiments to excite the structure and the transmission frequency response of the device was obtained between 3-4.5 GHz with a resonance at 3.4 GHz. The device was characterised in radio

frequencies too and presented an acoustic resonance at 3.2 MHz. We couldn't achieve efficient microfluidics using this device. The reasons can be excessive attenuation of the acoustic waves in the polymer layer, or the use of laser in fabrication process, which can disturb the polarisation of the PVDF layer and remove its piezoelectric material property.

A key other progress towards the new-generation of sensing is the development of wireless flexible sensors. We contributed to this objective by fabricating an embroidered rectangular SRR on a cloth that is excited wirelessly by monopole antennas. The sensor was wrapped around a bottle and its magnetic behaviour under different electromagnetic excitation conditions was characterised through experimental measurements and was verified through simulations. In the next step, the bottle was filled with various dielectric materials and the shift in frequency was monitored. As expected, the sensor showed higher resonances when the bottle was filled with materials with lower relative permittivity. A summary of the key findings for the individual devices presented in each chapters are presented in the following Table:

Table 8.1: Summary of the chapters.

Functionality Device	Split-ring resonator (SRR)-based Sensing	Surface acoustic wave (SAW)-based sensing and actuation
	<ul style="list-style-type: none"> • Glucose sensing, sensitivity*: 28 MHz/(mg/dL) 	<ul style="list-style-type: none"> • Streaming, pumping and jetting
	<ul style="list-style-type: none"> • Glucose sensing, sensitivity*: 18 kHz/(mg/dL) • Material Characterisation • Monitoring Yeast Fermentation 	<ul style="list-style-type: none"> • Streaming**
	<ul style="list-style-type: none"> • Glucose sensing, sensitivity*: 0.34 MHz/(mg/dL) 	<ul style="list-style-type: none"> • UV sensing, Sensitivity: 56.86 ppm/(mW/cm²) • Temperature control of the droplet.
	<ul style="list-style-type: none"> • Electromagnetic characterisation • Device optimisation and further experiments are required 	<ul style="list-style-type: none"> • Acoustic characterisation • Device optimisation and further experiments are required
	<ul style="list-style-type: none"> • Material Characterisation 	<ul style="list-style-type: none"> • Not Applicable

* Sensitivities reported for devices in each chapter are not comparable with each other, as the location of the droplet, the droplet size, and the geometry of the device have an impact on the achieved sensitivity.

** The actuation capability of this device wasn't explored to its full extent and only streaming functionality was investigated.

8.1 Future Work

The new method is described in this thesis together with different implementations of devices. A key advantage for wireless sensing is the capability of operating devices in array formations where individual devices in an array can be interrogated simultaneously. This capability has not been investigated in this thesis and is worth investigating for its limits. In an array of devices, individual elements can be functionalised with different molecules or analytes for multi-agent detection.

Another future direction could be the development of a portable readout unit for the presented sensors. The devices were characterised using a vector network analyser. This is ideal for benchmarking and fundamental analysis. However, it is not practical to use a benchtop network analyser for a LoC application. Design of readout electronics based S_{11} and S_{21} spectra presented in this thesis can be a topic for a future study.

Packaging of these devices and their use cases require future work. It is not challenging to fabricate these devices using conventional processes. However, these devices need to be packaged appropriately considering specific applications and form factors.

Finally, clinically relevant studies need to be designed to investigate the reliability of the data that can be collected using these devices.

Acronyms

AC	Alternating Current
AdTSV	Adsorptive Transfer Stripping Voltammetry
Ag	Silver
AgCl	Silver Chloride
Al	Aluminium
AlN	Aluminium Nitride
Ar	Argon
Au	Gold
BAW	Bulk Acoustic Wave
C ₂ H ₅ OH	Ethanol
C ₆ H ₁₂ O ₆	Glucose
CdS	Cadmium Sulfide
Cl	Chlorine
CMOS	Complementary metal–oxide–semiconductor
CO	Carbon Monoxide
CO ₂	Carbon Dioxide
CP	Cell-Phone
Cr	Chromium
CTFE	Chlorotrifluoroethylene
CYTOP	Amorphous Fluoropolymer

Acronyms

dB	Decibels
DC	Direct Current
DI	Deionised
DNA	Deoxyribonucleic Acid
DPDI ²⁺	Diphenoquinone Diamine
DSRR	Dual Split Ring Resonator
EM	Electromagnetic
FBAR	Film Bulk Acoustic Resonator
FEA	Finite Element Analysis
FGF-2	Fibroblast Growth Factor 2
FR4	Flame Retardant 4: Glass-Reinforced Epoxy Laminate Material
GaAs	Gallium Arsenide
HFP	Hexafluoropropylene
IDT	Interdigital Transducer
IPA	Isopropanol
LC	Inductor Capacitor
LDPE	Low-Density Polyethylene
LHM	Left Hand Material
LiNbO ₃	Lithium Niobate
LiTaO ₃	Lithium Tantalate
LoC	Lab-On-Chip
LSAW	Leaky SAW
MEMS	Microelectromechanical systems

N	Nitrogen
NFC	Near Field Communication
O	Monoxide
O ₂	Dioxide
PDMS	Polydimethylsiloxane
PET	Poly-Ethylene Terephthalate
pH	Potential of hydrogen
PhD	Doctor of Philosophy
PI	Polyimide
PoC	Point-of-care
PoCT	Point-of-care Testing
PVDF	Polyvinylidene fluoride
QCM	Quartz Crystal Microbalance
RF	Radio Frequency
RFID	Radio Frequency Identification
RHM	Right Hand Material
RLC	Resistor Inductor Capacitor
SAW	Surface Acoustic Wave
SBAW	Shear BAW
SCE	Saturated Calomel Electrode
Si	Silicon
SiO ₂	Silicon Dioxide
SPUDT	Single-Phase Unidirectional Transducer
SRR	Split Ring Resonator

Acronyms

TCF	Temperature Coefficient of Frequency
TrFE	Trifluoroethylene
TSAW	Traveling SAW
TSM	Thickness Shear Mode
UNCD	Nanocrystalline Diamond
UNN	University of Northumbria, Newcastle
US	United States
USD	United States Dollar
UV	Ultraviolet
VNA	Vector Network Analyser
Zn	Zinc
ZnO	Zinc Oxide